University of Strathclyde

Department of Mechanical & Aerospace Engineering

Lattice Boltzmann modelling of droplet dynamics in confinement

Nikolaos Ioannou

A thesis presented in fulfilment of the requirements
for the degree of Doctor of Philosophy

2016

Declaration of author's rights

This thesis is the result of the author's original research. It has been composed by the author and has not been previously submitted for examination which has led to the award of a degree.

The copyright of this thesis belongs to the author under the terms of the United Kingdom Copyright Acts as qualified by University of Strathclyde Regulation 3.50. Due acknowledgement must always be made of the use of any material contained in, or derived from, this thesis.

<div align="right">

Nikolaos Ioannou

July 2016

</div>

Abstract

Droplet behaviour influences significantly the quality of emulsions and the performance of microfluidics applications. Despite the numerous studies on droplet behaviour, the interactions between the suspended droplet and its surrounding walls, especially for non-Newtonian fluids, are not yet fully understood.

Here, we investigate the behaviour of isolated droplets subjected to a simple shear in a wide range of capillary numbers, confinement ratios and viscosity relations between the droplet and the carrier fluid. Simulations are performed using the colour-gradient lattice Boltzmann method (LBM), which is also adapted to handle power-law fluids.

Findings on the Newtonian droplets in a Newtonian carrier fluid show that droplet deformation and orientation to the flow, i.e. tumbling, are enhanced with increasing confinement. Even more, with a larger viscosity ratio the rate of the deformation increases more significantly while the rate of tumbling becomes smaller. Noteworthy, the largest deformation is presented by droplets of the same viscosity as the matrix fluid. We also find that in a shear-thickening carrier fluid droplet deformation and tumbling are enhanced while they are reduced in a shear-thinning fluid.

Additionally, with increasing confinement, the lowest capillary number a droplet breaks increases in the low viscosity ratio cases, contrary to the high viscosity ratio ones. At unity viscosity ratio this critical capillary number is slightly affected while droplets are found to break at a lower capillary number in a power-law carrier fluid.

Simulations are performed to examine the behaviour of power-law droplets sheared in a Newtonian carrier fluid. The results are correlated well with the ones of the Newtonian droplets when the droplets obtain ellipsoidal shapes. However, upon slight deviation from the ellipsoidal shape the behaviour of power-law droplets differs substantially from their Newtonian counterparts.

Acknowledgements

Contribution to the Literature

- Journal Papers.

  1. Droplet dynamics in confinement, N. Ioannou, H. Liu and Y.H. Zhang, *Journal of Computational Science*, In Press, Corrected Proof, 2016.

  2. Lattice Boltzmann simulations of thermocapillary motion of droplets in microfluidic channels, J. Li, H. Liu, N. Ioannou, Y.H. Zhang and J.M. Reese, *Communications in Computational Physics*, 17(05), 1113 − 1126, 2015

- Conference Papers

  1. Three-dimensional simulations of droplet deformation and breakup in simple shear flow using the lattice Boltzmann method, *Proceedings of the 4th European Conference on Microfluidics*, Limerick, Ireland, long oral, 2014

Contents

List of Figures

List of Tables

Nomenclature

Latin

$2R/H$ confinement ratio

$\mathcal{S}$ second order tensor in the Maffetone–Minale model

B small axis of the ellipsis

c microscopic lattice velocity magnitude

C_S shape parameter in the Shapira–Haber model

c_s speed of sound

Ca capillary number

D droplet deformation parameter

D_T deformation in the Taylor theory

D_{MMSH} deformation in the combined Maffettone–Minale-Shapira–Haber model

D_{MM} deformation in the Maffettone–Minale model

D_{SH} deformation in the Shapira–Haber model

e microscopic lattice velocity vector

F force vector

H height

L large axis of the ellipsis

$l.u.$ lattice unit

L_0 characteristic length

m_1, m_2 coefficients in the Maffetone–Minale model

n power law exponent, or normal unit vector

p pressure

R droplet radius

r position vector

Re Reynolds number

S rate of shear strain

T deviatoric stress tensor

t simulation time step

t^* time instant

U velocity magnitude

u velocity vector

w weight coefficient

x, y, z components in Cartesian coordinate system

Greek

Δt duration of the simulation

δ_t lattice time step, iteration, timestep

δ_x lattice length

$\dot{\gamma}$ shear rate tensor

$\dot{\gamma}_0$ global imposed shear rate magnitude

η varying dynamic viscosity

κ curvature

λ viscosity ratio

μ constant dynamic viscosity

Φ force term

ρ density

ρ^N colour index function

σ surface tension coefficient

τ relaxation parameter

θ orientation angle

Super- Subscripts

0   characteristic property

α, β index notations

B blue fluid

b bottom wall

c continuous fluid

d dispersed or droplet fluid

$emul$ emulsion

i microscopic velocity lattice direction

LBM lattice Boltzmann method

$phys$ physical

R red fluid

S surface

t top wall

x, y, z components in Cartesian coordinate system

Chapter 1

Introduction

1.1 Motivation

The research interest in droplet dispersions has been growing, as they are important to natural processes and industrial applications, e.g. emulsions, microfluidic devices, and porous media. In these processes and applications the fluids can be both Newtonian and non-Newtonian. A plethora of numerical and experimental studies have been performed to reveal fundamental droplet dynamics.

1.1.1 Droplet-based Applications

Emulsions consist of mixtures of immiscible liquids, one of which is finely dispersed in the continuous phase of another. Emulsion-based products are widely used in food, chemical, and pharmaceutical industries.

Moreover, a single droplet can be employed as a precisely controlled reaction site to study enzyme kinetics and perform DNA analysis, and bio-chemical assays [1]. This potential is exploited by droplet based microfluidic technologies which attract ever-growing attention. The performance of devices which handle microdroplets, comparable or even smaller in size than at least one channel dimension, depends significantly on droplets dynamics [2].

Furthermore, the flow of oil-in-water emulsions through porous media show a non-trivial "pseudo non-Newtonian" behaviour [3]. The study of droplet deformation and breakup can provide valuable insights into immiscible fluid displacement in porous

1

media, which plays an important role in enhanced oil and natural gas recovery [4].

1.1.2   Newtonian and Power-law Fluids

The Newtonian fluid constitutive modelling assigns the *viscosity* as a constant property. This leads to a linear relation between the *stresses* and the *rate of strain* a fluid experiences. The Newtonian fluids include water and other common fluids such as oils which are used in many applications, for example "Silicone oil droplets are often applied in therapeutic protein products, especially in pre-filled syringes or double-chamber cartridges, retina surgery, oil-in-water (O/W) emulsions, and even used as intraocular tamponade and microreactors", see [5] and references therein.

However, fluids which display a non-Newtonian character have also an important impact in the industry. The main difference from the Newtonian fluids is that during a process the relation between the *stresses* and the *rate of strain* is not linear. The *viscosity* of a non-Newtonian fluid is modelled as a function of the spatial and temporal *shear* which varies concurrently to the evolution of the droplet.

Power-law fluids are considered as the simplest example in the category of non-Newtonian fluids. They exhibit shear-thinning behaviour, which is one of the most frequently encountered in industrial applications [6], or shear thickening behaviour found in concentrated emulsions [7].

This research includes both types of fluids, i.e. Newtonian and power-law, which notably show different behaviour in the same flow conditions, especially in pinch-off events [8].

1.1.3   Numerical Approach

Experimental methods for the droplet deformation rely on accurate measurements of droplet shape data that are provided by the application of video optical microscopy and image analysis techniques coupled with computer-controlled high precision shear flow cells [9]. Besides the uncertainties in the experimental measurements, purely inelastic liquids cannot be created. This issue emerges from the fact that non-Newtonian fluids are the result of polymer blends, such those reported in [10, 11, 12, 13, 14].

On the other hand, pure inelastic fluids can be modelled with numerical methods,

which act complementary to experimental studies. This work applies the numerical lattice Boltzmann method (LBM) to study droplet dynamic behaviour.

1.1.4   Flow Configuration

This work considers a single droplet immersed in a matrix fluid system which can be considered as a first approach to model dilute emulsions [15, 16]. The droplet size and shape determine important emulsion properties, i.e. stability and rheology [17]. To understand the mechanisms of droplet deformation and breakup during emulsification, systematic evaluation of droplet behaviour in well-investigated flow conditions is required.

The system is subjected to simple shear which creates a *simple shear flow*, one of the most fundamental rheological arrangements. Its main feature is its relative simplicity while still providing with rich physics [18, 19]. The results of a dilute emulsion in shear can be also applied to polymer blending, and even the behaviour of deformable particles, e.g. blood cells [13].

1.2   The Problem: Droplet in Simple Shear Flow

Figure (1.1) illustrates a spherical droplet of radius R placed halfway between two parallel plates separated by a finite distance H. The dynamic viscosities of the droplet (η_d) and carrier fluids (η_c) may differ in general. However, both fluids have the same density ρ, and the interfacial tension σ is considered constant.

The plates move with equal but opposite velocities (U), introducing the shear flow in the system. The magnitude of the applied shear rate is

$$\dot{\gamma}_0 = 2U/H. \tag{1.1}$$

During the simple shear flow two most important forces are being exerted on the surface of the droplet. Due to the viscosity of the carrier fluid, the viscous forces ($\eta_c \dot{\gamma}_0 R^2$) lead the droplet to turn towards the direction of the flow and deform. On the other hand, the droplet resists the deformation due the capillary forces (σR) which are also responsible for retaining the spherical shape of the droplet.

Consequently, the droplet undergoes an elongation in the direction of the major axis (L), and a compression in the direction of the minor axis (B), as seen on the right-hand side of figure (1.1). The relative magnitude of viscous and capillary forces is measured by the capillary number, which is defined as

$$Ca = \frac{\eta_c \dot{\gamma}_0 R}{\sigma}. \tag{1.2}$$

Additionally, the dynamic behaviour of the droplet is influenced by the inertial forces which are contrasted to the viscous through the Reynolds number

$$Re = \frac{\rho \dot{\gamma}_0 R^2}{\eta_c}. \tag{1.3}$$

In this definition, R and $\dot{\gamma}_0 R$ are the characteristic length and velocity, respectively.

In this study the behaviour of the droplet is investigated under the assumption of insignificant inertial forces in comparison with viscous and interfacial forces. The flow is in Stokes flow regimes where $Re \leq 1$, and the capillary number is important to evaluate the impact of the shear stress on the deformation [2].

Besides the capillary and Reynolds numbers, the proximity of the walls to the droplet which is represented by the confinement ratio $2R/H$, and the viscosities of the
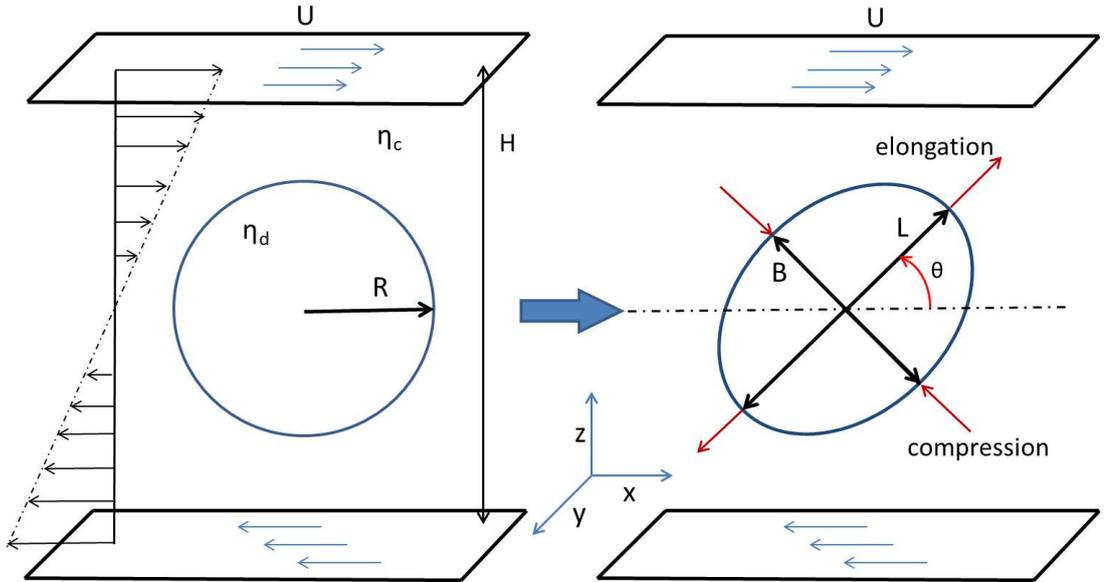
Figure 1.1: Schematic illustration of droplet deformation in a simple shear flow.

fluids, more specifically the relation between them, affect the behaviour of the droplet [20].

In cases where both droplet and carrier fluids are Newtonian the viscosity effects are attributed to the viscosity ratio defined as

$$\lambda = \eta_d/\eta_c. \tag{1.4}$$

Unlike Newtonian fluids the viscosity of a power-law fluid is shear rate dependent. The present work focuses on fluids described by the power law formulation [18]

$$\eta\left(|\dot{\gamma}|\right) = k\left|\dot{\gamma}\right|^{n-1}, \tag{1.5}$$

where $\dot{\gamma}$ is the local shear rate which is explained in details in *Chapter* 2.

In equation (1.5), k is a pre-factor called the consistency index and has units $Pa\,s^n$, or $kg/m\,s^{n-2}$, and n is the so-called power-law exponent which reflects the behaviour of the specific fluid; with increasing shear rate the viscosity of the fluid decreases for $n < 1$ and the fluid is referred to as shear-thinning. Contrariwise, for $n > 1$ the viscosity increases and the fluids are called shear-thickening. Clearly, for $n = 1$ the fluid is Newtonian.

As the viscosity of the power-law fluid is not assigned to a specific value, there is not a specific viscosity ratio to be defined. Two cases have been reported on the power-law droplet sheared in a Newtonian fluid case. A "non-Newtonian viscosity ratio" defined as $\lambda^{NN} = k_d/\eta_c$ in [21], and an "apparent Newtonian viscosity ratio" $\lambda_a = k_d\dot{\gamma}_0^{n-1}/\eta_c$ as in [13]. The procedure to assess the viscosity effects for these fluids is discussed in detail in Chapter 4.

The evolution of the droplet is categorised into two regimes: the steady state and the breakup. In low shear intensity flows, i.e. $Ca \leq 0.4$, the droplet eventually obtains a steady shape. Even more, in weakly bounded configurations where the wall effects are negligible, i.e. for $2R/H = 0.1$, the droplet shape is ellipsoidal which "is a good representation of drop shape not just for small deformations, but up to relatively high values of $Ca[=0.43]$" [22]. Hence, in the steady state the lengths of the axes L and B

of the final ellipsoid droplet are used to define the deformation parameter as

$$D = \frac{L - B}{L + B}. \tag{1.6}$$

The orientation angle (θ) is defined as the angle between the major axis and the horizontal plane, i.e. $x - y$ plane in the mid-height location (dash-dotted line in figure (1.1)).

With strong shear, the capillary forces are not sufficient to retain the shape of the droplet, hence the dominant viscous forces lead the droplet to split into two or more fragments, referred to as daughter droplets. The critical capillary number (Ca_{cr}), defined as the capillary number above which the droplet breakup occurs, is influenced by both the viscosity relation and the degree of the confinement [23] and lead to different breakup sequences-classes [24].

1.3   Literature Review

This section discusses the most relevant theoretical, experimental and computational works. More information on the single droplet and confined dilute Newtonian blend dynamics are presented in [9, 25].

1.3.1   Theoretical Studies

The interest in droplet deformation dates back to Taylor (1934) [26]. This work derives a theoretical expression which describes small deformations in the bulk shear flow, using a first order small deformation perturbation procedure with Ca as the expansion parameter. Hence, the deformation is described in terms of the viscosity ratio and the capillary number as

$$D_T = \frac{19\lambda + 16}{16\lambda + 16} Ca. \tag{1.7}$$

This expression shows good agreement with experimental results reported in the same work in which the value of the confinement ratio is around $2R/H \approx 0.2$.

However, equation (1.7) is not able to predict the droplet deformation for very large viscosity ratios [20, 26]. Notice that here 'T' denotes the Taylor theory. This practice

is adopted to the following models, the deformation parameters of which obtains a matching subscript to distinguish from the predictions of different models.

Furthermore, the Taylor theory does not take into account the influence of the wall proximity. To address the confinement issue, Shapira and Haber solved the Stokes flow around a droplet with the method of reflection, which takes into account the relative position of the droplet to the wall [27]. The resulting model, referred to as the SH model, combines the Taylor deformation and an additional term to include the impact of the walls on the deformation:

$$D_{SH} = D_T \left[1 + C_S \frac{1 + 2.5\lambda}{1 + \lambda} \left(\frac{R}{H} \right)^3 \right],$$ (1.8)

where C_S is referred to as shape parameter and its value depends on the relative position of the droplet to the walls. For a droplet positioned halfway between the two walls C_S is 5.6996.

Regarding the orientation angle both theories predict $\theta = 45°$, even though the droplet turns more to the direction of the flow with increasing Ca, λ and $2R/H$. The perturbation procedure in [26] is extended to the second order in Ca to yield a more accurate expression for the orientation angle [28, 29]: $\theta = \frac{\pi}{4} - \frac{(16+19\lambda)(3+2\lambda)}{80(1+\lambda)} Ca$.

Both Taylor and SH methods address the steady state problem. To predict the droplet deformation under transient conditions Maffettone and Minale proposed a phenomenological model [30], referred to as MM model. A second order tensor $\mathcal{S}$, the eigenvalues of which reflect the squares of the semi-axes of the ellipsoid, describes the shape of the droplet. Based on the assumption that the droplet shape remains ellipsoidal at all times an evolution equation for the tensor $\mathcal{S}$ is derived, which consists of a co-rotational derivative, the contributions of the viscous stresses and the capillary force. This equation predicts the values of the semi-axes for typical flows, including the simple shear, the uniaxial extensional and the planar hyperbolic flow. In particular, the deformation parameter in the steady state for the simple shear flow is calculated as

$$D_{MM} = \frac{\sqrt{m_1^2 + Ca^2} - \sqrt{m_1^2 + \left(1 - m_2^2\right) Ca^2}}{m_2 Ca},$$ (1.9)

where

$$m_1 = \frac{40(\lambda + 1)}{(2\lambda + 3)(19\lambda + 16)},$$ (1.10)

and

$$m_2 = \frac{5}{2\lambda + 3} + \frac{3Ca^2}{2 + 6Ca^2}.$$ (1.11)

To consider wall effects the MM model was extended by Minale in [15], where it is led to recover the analytical limits of the SH model. The new MM model, referred to as MMc, integrates new functions for m_1 and m_2. The calculation of the new functions involves parameters which are estimated by experimental data in the literature [20, 31]. Finally, both the MM and the MMc models estimate the orientation angle using the value m_1 as: $\theta = \frac{1}{2} \arctan\left(\frac{m_1}{Ca}\right)$.

More phenomenological models are discussed in [32]. Despite the initial assumption of the ellipsoidal droplet shape at all times, more complex theories do take into account the breakup and coalescence phenomena. For example, the Almusallam, Larson, and Salomon (ALS) model provides acceptable predictions in some cases.

1.3.2   Experimental Studies

As already mentioned, the earliest experiments investigating the shear of droplets are reported in [26] which considers weakly bounded conditions.

Further investigations which consider very low, $(\lambda = 2 \times 10^{-4})$, and relatively high viscosity ratios $(\lambda = 6)$ are conducted in [24], which confirms the validity of the Taylor theory. Moreover, it emphasises on the breakup regime and proposes four classes: *A*: the droplet obtains an ellipsoid-like shape and tiny droplets ("fragments of liquid") detach from its tips; *B-1*: at $\lambda = 1$ the droplet creates a thin neck and two dumbbell-like edges until it breaks into two, with smaller ("satellite") droplets in the middle; *B-2* at a bit smaller viscosity ratio, i.e. $\lambda = 0.7$, the neck elongates and becomes thinner until the original droplet bursts into numerous finer droplets; and *C* at high values of λ in which case the droplet tumbles to the direction of the flow and does not break.

The shape of the droplet in shear is investigated at a confinement ratio $2R/H \leq 0.1$ in [22]. The ellipsoidal shape assumption is validated through image analysis up to $Ca = 0.43$, for λ ranging from 1 to 2. Figures (12.b) and (13.b) therein show a

deviation of the ellipsoidal at $Ca = 0.46$.

The confinement effects on the droplet deformation of $\lambda = 1$ are investigated in [31]. Three different capillary numbers, i.e. $Ca = 0.1$, 0.2, and 0.3, are studied and the confinement ratios ranging from $2R/H = 0.14$ to 1. For the same capillary number, the droplet obtains a more elongated shape in higher confinement. Also, the droplet shape deviates from the ellipsoid at very high confinement ratios, i.e. $2R/H \geq 0.8$.

A similar study shows insignificant differences in the deformation up to confinement ratios of $2R/H < 0.37$, for viscosity ratios above and below unity [20]. However, with increasing confinement the differences in deformation grow considerably and are more significant at large capillary numbers.

In order to fit the experimental results regarding the large deformation at large capillary numbers, i.e. $Ca = 0.3$, with an analytical expression, two models are proposed.

One of them is the orientation angle-scaled SH model, in which the deformation parameter D_{SH} scales with the term $sin\theta cos\theta$. However, it shows to underestimate the deformation at high capillary numbers. Also, the model suffers from the difficulty of estimating experimentally the orientation angle at low deformations [22]. The other model, is a combination of the SH and MM models. Specifically, the term D_T in the SH model is replaced by D_{MM} leading to a new model, referred to as MMSH model:

$$D_{MMSH} = D_{MM} \left[1 + C_S \frac{1 + 2.5\lambda}{1 + \lambda} \left(\frac{R}{H} \right)^3 \right]. \tag{1.12}$$

Since the predictions from this model show very good agreement with the experimental data and there is no need to estimate the droplet orientation angle in [20], it is used to verify the numerical model and support the simulations results in this work.

Regarding the breakup, [33] shows that a droplet over $\lambda \geq 4$ experiences breakup in a highly confined geometry. Further on, [23] studies the breakup for more viscosity ratios, above and below unity, in a wide range of confinement ratios. The experimental results show good agreement with corresponding numerical data obtained with the boundary integral method (BIM).

Furthermore, experimental studies utilise polymer solutions either to suspend a Newtonian droplet in a non-Newtonian fluid [11, 13], to create a non-Newtonian droplet

which later is sheared in a Newtonian fluid [14], or both [10, 12]. Even though some of the polymer solutions mentioned in these works exhibit shear-thinning behaviour there is no exact correlation to equation (1.5).

A comprehensive work which includes the investigation on a range of isolated particles in simple shear flow involving shear-thinning fluids is reported in [10]. This work examines the deformation and breakup mechanisms of droplets in two experimental setups: *(i)* Newtonian droplets in a shear-thinning matrix fluid, and *(ii)* shear-thinning droplets in a Newtonian matrix fluid.

The constitutive expression used is a power law in the form of $\tau_{xz} = k\dot{\gamma}_0^n$, where τ_{xz} is the shear stress component. However, the relation between the viscosity and the shear rate is not mentioned; thus their results cannot be correlated to the power-law relationship implemented in our simulations. Also, the results on the droplet deformation are plotted against the term $\dot{\gamma}_0 R$ and not the capillary number, while the orientation angles are shown against the deformation parameter. This illustration renders the correlation between numerical and experimental results further problematic.

The findings show that in case *(i)* the deformation of the droplet does not increase linearly with increasing shear intensity. However, the orientation follows the theoretical predictions as reported in [28], regardless the nature of the suspending fluid showing a decreasing θ between 35° and 40°. In addition, the breakup procedure for different apparent viscosity ratios showed to relate to class A in [24] for low apparent viscosity ratio values, while upon greater ratios the breakup matches to class B.

Droplets in system *(ii)* deform following the Taylor theory for the specific values of apparent viscosity ratio and capillary numbers. This observation indicates that *a Newtonian droplet of a specific viscosity can replicate the behaviour of a power-law one.* In addition, the droplet breakup exhibits a character which corresponds to class B.

The behaviour of strong shear-thinning droplets sheared in a Newtonian fluid is investigated in [14]. The work follows the correlation $\eta \propto \dot{\gamma}^n$ with $n = -0.8$ for the liquid of the droplet. This value would correspond to $n = 0.2$ with respect to the definitions in equation (1.5). The respective droplets exhibited a very weak deformation and high orientation to the flow for small Ca, while noteworthy deformation is observed at capillary number above $Ca \geq 6$.

An extensive work on breakup is presented in [13], where the continuous phase is Newtonian in all cases to negate the effect of droplet elasticity. Newtonian droplets are used as comparative means to evaluate non-Newtonian droplets. In the Newtonian experiments the critical capillary numbers are over-predicted. This finding possibly links to the fact that the confinement ratio of the experimental apparatus is $2R/H = 0.4762$. Overall, the study shows that the critical capillary number values are a bit higher for the shear-thinning droplets than the respective viscous Newtonian droplets. This could explain the larger deformation prior to breakup, which occurs in a similar fashion to the Newtonian.

Other experiments report the formation of droplets in flow focusing devices. The generation of shear-thinning droplets, which display also yield stress, in a Newtonian carrier fluid in investigated in [8]. The droplets that occur are larger than the Newtonian case. Contrariwise, in [5] Newtonian droplets are generated while the carrier fluid is described by a power-law relation. The difference is detected in the neck formation due to the different pinching behaviour in shear-thinning fluids.

1.3.3   Numerical Studies

Complementing the theoretical and experimental studies, numerical simulations are extensively used to investigate the droplet behaviour in the simple shear flow. Numerical simulations give insight to quantities such as the velocity, pressure and viscosity fields inside and outside the droplet. In addition, they have the ability to illustrate the deformation and breakup from different standpoints. Here, we summarise the most relevant works and categorise them by the numerical method they implement.

1.3.3.1   Boundary Integral Method (BIM)

The earliest work to implement the BIM in arbitrary sheared droplet simulations dates back to 1981 [19]. The study is limited to the Stokes flow in two dimensions (2D) with a unity viscosity ratio, i.e. $\lambda = 1$. Later on, the same conditions are implemented in [34] which investigates not only the behaviour of a single droplet but also a suspension of droplets. The illustrations of velocity streamline patterns inside and outside droplets are noteworthy. For the single droplet system these patterns show a recirculating zone

around the droplet and a single vortex-like structure in the interior.

While the previous numerical studies consider $\lambda = 1$, [35] examines a range of viscosity ratios from 0.08 to 6.4. The results of three dimensional (3D) simulations at varying capillary numbers agree well with theoretical and experimental data available at that time. Interestingly, the velocity streamlines inside a low viscosity droplet, $\lambda = 0.08$, form a two vortices pattern at low capillary numbers, i.e. $Ca \leq 0.01$. The streamlines turn into single vortex at a greater capillary number, i.e. $Ca = 0.2$. For viscosity ratio unity and above $\lambda \geq 1$ only single vortex formations are observed as in [34].

It is noticeable that the above studies do not explicitly mention the Reynolds number. The only remark is that it is sufficiently small to recover the Stokes flow regime. The influence of the Reynolds number is evaluated in [36] concluding that there are no significant differences in the results between flows at $Re = 1$ and those reported in [34] for vanishing Reynolds number. Additionally, the inertial forces impact on the droplet deformation for $Re = 1, 10, 50, 100$ is examined. It is notable that the interior flow shows qualitatively similar behaviour at $Re = 50$ to that of low viscosity ratios although in the former case the two vortice-like patterns turns more to the direction of the flow.

The progress in numerical studies using the BIM involves the topic of the confinement effect which is systematically addressed in works conducted by P.J.A. Janssen and co-workers.

Initially, [37] shows the evolution of the deformation and orientation angle for $Ca = 0.2$ and 0.4 in different confinement ratios, which reaches the value $2R/H = 2$ in some cases. Additionally, the critical capillary number is illustrated as a function of the confinement ratio showing the ability of the method to produce binary and ternary breakup modes. It is worthwhile to notice the excellent agreement between the shapes of the droplet from simulations and experiments (see figure (11) and (14) in reference [37]). The results are supported by a corresponding experimental work [38]. However, these results refer to a viscosity ratio of unity.

The method is extended to handle viscosity ratios different from unity. In [39] the viscosity ratio ranges from 0.1 to 10. The deformation of droplets is shown upon

numerous combinations with confinement ratios $2R/H$ from 0 (unbounded case) to 1.8. The work includes additionally selected results for the breakup case. The breakup case is systematically evaluated in [23] which presents numerical and experimental results showing a very good agreement for arbitrary combinations of λ and $2R/H$.

The topic of non-Newtonian fluids is also addressed using the BIM method in [40] which models the shear-thinning droplet with the Carreau-Bird law. The numerical investigation considers a droplet passing through a converging-diverging channel, which is an alternate configuration to study the elongation flow.

Further on, the problem of shear-thinning droplets in shear flows is addressed by Giraldo and his co-workers. The truncated law is implemented in [21] which studies the behaviour of shear-thinning droplets sheared by a circular confined Couette flow characterised by different capillary numbers. The droplet is not located in the middle of the walls and the exponents take values $n = 0.6$, 0.8 and 1 (Newtonian). Different λ^{NN} values below, equal and above unity are investigated. The results show that the deformation increases at lower exponents and the difference to the Newtonian droplet is closely related to the capillary number and weaker to the λ^{NN}.

Additionally, the mobility of droplets in both Newtonian and non-Newtonian (one component is power-law in specific) systems are investigated in [41] and [42], respectively. The term mobility is used to describe the relative motion of two interacting droplets one of which is placed initially in the middle of the domain and the other at a position close to one of the walls (see figure (2) in reference [42]). Then, the system is subjected to simple shear flow. However, simulations on the single *power-law* droplet case are not found in the literature.

For the sake of completion, numerical investigations using the BIM extend to the simulations for the Bingham fluid [43], the visco-elastic fluid [44] and the effects of surfactants on the surface of the droplet [45]. Also, the single droplet deformation travelling in a microchannel is studied in [46, 47] while the emulsion behaviour is studied in [48].

Finally, it is worth noting that the case of the single droplet in simple shear provides an ideal simulation ground for tests on adaptive mesh algorithms. An adaptive mesh approach is proposed in [49] to deal with large deformations, whereas [50, 51] focus on

big topological changes which occur during the breakup and coalescence procedures.

1.3.3.2 Volume of Fluid (VOF)

Focusing on the Newtonian fluids, the developed VOF algorithm in [52] is validated only for $\lambda = 1$, although the study considers more viscosity ratios. The study aims to identify the Reynolds numbers above which breakup occurs at a fixed Ca, namely the critical Reynolds numbers, and reveal the breakup mechanisms. Therefore, higher Re up to about 20 are also considered. The inertia effects on breakup are further studied in [53] which discusses the size of daughter droplets, and [54] which analyses the breakup mechanisms in more depth than in [52]. Noticeably, these studies reveal that the critical capillary number does not change at the Stokes regime flow, i.e. when $Re \leq 0.1$ (for example see figure (1) in [54]). Moreover, the confinement effect is addressed in [55], which compares the behaviour of an unconfined to a highly confined droplet, i.e. $2R/H \approx 0.7$, in Stokes flow and at $Re = 10$. The simulations in [55] are conducted using the method developed in [56] which tackles effectively the problem of the parasitic currents. Finally, the effects of inertia for non-unity viscosity ratios are studied in [57]. The Reynolds number increases up to $Re = 50$ while λ spans from 1 to 5. The illustration of the velocity streamlines inside the droplet reveals two vortices-like patterns in high Reynolds numbers as shown in [34].

With respect to *power-law* fluids, to the author's knowledge at the time of writing, no relative studies are available for the single droplet subjected to the simple shear case. However, the behaviour of a shear-thinning droplet, described by the Carreau model, passing through a contraction channel is compared to the Newtonian droplet in [58]. The findings show that a Newtonian droplet of a "characteristic" viscosity can be utilised to approach a shear-thinning one flowing in the same carrier fluid. Further more, the same work includes the opposite case; a Newtonian droplet suspended in shear-thinning carrier fluid. The behaviour of the droplet differs substantially to the previous setup.

To conclude, the VOF method is also used in simulations of Newtonian droplets in a Bingham carrier fluid [59, 60], and visco-elastic fluids [61, 62]. Also the role of surfactants on the shearing droplet is addressed in [63]. The VOF method developed

by Y. Y. Renardy and colleagues has been widely used in studying droplet dynamics [52, 53, 54, 55, 56, 59, 61, 62, 63].

1.3.3.3   Other Multi-phase Studies

Alternative numerical methods which are applied to simulate the single droplet problem are namely the phase-field (PF), the immersed boundary (IBM), the front tracking (FT) and the level-set (LS) methods. Although they are not as frequently encountered as the BIM and the VOF regarding the shearing droplet problem, for the sake of completion a brief mention of the most relevant works is included.

The PF method is adopted for two-phase shear flow simulations in [64]. The method is tested with respect to stability and accuracy against the Taylor theory and further on phase separation is investigated in 2D and 3D simulations. Simulations with the PF method are performed for the sheared droplet case in [65]. The deformation is investigated for unity viscosity ratio in $2R/H = 0.25$ and gives satisfying agreement with predictions from the Taylor theory (reported as "linear theory" in the specific article) and VOF results in [52]. To investigate both the breakup in the capillary number reaches the value of $Ca = 0.42$, and results are compared to experimental predictions. Again, the droplet subjected to simple shear flow is considered in [66]. In this work the computational method is first validated for Newtonian systems against the results reported in [34], and then the method is extended to study the behaviour of visco-elastic droplets in the same configuration. Additionally, this work discusses the droplet retraction and droplets coalescence features. Note that the phase-field method is also implemented in the LBM framework, which is described in *Chapter* 2.

The IBM formulation is used in [67] to investigate the effects of insoluble surfactants on a droplet under shear. Keeping density and viscosity ratios fixed to unity and the confinement ratio to $2R/H = 0.5$, the results on clean and surfactant-contaminated sheared droplets are contrasted. They show that the more contaminated the droplet the less it deforms. Also, the authors report that their investigation revealed that the capillary number has a more significant impact to the deformation of the droplet compared to other dimensionless numbers. The same numerical approach is used in [68] in which the aim is to develop a scheme in the IBM to guarantee volume conserva-

tion. After validations in $2R/H = 0.4$ for Reynolds numbers ranging from 1 to 100, this work focusses on the confinement effects for capillary numbers $Ca = 0.1$ to 0.8, while the Reynolds number and the viscosity ratio are set to unity in 3D simulations. Interestingly, the method is used in [69] to study the behaviour of compound droplets, i.e. the systems in which a droplet contains another droplet like those found in double emulsions. The density and viscosity ratios are set to unity and initial simulations are conducted to adjust the mesh refinement and the theoretical pressure jump. The investigation compares the final deformation shape of a single to a compound droplet, and furthermore considers in different capillary numbers the effects of: the ratio between *ambient fluid–outer droplet* and *outer–inner droplet* surface tensions, the radius ratio of the *outer* and *inner* droplets, the initial relative position of the *inner* droplet, and the wall confinement. The reported findings are versatile with respect to each parameter studied. The most relevant to the present research, is that the increase of the wall proximity leads to greater deviation between the behaviour of a single and a compound droplet. This finding indicates that wall effects enhance the complexity of droplet behaviour phenomena.

Furthermore, the behaviour of sheared visco-elastic droplets immersed in a Newtonian carrier fluid are simulated using the FT method [70, 71]. In [70] the deformation of a sheared droplet of unity viscosity ratio at $Re = 0.1$ is evaluated at different Ca and the method shows good agreement to the theory. Further on, the behaviour of the droplet at $Ca = 0.2$ and the critical capillary number are investigated for different Deborah numbers. The effect of the viscosity ratio on visco-elastic droplet is considered in [71]. Simulations are restricted to $Ca = 0.3$, and the findings show that the deformation decrease with the raise of the Deborah number up to a specific value which depends on the viscosity ratio. Above that value, the deformation increases.

Finally, the LS method is employed in simulations of droplets sheared in simple shear flow close to the breakup points, i.e. the capillary and Reynolds numbers are set as $(Ca, Re) = (0.25, 1.5)$, $(0.2, 4)$, $(0.15, 10)$, and $(0.1, 20)$ [72]. Their results agree well with the corresponding findings in [52]. This work includes also the investigation of the flow in the ascending bubble case.

1.3.3.4   Lattice Boltzmann Method (LBM)

The lattice Boltzmann method has the following four major multi-phase models: the colour-gradient introduced in [73], the interparticle-potential, frequently referred to as Shan-Chen model [74], the free-energy (or phase field) [75] and the mean-field theory. [76].

- Shan-Chen method

To the author's knowledge this method is the least used for the single droplet in shear problem. It is employed in [77] to perform 3D simulations, but most interestingly it is coupled with a finite difference scheme solver to handle visco-elastic fluids in [16]. The hybrid method is also used to evaluate the droplet generation in a T-junction micro-channel in two cases: i) Newtonian to-be-dispersed phase in visco-elastic continuous phase, and ii) the opposite setup [78].

- Free-energy or Phase-field method

This method is the most frequently used in numerical studies related to the single sheared droplet in the LBM framework.

The significance of the physics, or better stated the absence of them, in two dimensional simulations is examined in [79] which investigates the critical capillary numbers at zero and finite Reynolds numbers. The argument is that the droplet breakup at $Re = 0$ occurs not due to hydrodynamic but rather to numerical issues which would correspond to a molecular mechanism breakup. Two dimensional simulations are also performed in [80]. This study evaluates in a systematic way the dimensionless related parameters which ensure the suitability of the method to provide accurate results for the shearing droplet.

The effects of inertia are investigated with 2D and 3D simulations in [81]. This work mainly focusses on high Reynolds numbers, i.e. $Re = 1$, 10, 50, 100, while considering two confinement ratios $2R/H = 0.5$ and 0.8 and viscosity ratios above unity ($\lambda > 1$). The results show good agreement with results from experiments and the BIM. Again, the flow patterns show the same behaviour as reported in [34] using the BIM, and in [57] using the VOF. The study argues that the increase of the viscosity ratio does not

affect significantly the deformation of the droplet for moderate confinement ratios, i.e. $2R/H \leq 0.5$. However, at a confinement ratio $2R/H = 0.8$ higher viscosity ratios lead to larger deformations.

A more extensive study in which the Reynolds number varies from 0.0625 to 50 is presented in [82]. This study also extends the evaluation of the dimensionless numbers from 2D in [80] to 3D simulations. Simulations are performed in $2R/H = 0.25$ and the results are validated with the experimental and numerical results for $\lambda = 1$, before evaluating the droplet behaviour in viscosity ratios above unity. In addition, the critical capillary number is investigated.

Further investigations on the influence of the viscosity ratio, ranging from $\lambda = 0.1$ to 2, at $Re = 10$ are conducted in [83]. Simulations are performed in 3D at a confinement ratio $2R/H = 0.5$, which is mentioned as "sufficient to avoid wall effects".

A special reference needs to take place for the studies in [84] and [85] due to their modelling of the power-law fluids, although the single droplet case is not included. The viscous fingering phenomenon for different viscosity ratios, and most interestingly for different *power-law* fluids with their exponents n varying from 0.6 to 1.4 is examined in [84]. The generation of Newtonian droplets in T-junctions in which the carrier fluid follows the *power-law* formulation is evaluated in [85]. The *power-law* exponent n extends from 0.4 to 1.4 for these cases.

Finally, we mention that the phase-field method has been successfully employed to study the effects of surfactants [86], the droplet coalescence feature [87] and droplet generation in T-junction micro-channels [88].

- Colour-gradient method

This method is the earliest proposed to model multi-phase flows within the frameworks of the lattice Boltzmann method.

The Taylor theory is used to validate the method developed in [89] and [90]. Both works investigate the most suitable value for a numerical parameter referred to as "segregation parameter" (see in *Chapter* 2) to recreate the correct interfacial dynamics. The original objectives in [89] are the droplet breakup and the rising bubble while [90] discusses the droplet formation in cross junction micro-channels. In [91], the method

is extended to address the multiple droplets in shear problem. This work includes a module to prevent droplet merging.

   Additional works involve the implementation of techniques to deal with the contact line dynamics [92, 93, 94], which have improved the accuracy of the droplet formation simulations in asymmetric T-junctions [95]. Moreover, the method is applied to study the flow in porous media [96], and thermo-capillary effects on droplets moving in simple and complex micro-channels [97, 98].

1.4   Overview of the Present Work

This research focusses on the numerical investigation of a single droplet subjected in simple shear using the lattice Boltzmann method. The viscosity of the fluids is either constant or obeys the power-law model, equation (1.5). Three cases are considered:

1. a Newtonian droplet in a Newtonian matrix fluid; both fluids are assigned to constant viscosities connected by the viscosity ratio λ,

2. a Newtonian droplet in a power-law matrix fluid; the continuous phase is assigned to an arbitrary power-law exponent (n_c) and a consistency index (k_c) which is related to the dimensionless numbers describing the case. The droplet has a viscosity of equal value to this consistency index, i.e. $\eta_d = k_c$,

3. a power-law droplet in a Newtonian matrix fluid; the viscosity of the continuous phase (η_c) is calculated with respect to the dimensionless number, while the consistency index of the droplet is set to the same value, i.e. $k_d = \eta_c$, and the power-law index (n_d) is set again arbitrary.

The droplets are subjected to a wide range of shear intensity conditions, under which they obtain a steady shape or burst into smaller droplets. The findings refer to the confinement and viscosity effects. Besides the variations in deformation, orientation and the critical capillary numbers, the analysis focus on viscosity, velocity fields and stresses on the surface. The correlation among these properties is related to the underlying mechanisms of the droplet behaviour.

Although previous works successfully simulate the *Newtonian-Newtonian* system [16, 77, 80, 81, 82, 89], none of them examines systematically the impact of the relative parameters on the droplet behaviour, as done in this work.

Moreover, the data this work provides on the power-law fluid cases is a novel contribution to the literature. Even though the visco-elastic case has been numerically investigated, studies on the power-law area are still scarce.

In our tests the consistency index is considered equal to the viscosity of the Newtonian fluid counterpart at all times and the effect of the power-law index is evaluated. From a different perspective, the power-law case resembles a *Newtonian-Newtonian* system, i.e. both power-law exponents have an initial unity value $n_d = n_c = 1$, in which one component transits suddenly to the power-law state by assigning the value of n different from unity. This approach is genuinely numerical. Hence, our results could not be correlated to a tailored-designed experiment, because the shear rate imposed on the droplet would have to be extremely low. This artefact is discussed in *Chapter* 2, in Section 2.4.3.

In conclusion, the simulations are performed with an in-house LBM code which integrates the colour-gradient method to handle two-phase flows. The BGK operator is preferred due to its simplicity, and although it is stable in every parameter combination its suitability is questioned in low power-law exponents.

1.5   Outline of the Dissertation

The rest of the dissertation is structured as follows. *Chapter* 2 includes a general description of the numerical multi-phase methods mostly found in the literature regarding the sheared droplet case. Further on the numerical modelling used in this research is analysed.

The results and analyses on the simulations data are reported in *Chapters* 3 and 4. *Chapter* 3 discusses the Newtonian droplet sheared in both Newtonian and power-law fluids. The deformation and orientation are discussed along the developed velocity and stresses fields. Additionally, the critical capillary number is mapped on the confinement ratio in which the corresponding droplets are sheared and the breakup process is described. Further on, *Chapter* 4 investigates the behaviour of power-law droplets

sheared in a Newtonian liquid, and correlates their behaviour to Newtonian droplets.

Finally, *Chapter* 5 summarises our findings and suggests future applications. Complementary information is presented in the *Appendices*.

Chapter 2

Numerical Modelling

2.1 Introduction

The previous *Chapter* introduces the droplet shearing problem and states the parameters of interest. In addition, the most relevant available theoretical, experimental and numerical works are discussed.

This *Chapter* first describes briefly some of the numerical multi-phase models. Then it analyses the model developed in this work which includes both Newtonian and power-law fluids. Further on, the simulation settings are specified, i.e. the geometry and meshing, the initial and boundary conditions and the dimensionless numbers that describe the flow. Additionally, the calculation procedures of the deformation, orientation angle and stresses are described.

The *Chapter* concludes with a description of the evolution of the system upon shear when it reaches the steady state.

2.2 Multi-phase Methods

One of the main tasks of a multi-phase numerical method is to trace the position of the interface which separates two phases from each other. From this perspective, multi-phase methods are categorised into two approaches: '*interface tracking*' and '*interface capturing*'.

Interface tracking methods utilise numerical 'markers' at the interface to track its

motion. This category includes the boundary integral method (BIM), the front tracking (FT), and the immersed boundary method (IBM).

In the *interface capturing* methods, the interface evolves in a fixed Eulerian mesh along with the development of the flowfield. The interface is *captured* by an index function which evolves following a specific topological 'rule' in each method. The *interface capturing* methods include the volume of fluid (VOF), the level set (LS), the phase field (PF), and the lattice Boltzmann methods (LBM) which incorporate one of the models discussed in Section 1.3.3.4 and described further on in the following Section 2.2.3.1.

The representation of the interface is another essential feature multi-phase methods need to consider. A one-to-one *physical-to-numerical* representation is rather inaccessible, at least with the methods discussed here, because of the *physical* nature of the interface. The interface has a finite thickness of the order of $1\,nm$ [99], whereas droplets involved in microfluidic applications have a radius of at least several μm. The difference between the length-scales in the bulk area of a droplet and its surface is several orders of magnitude leading to a multi-scale problem.

Usually, two *numerical* methods are proposed to represent the interface: the zero (or sharp) and finite thickness interface methods. In the zero interface methods the surface resides only in one node in the normal direction and variables such as density and viscosity vary steeply during the transition from one phase to the other. On the other hand, finite thickness interface methods reserve a number of nodes for the interface through which the density and viscosity present a smooth transition.

The *interface tracking* BIM and FT methods, mentioned above, are considered as sharp interface methods. Additionally, IB methods have been implemented both as sharp or diffuse interface methods [100]. However, to the author's knowledge only sharp interface variations are applied to droplets [67, 68, 69], presented in the previous section 1.3.3.3. Also, an *interface capturing* method can be implemented as a sharp interface method, e.g. the interface reconstruction VOF (IR-VOF). Finite thickness interface methods include the colour function VOF (CF-VOF), the level-set (LS), the phase field (PF), and the lattice Boltzmann methods (LBM) which are described in the later Section 2.2.3.1.

Multi-phase modelling involves techniques to handle the integration of the interface tension and topological changes, to minimise the parasitic currents, and to model contact line. These issues are not discussed here, but are presented in comprehensive reviews especially for microfluidics and complex flows regarding the BIM in [101], the single-fluid Navier-Stokes representation methods (VOF, LS, PF, FT, IBM) in [102, 103], and the LBM in *Chapter 4* of [104].

2.2.1   Boundary Integral Method (BIM)

The core of the boundary integral method is the formulation of the partial differential equations (PDE's) of the mass and momentum conservation for each fluid into Green's type integrals. Hence, the methods is suitable for problems such as the potential theory and Stokes flow rather than Navier-Stokes flow [101]. The criticism that the method is not applicable in problems which include non-linear terms is addressed in [21, 42] which implement a dual reciprocity method to simulate shear-thinning fluids.

The integrals are solved for each fluid separately, using different techniques, e.g. the finite difference method (FD) [19, 36], the boundary element method (BEM) [35, 44, 40], the mean value theorem [37, 51], or the successive iteration method [34]. The interface is treated as a boundary where three conditions are imposed

- continuity of tangential stress components,

- balance of normal stress components with surface tension stresses, and

- continuity of tangential and normal components of velocity.

The explicit targeting of the interface enhances the accuracy of the BIM to benchmark-level precision results. The method is successfully employed to simulate cases which include viscosity differences, non-Newtonian fluids and the effects of surfactants, as described in *Chapter* 1. Moreover, the method is extended to address components of different density [101].

On the other hand, to capture big topological changes the method requires the implementation of sophisticated algorithms which increase the complexity of programming. Additionally, its prediction limits are narrowed by the input of a length-scale

which determines the site and time of pinch–off [87]. Finally, note that studies on the contact line dynamics are missing.

2.2.2   Volume of Fluid (VOF)

The Volume of Fluid is developed as both zero and finite thickness interface method. The main idea is to address the two immiscible liquids as a *single fluid* and introduce an order parameter which *captures* the interface. Hence, only one set of the Navier-Stokes equations is solved, in which the momentum equation integrates a volume-distributed force term to induce the local stress jump along the interface. The most used model is the continuum surface force (CSF) [105], but other methods are available [102]. Additionally, the order parameter evolves in space and time following an advection-type topological equation.

In the original, sharp-interface approach the order parameter is introduced in the form of an index function which obtains finite values in each node of the domain. To pinpoint the location of the interface a reconstruction procedure is required, hence the method is called interface reconstruction VOF (IR-VOF). One of the drawbacks is that considerable efforts are required to provide an accurate representation of the surface, especially in three dimensions. Therefore, another VOF approach considers a replacement of the index with a continuous 'colour' function, hence the name colour function VOF (CF-VOF) [102]. The surface is captured through a diffusive/finite thickness interface of a certain thickness hence no reconstruction algorithm is required.

The method can handle cases in which the components have different densities [106] or viscosities, as described in *Chapter* 1. Shear-thinning, Bingham and viscoelastic fluids, as well as the integration of surfactants effects modelling [107, 108] are also within the capabilities of the VOF. Finally, although VOF originated from the macroscopic point of view, it can be extended to deal with contact line dynamics successfully by adapting slip-velocity boundary conditions and integrating mesh adaptation and refinement techniques at the three-phase meeting sites [109].

The main difficulty in employing a VOF method lies in the development of a suitable scheme to solve the order parameter evolution equation while providing stability and accuracy. Despite this downside, in-house codes [52, 59], commercial and open-source

softwares, e.g. Ansys Fluent and CFX, OpenFOAM, implement the method broadly due to its robustness and the inherent volume and mass conservation, see [102] for a review.

2.2.3   Lattice Boltzmann Method (LBM)

The above methods solve directly the Navier-Stokes equations. On the other hand, built upon "microscopic models and mesoscopic kinetic equations" [110] the lattice Boltzmann method can incorporate surface dynamics, i.e. modelling the surface tension, in an intuitive way comparing to the aforementioned methods. Hence, "the interfaces emerge from the underlying dynamics" [111], and no additional techniques are required to detect pinch-off related events, while the accuracy is only a matter of resolution [87].

Although the method is a discretised form of the Boltzmann model equation, it is proved that it can retrieve the Navier-Stokes equation through a multi-scale (Chapman-Enskog) analysis [110]. Additionally, emerged as an alternative to CFD, the LBM can be regarded as an explicit Navier-Stokes solver in the near incompressible limit, and therefore no iterative procedure and no pressure correction algorithm is needed [112].

The key element of the method is the representation of the fluid as assemblies of pseudo-particles which are described by particle distribution functions $(f(\vec{r}, \vec{u}, t))$. These functions show the probability of particles residing in specific sites to move with specific velocities at a certain time. The main task of the method is to track the evolution of these distribution functions which consist of two mechanisms: the *streaming* and the *collision*.

The discretised form of the Boltzmann model equation incorporates functions $f(\vec{r}, t)$ which are embedded on a lattice of specific lengths and directions (see figure (2.1)). A simplified version, adopted in this research, forces the functions to *propagate* at a neighbour node at the next time step in predetermined paths of specific directions as described in equation (2.30). Although this choice simplifies the method, it prevents from simple implementations of body-fitted coordinates and adaptive time marching [113]. Also, the conversion from the microscopic lattice to the physical units is not a straightforward task, as shown in Section 2.4.3.

After the *streaming step* the functions undergo the *collision step*; they are forced to

relax towards specific Maxwellian type functions, namely the equilibrium distribution function (f^{eq}), at certain rate. The simplest relaxation operation is to introduce a single relaxation rate, which is related to the viscosity of the fluid, for all distribution functions, a method called Bhatnagar-Gross-Krook (BGK). The *collision step* covers up to two thirds of the entire computational process [114]. However, due to the local character of the calculations the method is easy to parallelise, comparing to other methods. Moreover, its ability to easily handle boundary and initial conditions because of the simplicity of the bounce-back and reflection patterns [115] renders it a preferable option to simulate flows in complex geometries.

Comprehensive reviews on the lattice Boltzmann method are found in [110, 116] and more recently in [112, 115], which also include discussions on the multi-phase models. Note that the colour-gradient method is only briefly described in [112] and not at all in [116, 115]. Further discussions focussed on the multi-phase models are included in [117, 118] which evaluate and compare their efficiency and suitability in porous media applications.

2.2.3.1 Multi-Phase LBM

The treatment of a second fluid involves an additional set of distribution functions. The following part describes the most frequently encountered multi-phase methods implemented in the LBM, namely the interparticle/pseudo-particle potential or Shan-Chen, the free-energy or phase-field (also referred to as the 'Oxford' model), the mean field (He-Shen-Zhang), and the colour-gradient (also called "chromodynamic").

• Shan-Chen model

The method is introduced in [74] and it is first used to simulate a droplet in simple shear flow in [77]. Each fluid, or phase, is monitored separately by individual sets of distribution functions, thus the independent calculation of densities and velocities in each component. The key element of the method lies in the representation of the interaction between the particles of the different components, or phases. An interparticle potential, which is a function of the density, is introduced and it models the force acting on a specific node towards the separation of species, or phases. This force is implemented

in the evolution of the distribution functions and used to update the velocities.

Due to its conceptual and programming simplicity the method is preferred over the other LBM multi-phase methods [115], and is chosen to be integrated in hybrid codes, e.g. with a finite differences method to model visco-elastic effects [16]. Many studies focus on widening the density difference ratio in which the method can be applied. The aim is to improve either the force relation to the interparticle potential [119], or the incorporation of the force term to the equilibrium distribution function [120].

Another strong point of the method is that it can model high density ratios ($\rho_d/\rho_c \sim$ 1000:1) [115]. Even more, the main criticism that the surface tension cannot be freely adjusted, as it depends on the density difference, is addressed in [121] which proposes a suitable additional term to the interparticle potential. Finally, the wetting phenomena are approached by introducing an additional interaction potential between the fluid and the solid-wall phases [122].

However, the method in its original BGK version is not suitable to simulate flows where the viscosity ratio exceeds 10:1. The observation of a mixing tendency is mentioned in [123], while the inapplicability of the method is further analysed in [117]. To extend the method in viscosity ratios 1000:1 higher-order isotropy in the evaluation of the fluid-fluid forces and MRT formulations are needed [124].

- Free-energy or Phase-field

The method is first proposed in [75], as an alternative to the colour-gradient and Shan-Chen models. Its main objective is to address the equilibrium state of a fluid from a thermodynamic point of view by encompassing a free-energy functional to describe the fluid behaviour. Although, note that the Shan-Chen can be characterised as "pseudo-free-energy" [125].

The original idea in [75] is to introduce a second set of distribution functions (g) and assign it to recover the density difference between the two fluids. Later works replace the density difference with the order parameter which, similar to the colour function, reflects the fraction of the dispersed fluid in the mixture [80, 86, 82]. The order parameter is also referred to as phase-field, a term which is attributed to the set of values the order parameter can obtain. Hence, the method is called interchangeably

as free-energy or phase-field in the literature. Note also that the phase-field falls into the category of the diffuse-interface models [64].

To describe the correct dynamics of the mixture, the second moment of g includes terms of the chemical potential which is derived from the free-energy functional as the "variational derivative of the free energy functional with respect to the order parameter" [86]. Additional to the chemical potential, the pressure tensor is also formulated following the free-energy functional. Regarding the surface tension, it is linked to the excess of the free energy per unit area, and is expressed in terms of a constant, found in the free energy functional, and the thickness of the interface.

The method can recover the Navier-Stokes equation, in which the conservation of momentum equation includes a force term linked to the chemical potential and the order parameter, and the Cahn-Hilliard equation to describe the evolution of the order parameter. Although the method is thermodynamic consistent, its main drawback is the lack of Galilean invariance [116, 126].

In the free-energy approach method a Poisson equation is actually solved to address the pressure difference in [127]. The method is tested successfully in problems considering a density ratio as large as 1000:1. A later work integrates the visco-elastic effects of a fluid that follows the Maxwellian model [128]. However, the solution of the Poisson equation harms the computation efficiency and simplicity of the LBM. This issue is addressed in [129] in which the method proposed does not only improves the efficiency, but the authors support that it also deals with the Galilean invariance; a statement verified in [130].

Moreover, the contact line dynamics can be approached by modifying the force term in the momentum conservation equation [131] (*Chapter 3 p.* 38 therein) and is implemented to enhance the accuracy in droplet generation in T-junctions simulations [88]. An additional significant feature is that the thermodynamic treatment of the interface allows the coalescence to occur 'naturally' without the need of an 'a-priori' criterion to specify a length condition [87]. Further more, the versatility of the free-energy functional allows it to be adjusted appropriately to encompass the effects of surfactants [86]. Finally, the method is proved to be suitable to simulate viscosity ratios below and above unity [83], and power-law fluids by adjusting the relaxation

parameter [84, 85].

On the other hand, the method is criticised to show droplet dissolution in conditions where the thickness of the interface is not small enough comparing to the droplet radius (a ratio adjusted by the Cahn number) [102]. Characteristically, it is shown in [82] (see figure (6) therein) that due to diffusion the interface occupies remote nodes from the bulk of the interface. The same study, along with [80], further shows that the stability and accuracy of the method depends, besides Re, Ca and λ, on two additional numerical dimensionless parameters which have to be properly adjusted, i.e. the ratio of interface thickness over the radius of the droplet namely the Cahn number, and the interface Peclet number that relates the advection to the chemical potential diffusion time scale.

- Mean-field theory

This method is developed in [76]. The distribution functions are forced to recover the pressure rather than the density rendering the method suitable for incompressible flow although limited to moderate density ratios. The surface effects are addressed with an intermolecular approach resembling the idea in the Shan-Chen method. Hence, the method is treated as an extended Shan-Chen approach for incompressible flows [116]. In other works the same method is categorised as a phase-field method [115].

- Colour-gradient

This method is first proposed to deal with the segregation in [73]. The idea is to introduce two sets of distribution functions for each fluid, namely 'red' and 'blue', which evolve individually. Close to the interface a perturbation term models the surface effects, i.e. generates the interfacial tension [111]. Instead of the perturbation term a CSF can be implemented [89, 97, 132, 133] (also in the present work see the following *Section*). In this approach, the sum of the 'red' and 'blue' distribution functions defines a total distribution function which follows the *collision* step. The *streaming* step involves both sets of distributions functions for each fluid, which zeroth moments produce the density of each fluid. A very significant contribution to the method is the re-colouring algorithm introduced by Latva and Kokko [134] which ensures the smooth

evolution of the diffusive interface and tackles the issue of the stagnation of the interface referred to as lattice pinning.

The idea is similar to the CF-VOF method. However, in the case of the colour-gradient LBM instead of an advection equation which governs the behaviour of the colour function, the colour function arises through a relation between the individual fluid densities, which is described in the following Section.

A distinctive feature of the colour-gradient model is that due to the individual coloured distribution functions the model "is only able to simulate completely immiscible fluids" and therefore no diffusivity is observed at the surface [117]. Hence, the interface is captured only within a finite number of lattices preserving the droplet from dissolution, and furthermore the Peclet and Cahn numbers do not need to be fine-tuned as in [80, 82]. In addition, the method is successfully extended to deal with contact line dynamics even for the cases of large viscosity ratios [94].

Moreover, the method can handle density ratios up to 1000:1 for stationary bubbles by implementing a suitable perturbation operator. However, instabilities occur for the rising bubble problem at much smaller ratios (100:1) [89]. Note that similar works which implement the CSF do not address the suitability of the colour-gradient method in high-density ratios.

Finally, heuristic-means schemes can be incorporated in the method to recreate the attractive/repulsive interactions between droplets [91, 135].

In this research the colour-gradient is preferred over the Shan-Chen due to the evidently significant effort needed by the latter to simulate flows in large viscosity ratios. Moreover, although both colour-gradient and free-energy methods present similar results in layered-Poiseuille and viscous fingering flows, the colour-gradient method produces sharper interface and better accuracy [117]. Also, taking into consideration that our research does not involve high density ratios or additional surface effects besides the breakup, i.e. surfactants or coalescence, we choose the colour-gradient method to conduct simulations. An additional benefit is that the Peclet and Cahn numbers do not need to be set.

To the author's knowledge, studies which implement the colour-gradient LBM model to systematically address the effect of the capillary number, the viscosity ratio and the

degree of confinement in droplet deformation and breakup are not reported. In particular, the colour-gradient LBM is used as our simulation tool because of its advantages such as low spurious currents, high numerical accuracy and strict mass conservation for each fluid which have been demonstrated in recent works [94, 96].

2.3   Colour – Gradient Lattice Boltzmann Method

The previous section provides general remarks on multi-phase numerical models. This section discusses in detail the adopted numerical method developed specifically for the simulations of a droplet in shear. In the following analysis, note that in every equation the scalars and vectors vary with the position $(\vec{r})$ and the time (t) and the explicit dependence on $(\vec{r}, t)$ is omitted except otherwise stated. Also, the index notations α and β are used for the spatial Cartesian coordinates $(x, y$ and $z)$.

The colour–gradient lattice Boltzmann method proposed for the isothermal motion of two immiscible fluids in [133] integrates a continuum surface force (CSF) model [105] to describe the surface tension dynamics. This formulation considers the two phases as a single fluid, i.e. single-field formulation [102], with space-dependent properties and replaces the jump condition at the interface with an additional force that acts only in the interface region. Hence, the method, characterised also as an explicit Navier-Stokes solver [102, 104], solves one set of continuity and momentum equations

$$\frac{\partial u_\alpha}{\partial x_\alpha} = 0 \tag{2.1}$$

$$\rho \left(\frac{\partial u_\alpha}{\partial t} + u_\beta \frac{\partial u_\alpha}{\partial x_\beta} \right) = -\frac{\partial p}{\partial x_\alpha} + \frac{\partial T_{\alpha\beta}}{\partial x_\beta} + F_{S\alpha} \tag{2.2}$$

where ρ is the total density, $\vec{u}$ is the fluid velocity, p is the pressure, $\mathbf{T}$ is the deviatoric stress, and $\vec{F}_S$ the force in the vicinity of the interface which models the surface tension effects.

The deviatoric stress tensor obeys a simple constitutive law which links it to the shear strain rate $(\mathbf{S})$ through the viscosity

$$T_{\alpha\beta} = \eta \left(|\dot{\gamma}_{\alpha\beta}| \right) 2 S_{\alpha\beta} \tag{2.3}$$

where $2\mathbf{S}$ is equal to the shear rate tensor $\dot{\boldsymbol{\gamma}}$. The local shear rate magnitude is calculated as

$$|\dot{\gamma}_{\alpha\beta}| = \sqrt{\frac{\dot{\gamma}_{\alpha\beta}\dot{\gamma}_{\alpha\beta}}{2}} = \sqrt{2S_{\alpha\beta}S_{\alpha\beta}} \tag{2.4}$$

and $\mathbf{S}$ is defined as

$$S_{\alpha\beta} = \frac{1}{2}\left(\frac{\partial u_\alpha}{\partial x_\beta} + \frac{\partial u_\beta}{\partial x_\alpha}\right) \tag{2.5}$$

In equation (2.3) the viscosity is modelled by the power-law formulation, see equation (1.5) restated here for completion,

$$\eta\left(|\dot{\gamma}|\right) = k\left(|\dot{\gamma}|\right)^{n-1}, \tag{2.6}$$

where n is the power-law exponent and k is the consistency index with units $Pa\,s^n$ or $kg/m\,s^{n-2}$.

Clearly, the viscosity depends on the velocity gradients except in the case where the phases are Newtonian ($n = 1$). Hence, equations (2.5) and (2.6) are omitted in the calculations to decrease the simulations times, and a constant separate viscosity value is assigned to each fluid throughout the entire simulation.

The last term in equation (2.2) represents the interfacial tension force acting at the interface between the two fluids and is defined as

$$\vec{F}_S = \sigma\kappa\vec{n}\delta_\Gamma, \tag{2.7}$$

where σ is the interfacial tension, κ is the local interface curvature, $\vec{n}$ is the unit normal to the interface vector, and δ_Γ is the Dirac delta function used to localize the force explicitly at the interface, which should satisfy

$$\int_{-\infty}^{\infty} \delta_\Gamma dz = 1 \tag{2.8}$$

in order to recover properly the stress jump condition in the sharp-interface limit. Here z is the spatial location normal to the interface.

The key element of this method is that the interface capturing procedure differs substantially from the other multi-phase methods. Instead of solving a transport equation

for the volume fraction of each phase, it introduces two sets of distribution functions which represent the two immiscible fluids. Note that each fluid is assigned to a different set of k and n values in the implementation of power-law viscosity modelling described by equation (2.6). This versatility allows to model cases where liquids represent arbitrary power-law fluids.

Henceforth, the dispersed fluid is also referred to as 'red' and the continuous as 'blue'. The respective functions are defined as f_i^R and f_i^B, where the subscript 'i' denotes the velocity direction and the superscripts 'R' and 'B' refer to the red and blue fluids, respectively. Summing the two sets leads to the total distribution function:

$$f_i = f_i^R + f_i^B. \tag{2.9}$$

The zeroth moment of each set calculates the density of the respective fluid

$$\rho^R = \sum_i f_i^R, \quad \text{red fluid}$$
$$\rho^B = \sum_i f_i^B, \quad \text{blue fluid}. \tag{2.10}$$

Moreover, the method utilizes these partial densities to define the colour function, or stated as order parameter, which indicates the spatial distribution of the two fluids as

$$\rho^N = \frac{\rho^R - \rho^B}{\rho^R + \rho^B}, \quad -1 \leq \rho^N \leq 1. \tag{2.11}$$

Thus, the colour function captures an interface of finite thickness. The location where the colour function obtains the value $\rho^N = 0$ dictates the middle of the interface between the red and the blue fluid, further adopted as the droplet surface in the rest of the dissertation. Clearly, the total density of the fluid is the sum of the partial densities or the zeroth moment of the total distribution function:

$$\rho = \rho^B + \rho^R,$$
$$\rho = \sum_i f_i. \tag{2.12}$$

The total distribution function (f_i) undergoes a Bhatnagar-Gross-Krook (BGK)

collision step as

$$f_i^\dagger = f_i - \frac{1}{\tau}(f_i - f_i^{eq}) + \Phi_i, \tag{2.13}$$

where f_i is the total distribution function in the i-th velocity direction at the position $\vec{r}$ and time t, f_i^{eq} is the equilibrium distribution function of f_i, $f_i^\dagger$ is the post-collision distribution function, τ is the dimensionless relaxation time, and Φ_i is the forcing term. The equilibrium distribution function is obtained by a second-order Taylor expansion of Maxwell-Boltzmann distribution with respect to the local velocity $\vec{u}$:

$$f_i^{eq} = \rho w_i \left[1 + \frac{\vec{e}_i \cdot \vec{u}}{c_s^2} + \frac{(\vec{e}_i \cdot \vec{u})^2}{2c_s^4} - \frac{\vec{u}^2}{2c_s^2}\right], \tag{2.14}$$

where c_s is the lattice speed of sound, $\vec{e}_i$ is the lattice velocity in the i-th direction, and w_i is the weight factor. For the three-dimensional 19-velocity (D3Q19) model, seen in figure (2.1), the lattice velocity $\vec{e}_i$ and the weight factors are given by

$$\vec{e}_i = \begin{cases} (0,0,0)c, & i = 0; \\ (\pm 1, 0, 0)c, (0, \pm 1, 0)c, (0, 0, \pm 1)c, & i = 1, 2, ..., 6; \\ (\pm 1, \pm 1, 0)c, (0, \pm 1, \pm 1)c, (\pm 1, 0, \pm 1)c, & i = 7, 8, ..., 18, \end{cases} \tag{2.15}$$

$$w_i = \begin{cases} 1/3, & i = 0; \\ 1/18, & i = 1, 2, ..., 6; \\ 1/36, & i = 7, 8, ..., 18, \end{cases} \tag{2.16}$$

and the speed of sound $c_s = \frac{c}{\sqrt{3}} = \frac{\delta_x}{\sqrt{3}\delta_t}$ with δ_x and δ_t being the lattice length and lattice time step, respectively.

By defining $\vec{n} = -\frac{\nabla \rho^N}{|\nabla \rho^N|}$ and $\delta_\Gamma = \frac{|\nabla \rho^N|}{2}$, equation (2.7) can be further written as

$$\vec{F}_S = -\frac{1}{2}\sigma\kappa\nabla\rho^N, \tag{2.17}$$

where the local interface curvature κ is related to the unit normal to the interface by

$$\kappa = -\left[(\mathbf{I} - \vec{n} \otimes \vec{n}) \cdot \nabla\right] \cdot \vec{n} = -\nabla \cdot \vec{n}, \tag{2.18}$$

and $\mathbf{I}$ is the second-order identity tensor. With the interfacial tension force given by

equation 2.17, the forcing term Φ_i that is applied to realize the interfacial tension effect, reads as in [97]:

$$\Phi_i = \left(1 - \frac{1}{2\tau}\right) w_i \left(\frac{\vec{e_i} - \vec{u}}{c_s^2} + \frac{\vec{e_i} \cdot \vec{u}}{c_s^4}\vec{e_i}\right) \cdot \vec{F}_S \delta_t. \tag{2.19}$$

According to Guo et al. [136], the local fluid velocity should be defined to incorporate the spatially varying interfacial tension force

$$\rho\vec{u} = \sum_i f_i\vec{e_i} + \frac{1}{2}\vec{F}_S\delta_t. \tag{2.20}$$

Using the Chapman-Enskog multiscale expansion, equation (2.13) can lead to the Navier-Stokes equations in the low frequency, long wavelength limit with the pressure and the fluid viscosity defined by

$$p = \rho c_s^2, \tag{2.21}$$

$$\eta = \rho c_s^2 \left(\tau - \frac{1}{2}\right)\delta_t. \tag{2.22}$$

The partial derivatives required for the curvature and normal vector calculations are obtained using the 19-point compact finite difference stencil. For example, for a
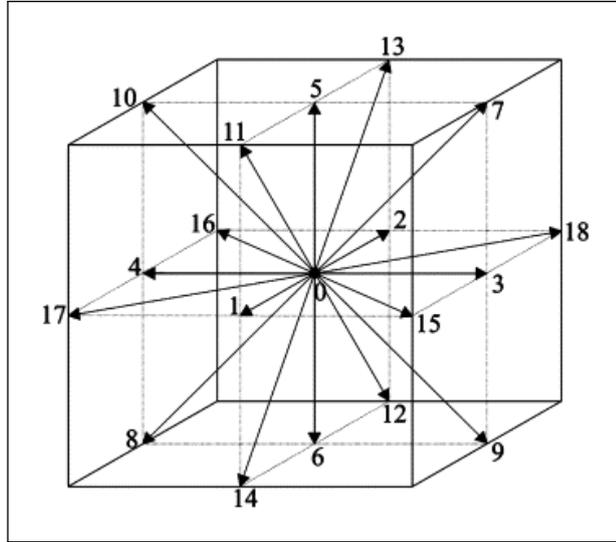
Figure 2.1: Schematic illustration of the three-dimensional, nineteen velocity (D3Q19) lattice.

variable ψ, its partial derivatives are calculated as

$$\frac{\partial \psi(\vec{r})}{\partial x_a} = \frac{1}{c_s^2} \sum_i w_i \psi(\vec{r} + \vec{e_i}\delta_t)e_{ia}. \tag{2.23}$$

This scheme can be utilised to calculate the shear rate tensor as well.

However, the components of the rate of strain tensor are calculated with a completely local scheme described in [137]:

$$S_{\alpha\beta} = -\frac{c_s^2}{2\rho c^2 \tau} \sum_i f_i^{(1)} e_{i\alpha} e_{i\beta}, \tag{2.24}$$

where $S_{\alpha\beta}$ is the strain tensor modified as in [92, 93]

$$S_{\alpha\beta} = \frac{1}{2}\left(\frac{\partial u_\alpha}{\partial x_\beta} + \frac{\partial u_\beta}{\partial x_\alpha}\right) + \frac{\delta_t}{4\rho c_s^2 \tau}\left(F_\alpha u_\beta + F_\beta u_\alpha\right) \tag{2.25}$$

and $f_i^{(1)} = f_i - f_i^{(eq)}$ is the non-equilibrium part of the pre-collision distribution function.

The implementation of this scheme provides a second order accuracy, similarly to the density and velocity [138].

To the author's opinion, the implementation of this scheme is the most important contribution to the development of the computational framework to introduce the power-law model in this research. The strain, and hence the viscosity, can be alternatively calculated by using equation (2.23) and the definition of the shear strain, i.e. equation (2.5). This approach was contrasted to the scheme using equation (2.24) in the single-phase Poiseuille flow for power-law exponents in the range of $n = 0.1$ to 4. Even though, the results showed some deviations from the analytical solutions for low exponents up to $n = 0.25$, both schemes produce comparable solutions.

These schemes were further tested in two-phase two dimensional simulations for the sheared droplet. Identical results were obtained using either scheme. Furthermore, while implementing equation (2.24) the calculations of the velocity gradient are avoided. Thus, no specific treatment in the message passing interface algorithms with respect to the velocity components is required for the domain decomposition practice.

Therefore the computational efficiency and parallelisation capability of the method are enhanced by using (2.24) when compared to the implementation of equation (2.23).

Equation (2.24) has been implemented in single phase studies [139, 140, 141, 142]. The scheme is also used in two-phase cases [84, 85] which investigated the viscous fingering and droplet formation involving power-law fluids. Note that the LBM-MRT implementation has the ability to calculate the rate of strain tensor locally following a similar formulation [143, 144, 145].

A drawback in this approach is that the relaxation parameter depends on the shear rate implicitly through the relation

$$\tau = \frac{\eta \left(\left| \dot{\gamma}_{\alpha\beta} \left(S_{\alpha\beta} \left(\tau \right) \right) \right| \right)}{\rho c_s^2 \delta t} + \frac{1}{2} \tag{2.26}$$

As this relation is not linear, its solution requires an iterative method to calculate τ at the current time step. This would affect the computational efficiency of the method, thus the concurrent relaxation time value is assigned to the one of the previous time step. This practice does not affect the accuracy of the method [146], and is also adopted in our code.

To deal with unequal viscosities of the two fluids, the viscosity of the fluid mixture follows a harmonic mean average function to the index:

$$\frac{1}{\eta \left(\rho^N \right)} = \frac{1 + \rho^N}{2\eta^R} + \frac{1 - \rho^N}{2\eta^B}, \tag{2.27}$$

where η^R and η^B are the dynamic viscosities of the red and the blue fluids, respectively as in [84, 96, 147]. It is shown that the choice of equation 2.27 can ensure a constant viscosity flux across the interface, resulting into a higher accuracy than other choices [148]. Additionally, the viscosities η_R and η_B are calculated by equation (2.6) independently from each other, thus each fluid can be Newtonian or power-law.

Although the forcing term generates an interfacial tension, it does not guarantee the immiscibility of both fluids. To promote phase segregation and maintain a reasonable interface, the segregation (recolouring) algorithm of Latva-Kokko and Rothman is used [134]. It can overcome the lattice pinning problem and creates a symmetric distribution of particles around the interface so that unphysical spurious currents can be effectively reduced. Following Latva-Kokko and Rothman, the post-segregation (recoloured) dis-

tribution functions of the red and blue fluids are

$$
\begin{aligned}
f_i^R &= \frac{\rho^R}{\rho} f_i^\dagger + \beta \frac{\rho^R \rho^B}{\rho} w_i \cos(\varphi_i) |\vec{e}_i|, \\
f_i^B &= \frac{\rho^B}{\rho} f_i^\dagger - \beta \frac{\rho^R \rho^B}{\rho} w_i \cos(\varphi_i) |\vec{e}_i|,
\end{aligned}
\tag{2.28}
$$

where β is the segregation parameter and is set to 0.7 for numerical stability and model accuracy; φ_i is the angle between the colour gradient and the lattice vector $\vec{e}_i$, which is defined by

$$
\cos(\varphi_i) = \frac{\vec{e}_i \cdot \nabla \rho^N}{|\vec{e}_i| |\nabla \rho^N|}.
\tag{2.29}
$$

After the recolouring step, the red and blue distribution functions propagate to the neighbouring lattice nodes, known as propagation or streaming step:

$$
f_i^k(\vec{r} + \vec{e}_i \delta_t, t + \delta_t) = f_i^k, \quad k = R \text{ or } B,
\tag{2.30}
$$

and the resulting distribution functions are then used to calculate the densities of both fluids as in equation (2.10).

Concluding, we note that the method is programmed in an in-house *Fortran* code. The collision and streaming procedures were developed within the frameworks of previous projects, and furthermore the unequal viscosities function and the recolouring algorithm were previously tested.

The author's contributions to the computational development were focussed on the development and verification of the forcing scheme described earlier in this Section (equation 2.19) in validations with respect to the force driven Poiseuille flow, the implementation of the half-way bounce-back condition which is described in the following Section 2.4.1, and the power-law modelling which is earlier discussed in the present Section.

2.4   Simulations Setup

2.4.1   Geometry, Mesh and Boundary Conditions

The computational domains are simple three dimensional cuboids on the Cartesian coordinate system. The length, depth and height of a domain are assigned to the x-, y- and z- directions, respectively. Each domain is meshed by a structured orthogonal grid and the D3Q19 lattice is implemented. Also note that, in the rest of this work, a cross sectional slice in the $x - z$ plane positioned in the middle of the y- axis, shown with blue in figure (2.2), will be referred to as the '$x - z$ middle plane', or plainly 'middle plane'. In this characteristic plane the vector and tensor properties are nullified in the y- direction due to the symmetry.

In the lattice Boltzmann method the boundary conditions specify the unknown incoming distribution functions at the numerical mesh edges. The simulations consider two types of boundaries: openings normal to the x- and y- and solid walls in the z- direction. Openings are modelled with 'standard' periodic boundary conditions [149] which practically consider a periodic array of droplets in shear, and are "legitimate when the boundary effects are negligible " [147].
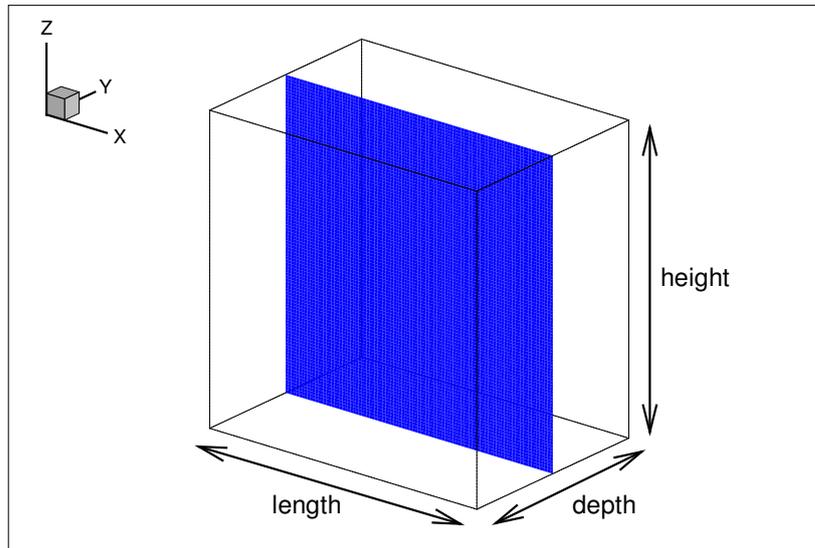
Figure 2.2: Simulation geometry. The blue plane illustrates the '$x - z$ middle plane' described in the text.

At the walls the half-way bounce-back in the z- direction is implemented as in [150]:

$$f_i(\vec{r}, t + \delta t) = f^{\dagger}_{ops(i)} + 6w_i\rho\frac{\vec{e}_i \cdot \vec{u}_w}{c}, \tag{2.31}$$

where $\vec{u}_w$ is the moving velocity of the solid wall and $ops(i)$ stands for the distribution function which has opposite direction to $\vec{e}_i$. The setup imposes the walls velocities $\vec{u}_t = (U_w, 0, 0)$ for the top wall and $\vec{u}_b = (-U_w, 0, 0)$ for the bottom wall throughout the entire simulation duration.

The initial droplet radius is fixed to 20 lattice units (l.u.) to keep the same droplet and interface resolution in all simulations. Also, grid independence tests in a typical shear test showed a variations in the deformation parameter of $4.5\,\%$ comparing to a droplet of $10\,l.u.$ and below $1\,\%$ for $R = 30\,l.u..$ The droplet is considered sufficiently isolated for length and depth of 100 and 71 $l.u.$, respectively. However, in high intensity shearing, i.e. high capillary number cases, a droplet elongates to an extent where one tip of the droplet re-appears in the other side of the domain via the periodic boundary conditions. This artefact can lead the two sides of the same droplet to merge where instead the droplet would break. Hence, to avoid this situation the length increases and can reach up to 492 $l.u..$ The height varies within a range of 51 to 223 $l.u.$ to obtain different confinement ratios from $2R/H = 0.18$ to 0.8.

2.4.1.1   Domain size effect in the periodic boundary condition

To assess the effect of the periodic boundary conditions with respect to the domain size in the shear direction, two droplets are tested in two domains with lengths (i) $100\,l.u.$, and (ii) $200\,l.u..$ The confinement ratio is set to $2R/H = 0.4$, and the capillary number is adjusted to $CA = 0.5$ to investigate the most shear intense case. The droplets are consisted of power-law fluids with exponents $n_d = 0.75$ and $n_d = 1.25$, which are correlated to very high- and low- viscosity Newtonian droplets, respectively. This correlation is discussed in *Chapter* 4.

Figure (2.3) illustrates the droplets in the $x - z$ middle plane, with solid lines for $n_d = 0.75$ and dashed for $n_d = 1.25$. The respective droplets and domains are depicted with red in case (i) and blue in case (ii). More specifically, in figure (2.3(a)) the droplets are contrasted along with the domain sizes, whereas in figure (2.3(b)) the area close to

the droplets is enlarged to observe the differences of droplets shapes in more detail.

The deformation parameters and the orientation angles are calculated as described in the following Section 2.4.5. For $n_d = 0.75$ the deformation between cases (i) and (ii) deviates by 1.0 % , and the orientation angle by almost 0.2 degrees. For the droplets of $n_d = 1.25$ the deviation in the deformation is around 0.1 %, and the angle differs by less than 2 degrees.

Therefore, the length of the domain is selected to $100 \, l.u.$, for the cases where steady deformation is expected, without affecting significantly the final observed droplet.

2.4.2   Initial Conditions and Fluid Properties

In all the simulations, the initial droplet is in the centre of the domain. The droplet includes only red fluid, hence in its interior $\rho^R = 1$ and $\rho^B = 0$. On the contrary, in the matrix fluid, which consists only of blue fluid, the respective colour function are $\rho^R = 0$ and $\rho^B = 1$. Also, each fluid is assigned with an individual viscosity evolution applied by equation (2.6).

Initially, the velocity everywhere in the domain is $\vec{u} = (0, 0, 0)$. At the first time step the velocity on the top and bottom walls are set to $\vec{u}_t = (U_w, 0, 0)$ and $\vec{u}_b = (-U_w, 0, 0)$, respectively. The magnitude of the velocity at the walls (U_w) and the viscosity of the continuous fluid (η_c) are imposed considering the Reynolds (Re) and the capillary (Ca) numbers, along with the height of the domain. As a reminder, the dimensionless Re and Ca numbers are defined using the properties of the *continuous-matrix* fluid as

$$Re = \frac{\rho \dot{\gamma}_0 R^2}{\eta_c} \tag{2.32}$$

$$Ca = \frac{\dot{\gamma}_0 R \eta_c}{\sigma}. \tag{2.33}$$

The magnitude of the shear rate is derived, with some manipulations, as

$$\dot{\gamma}_0 = \sqrt{ReCa\frac{\sigma}{\rho R^3}} \tag{2.34}$$
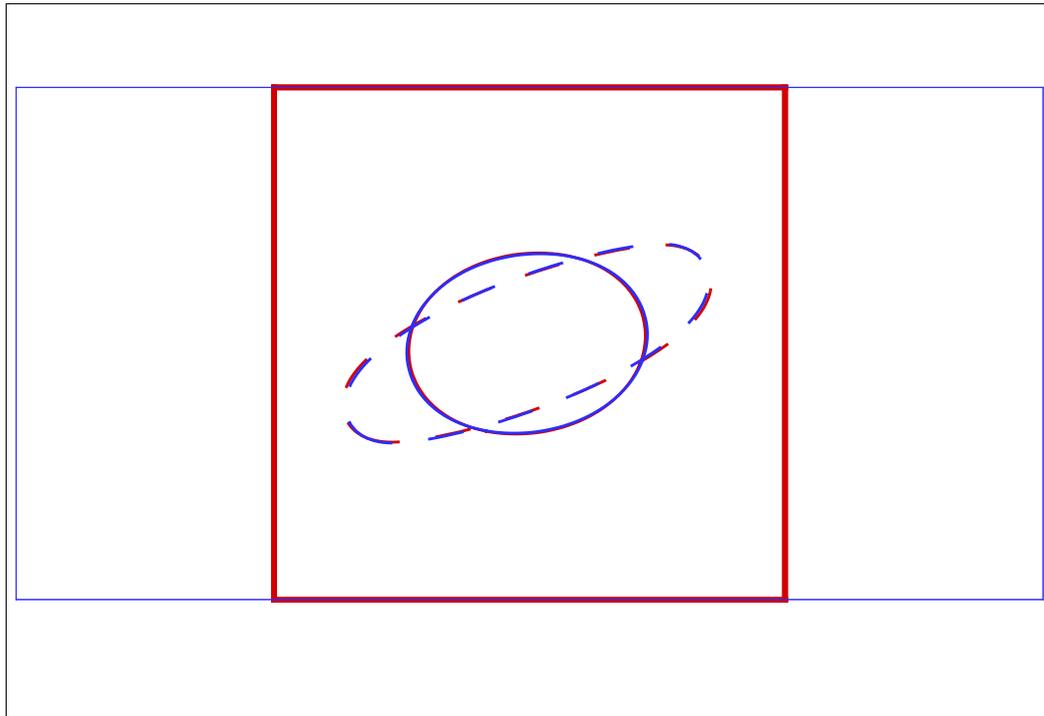
(a) Full domain in the $x - z$ middle plane.
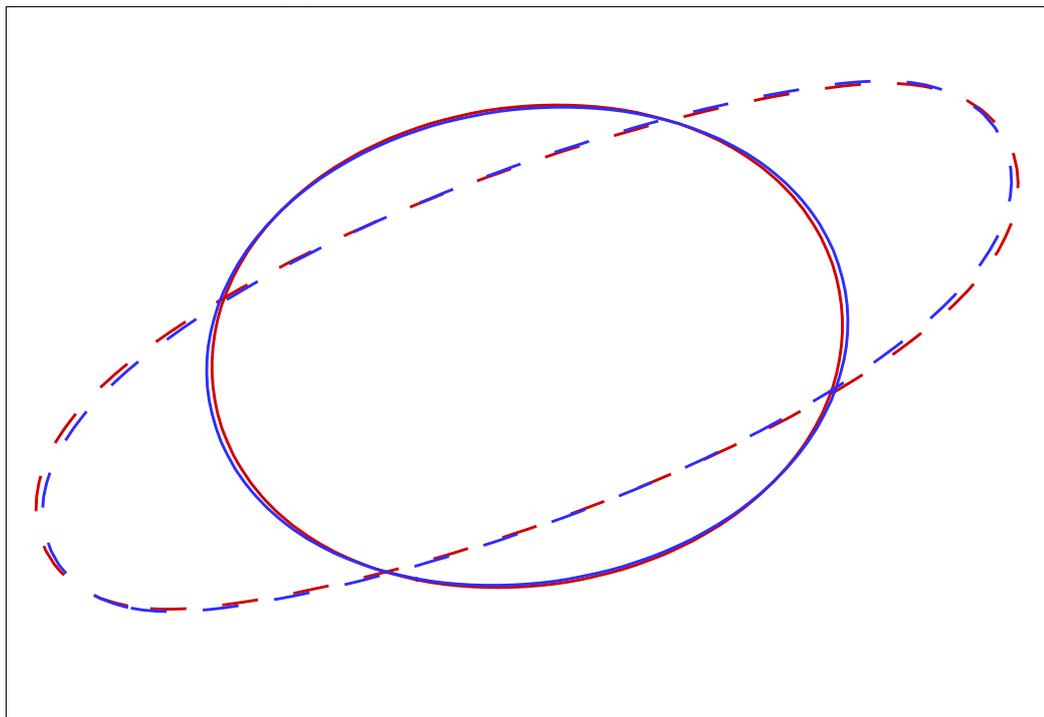
(b) Enalrged area close to the droplets region.

Figure 2.3: Droplet shape comparison for $n_d = 0.75$ (solid lines) and $n_d = 1.25$ (dashed lines), in domains with lengths of (i) 100 $l.u.$ (red), and (ii) 200 $l.u.$ (blue).

and the velocity magnitude on the walls (U_w) is calculated from

$$\dot{\gamma}_0 = \frac{U_w}{H/2} \Leftrightarrow U_w = \frac{\dot{\gamma}_0 H}{2} \tag{2.35}$$

For the range of parameters used the imposed velocity is low enough to fulfil the criteria of low Mach number, i.e. $Mach < 0.15$ [131] (see therein: *Chapter* 3, *p.* 41, *equation* 3.34). In a specific example where $Ca = 0.2$, $Re = 0.1$, $2R/H = 0.4$ the Mach number is ≈ 0.0043. Note that, even for a large capillary number, e.g. $Ca = 1$, the Mach number is lower than $Mach \leq 0.01$.

Finally, the viscosity of the *continuous-matrix* fluid (η_c) is

$$\eta_c = \sqrt{\frac{Ca}{Re}\rho\sigma R}, \tag{2.36}$$

and the viscosity of the droplet arises from the viscosity ratio

$$\eta_d = \lambda\eta_c. \tag{2.37}$$

Complementary, the numerical method can handle cases where a droplet is made of power-law fluid, which is discussed in *Chapter* 4.

On the other hand, when the matrix fluid is characterised as power-law the Reynolds and the capillary numbers cannot be defined adequately due to the variation of the viscosity term [151]. The following approach describes the adaptation of the numerical method to these cases.

Starting from the single phase, an analogous expression to the *Reynolds* number for the non-Newtonian fluid is derived as in [139]:

$$Re = \frac{\rho U_0^{2-n} L^n}{k}. \tag{2.38}$$

Note that in [139] Re is expressed in terms of the kinematic viscosity and L is a characteristic length, while the characteristic velocity was the maximum (u_{max}). Clearly, when the exponent is unity $n = 1$ the fluid is Newtonian.

For the two phase simple shear flow the viscosity, consistency index and power-law

are noted as η_c, k_c and n_c, respectively. The definition for the *Reynolds* number is

$$Re = \frac{\rho(\dot{\gamma}_0 H/2)^{2-n_c} H^{n_c}}{k_c} \Leftrightarrow$$

(replacing H with R, and dropping the 2 in the denominator of the term H/2)

$$Re = \frac{\rho \dot{\gamma}_0^{2-n_c} R^2}{k_c}, \quad \text{or}$$

$$Re = \frac{\rho \dot{\gamma}_0 R^2}{\eta_c}, \tag{2.39}$$

using the shear rate $(U_0 = \dot{\gamma}_0 H/2)$ and the droplet radius as characteristic properties. Hence, equation (2.39) is the same as equation (2.32). In addition, the capillary number may take the following forms depending on whether we use the viscosity or the consistency index:

$$Ca = \frac{\dot{\gamma}_0 R \eta_c}{\sigma} = \frac{\dot{\gamma}_0 R \left(k_c \dot{\gamma}_0^{n_c-1}\right)}{\sigma} = \frac{\dot{\gamma}_0^{n_c} R k_c}{\sigma}. \tag{2.40}$$

Therefore, the magnitude of the shear rate imposed is

$$\dot{\gamma}_0 = \sqrt{ReCa\frac{\sigma}{\rho R^3}}, \tag{2.41}$$

as in equation (2.34). The consistency index can be calculated as:

$$k_c = Ca\frac{\sigma}{\dot{\gamma}_0^{n_c} R}. \tag{2.42}$$

and the viscosity can be found either by the power law definition or as:

$$\eta_c = Ca\frac{\sigma}{\dot{\gamma}_0 R}. \tag{2.43}$$

In the simulations, the viscosity of the Newtonian droplet (η_d) equals to the consistency index of the matrix fluid (k_c). Consequently, the characteristic parameters i.e. Re, Ca and $\dot{\gamma}_0$, match in a consistent manner between the shearing in Newtonian and power-law matrix fluids.

Finally, note that the surface tension is considered as an adjustable parameter and is set to $\sigma = 0.001$ to minimize spurious currents.

2.4.3   Units Conversion

The usual practice in the lattice Boltzmann method (LBM) framework is to consider unity microscopic length (δ_x) and time discretisations (δ_t). The length is represented by lattice units noted with $l.u.$ and one δt corresponds to the duration from one timestep to the next (or previous). The conversion of lattice units to physical units involves specific length, mass and time scales noted as L_0, M_0 and T_0, respectively. The physical length a lattice cell represents links to L_0, while the mass of the fluid contained in a grid cell is indicated by M_0. T_0 associates the time step to a physical time duration. Here, the conversion is described in such a way that lattice properties correspond to practical physical units used in the literature. The physical quantities are denoted with the subscript '$phys$', and only in this section the computational counterparts carry the subscript 'LBM'

The first step is to decide an appropriate L_0. In our simulations the droplet is set to $R = 20\, l.u.$. Following the experimental work in [20], the droplet size varies between 80 to 400 μm to achieve different confinement ratios with a fixed walls width of 1000 μm. Thus, to represent a droplet within these limits and without affecting the general scope of the units conversion procedure, we choose *for this example* $L_0 = 10^{-5}\, m/l.u.$. Hence, a droplet of $200\,\mu m$ is considered. This choice correlates to a confinement ratio $2R/H = 0.4$ which corresponds to a computational height of $100\, l.u.$. Notice, that L_0 can change to accommodate units conversion related to different confinement ratios.

Besides the lattice cell and the time step, the density in the LBM is also set to unity, i.e. $\rho_{LBM} = 1$, whereas a typical physical density (e.g. water) is $1000 kg/m^3$. The scaling for the mass is

$$M_0 = \rho_{phys} L_0^3 = 10^3 \left(10^{-5}\right)^3 = 10^{-12}\, \frac{kg}{l.u.^3}, \qquad (2.44)$$

i.e. the liquid 'weighs' $10^{-12}\, kg$ in each cell.

Further on, the viscosity range of the matrix liquid may vary over many orders of magnitude; for example the viscosity of 'PIB Parapol 1300' used in [20] is $101\, Pa\, s$, while water has a viscosity of $0.001\, Pa\, s$ (at $20\,°C$). In this example, a fluid of $\eta_{phys} = 0.034\, Pa\, s$ is chosen. The physical and computational quantities (of density and viscos-

ity) are correlated through the following expressions obtained from [131] (see therein: *Chapter* 3, *p*. 42, *equation* 3.35) which include the length and time scales:

$$3\frac{\eta_{LBM}}{\rho_{LBM}} + 0.5 = 3\frac{\eta_{phys}}{\rho_{phys}}\frac{T_0}{L_0^2} + 0.5 \Leftrightarrow$$

$$T_0 = \frac{\eta_{LBM}}{\rho_{LBM}}\frac{\rho_{phys}}{\eta_{phys}}L_0^2, \quad \text{or}$$

$$T_0 = \frac{\eta_{LBM}}{\eta_{phys}}\frac{M_0}{L_0} \quad (2.45)$$

Equation (2.36) dictates that the viscosity depends on Ca, Re and σ. Considering a case with $Ca_{LBM} = 0.2$, $Re_{LBM} = 0.1$ and $\sigma_{LBM} = 0.001$, the viscosity is calculated as $\eta_{LBM} = 0.2$. Keeping the aforementioned length and mass scales, solving equation (2.45) results in a time scale $T_0 \approx 5.8824 \times 10^{-7}\, s/\delta t$. Finally, the physical surface tension is recovered through [131] (see therein *Chapter* 3, *p.*42, *equation* 3.36)

$$\sigma_{LBM} = \sigma_{phys}\frac{T_0^2}{M_0} \Leftrightarrow \sigma_{phys} = \sigma_{LBM}\frac{M_0}{T_0^2}, \quad (2.46)$$

which leads to $\sigma_{phys} = 2.89\, mN/m$ in the specific case. This value is very close to the one reported in [20], i.e. $\sigma_{phys} = 2.8\, mN/m$.

Nevertheless, not all properties can be matched one-to-one from the computational to the physical values. The shear rate in the LBM in the specific example gives $\dot{\gamma}_{0_{LBM}} = 5 \times 10^{-5}$. The corresponding physical shear rate would be

$$\dot{\gamma}_{0_{phys}} = \frac{\dot{\gamma}_{0_{LBM}}}{T_0} = \frac{5 \times 10^{-5}}{5.8824 \times 10^{-7}} = 85\, s^{-1} \quad (2.47)$$

This value is considered large for the experiments of shearing droplet; for example the specific case in [20] the shear rate is computed $\dot{\gamma}_{0_{phys}} = 0.028\, s^{-1}$, which however utilises a fluid of $\eta_{phys} = 101\, Pa\, s$, and not $0.038\, Pa\, s$ as set here. Other reasonable values are reported within the range $0.08 - 1.6\, s^{-1}$ [152]. Note also that, the same case in [20] provides with $Re = 5.6 \times 10^{-5}$, whereas the shear rate in equation (2.47) recovers $Re = 0.1$ for the physical problem. This value is, also, five order magnitudes larger than the one reported in [23], which reports Re in the order of 10^{-6}.

This aspect is more troublesome upon the correlation between Newtonian and

power-law droplets, see *Chapter* 4. In a specific case of $Ca = 0.2$ the shear rate in the simulation is 5×10^{-5} in lattice units. In order to map Newtonian to power-law droplets the shear rate has to take the same value in the physical domain, i.e. to $5 \times 10^{-5} \, s^{-1}$ $n_d = 1.125$. This leads to a physical Reynolds number of $Re = 5.88235295 \times 10^{-8}$.

However, the problem is more of a computational artefact and the need to match exactly both Reynolds numbers in the computational and the physical domain is redundant. The representative physics in the Stokes flow regime are not governed by inertial effects, therefore the Reynolds number describing the physical problem needs only to be sufficiently small, i.e. $Re < 1$. This practice is adopted in other numerical frameworks.

For example, the VOF method is also used with low Re, i.e. $Re = 0.0625$ [52], and the results are compared with results obtained in vanishing Reynolds numbers cases. The comparison among such results is valid following the reference [36] which shows negligible differences in the results between vanishing values of Re and $Re = 0.1$. Note that the above specific works implements the BIM. Even more, it is shown numerically that below $Re = 0.1$ the critical capillary number varies insignificantly [54]. Additionally, the projection of a low experimental to a higher computational Reynolds number, e.g. $Re = 0.1$, increases the computational efficiency as it speeds up the simulations. In this work we choose the Reynolds number to be fixed at $Re = 0.1$ for all simulations. Our tests showed no differences with respect to the deformation parameter between simulations with $Re = 0.01$ and 0.1, while the simulation times of the former are considerably longer.

On the other hand, the most important features are captured by the interfacial effects, thus the capillary numbers between the experiments and simulations are required to match.

Finally, to evaluate the events between different systems the term of *time instant* (t^*_{LBM}) is introduced, which is defined as in [89]

$$t^*_{LBM} = \dot{\gamma}_0 t_{LBM}, \tag{2.48}$$

where t_{LBM} denotes the corresponding simulation timestep. The physical counterpart

is defined using the characteristic emulsion time [153] as

$$t^*_{phys} = \frac{t_{phys}}{t_{emul}}, \tag{2.49}$$

where $t_{emul} = \eta_{phys} R_{phys}/\sigma_{phys}$. The link between the experimental and the computational time instants is formed as follows

$$t^*_{phys} = \frac{t_{phys}}{t_{emul}} = \frac{t_{LBM} T_0}{\frac{\eta_{phys} R_{phys}}{\sigma_{phys}}} \Rightarrow$$

$$= \frac{t_{LBM} T_0}{\frac{\frac{\eta_{LBM} M_0}{T_0 L_0} R_{LBM} L_0}{\sigma_{LBM} \frac{M_0}{T_0^2}}} \Rightarrow$$

$$= \frac{t_{LBM}}{\frac{\eta_{LBM} R_{LBM}}{\sigma_{LBM}}} \Rightarrow$$

$$= \frac{t_{LBM}}{\frac{Ca}{\dot{\gamma}_{0LBM}}} = \frac{t_{LBM} \dot{\gamma}_{0LBM}}{Ca} \Leftrightarrow$$

$$t^*_{phys} = t^*_{LBM}/Ca, \quad \text{or}$$

$$t^*_{LBM} = t^*_{phys} Ca \tag{2.50}$$

In the rest of the dissertation the subscripts '*phys*' and '*LBM*' are omitted and sizes are referred to the computational values.

2.4.4 Time Duration

The duration of a simulation (Δt), i.e. the total number of timesteps (δ_t), depends on the resulting droplet regime. Thus, the duration cannot be determined before the simulation is performed, because the moment at which a droplet obtains a steady shape or breaks is not known 'a-priori'. Furthermore, the duration cannot be set the same in all simulations, as the droplet behaviour changes with varying capillary numbers. Evidently, when the steady state regime is indicated, i.e. by low capillary numbers, the number of iterations is smaller than when breakup is expected. Even within the same regime the number of iterations varies for each simulation along the capillary number.

To apply consistent time duration among all the simulations, the timestep at which a simulation terminates (t^{final}_{LBM}) corresponds to a specific termination *time instant*

(t^{*final}_{LBM}) for every capillary number through equation (2.48). Each *time instant* provides a consistent correlation for different systems in the same time scale. For example, in *Chapter* 3 figures (3.15), (3.16) and (3.17) show the breakup of different droplets where it can be deduced which droplet breaks at an earlier or later *time instant*.

Again, the determination of a t^{*final}_{LBM} value is not straightforward, thus we follow the results reported in [89] to estimate the duration beforehand. When the steady state regime is evident the duration is set to $t^{*final}_{LBM} = 10$ (time instants) in most cases. Providing an example, a simulation implementing a capillary number $Ca = 0.2$ leads to a shear rate magnitude $\dot{\gamma}_0 = 5 \times 10^{-5}$. Hence, the specific simulation runs for 200,000 timesteps. The pinch-off point occurs at a later time comparing to the steady state of the droplet. For simulation which investigate the critical capillary number the duration increases to $t^{*final}_{LBM} \geq 30$.

Finally, in all simulations the results are evaluated at the last time step. If a simulation does not produce clearly steady conditions or breakup, it is resumed from the last save point until one of the two results is obtained.

2.4.5   Deformation and Orientation Angle

The behaviour of the droplet is evaluated in terms of the deformation parameter and the orientation angle. Both parameters are calculated in the $x - z$ middle plane where the droplet obtains the maximum deformation. *In cases in which the final droplet reaches a steady state, its shape is considered as a perfect ellipse.* Additionally, in order to explain the behaviour among different droplets, a case with the following characteristics is defined as 'standard': $Re = 0.1$, $Ca = 0.2$, $\lambda = 1$ and $2R/H = 0.4$ for a Newtonian droplet confined in Newtonian matrix fluid.

Figure (2.4) plots the shape of a 'standard' droplet in a polar graph. The radial axes show the distance from the centre in $l.u.$, and the outer angular axes show the angle around the droplet surface. Red dashed lines OA and OB depict the longest (L) and the shortest (B) axes of the ellipse, respectively. The angle between the longest axis of the droplet and the zero angular axis defines the orientation angle θ. In figure (2.5) the unity viscosity ratio droplets are contrasted in all confinement ratios tested. Notice that the orientation angle for a droplet confined in $2R/H = 0.7$ (magenta line)

is higher than the orientation angle of the droplet in $2R/H = 0.6$ (orange line).

This behaviour is linked to the procedure with which the calculations are performed. The deformation and orientation of all droplets are measured in the post processing phase using the visualisation software *Tecplot*. The first step is to export the Cartesian coordinates of the points residing on the surface of the droplet, where $\rho^N = 0$, in the middle plane. Next, the distances of all these points from the centre O (x_O, z_O), which is known as an input in all simulations, are calculated. The highest and lowest values and the positions they occur are obtained thus detecting points A (x_A, z_A) and B (x_B, z_B). As mentioned above, the distance OA is assigned to the axis L and the distance OB is assigned to axis B. Finally, the expression $D = \frac{L-B}{L+B}$ provides the deformation parameter, and the expression $\theta = \arctan\left(\frac{z_A - z_O}{x_A - x_O}\right)$ calculates the orientation angle.

This purely geometrical approach is subjected to errors due to the amount of points *Tecplot* produces. In some cases two points may give the same longest distance, which deviates from the actual longest distance, and therefore we have two coordinates for point A (x_A, z_A); the same could occur for point B (x_B, z_B). For example, figure (2.6) shows the points extracted for droplets in confinement ratios $2R/H = 0.4, 0.6$ and 0.7, in the area 0 to 90° of figure (2.5). In the area highlighted in the black rectangular, notice the points connected to the centre with solid lines. These lines represent the orientation of each droplet. Specifically, for $2R/H = 0.7$ (magenta lines) dashed lines depict an alternative orientation for this droplet. Both solid and dashed lines have the same length. The algorithm, developed in Fortran and given in *Appendix* D, systematically considers the point with the highest $z-$ coordinate as the one which points to the droplet tip point.

This feature does not produce significant differences to the deformation parameter values. However, the orientation angle is affected and the solid-calculated and dashed-alternative values may deviate by almost 3.5°. This leads to a significant noise in the plots of orientation angle against the confinement ratio $(\theta - 2R/H)$, and less important in the orienation angle against capillary number plots $(\theta - Ca)$, see later figures in *Chapters* 3 and 4.
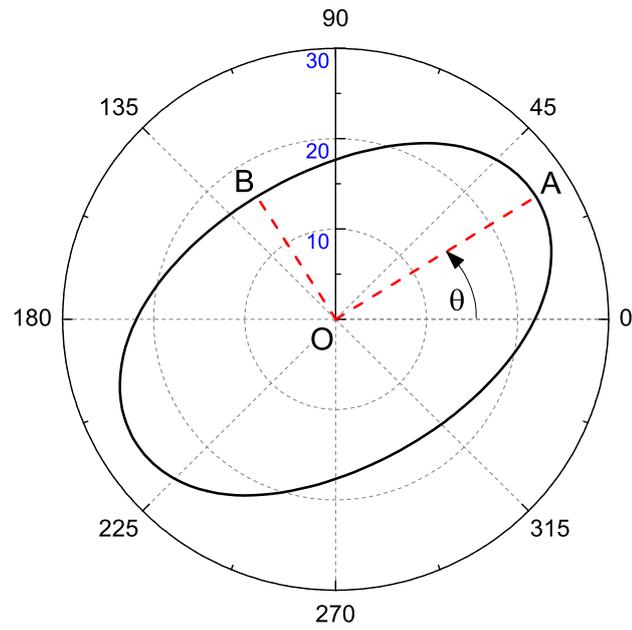
Figure 2.4: Polar graph of the Newtonian droplet shape in the $x - z$ middle plane, for $Re = 0.1$, $Ca = 0.2$, $\lambda = 1$, $2R/H = 0.4$, stated as the 'standard' case.
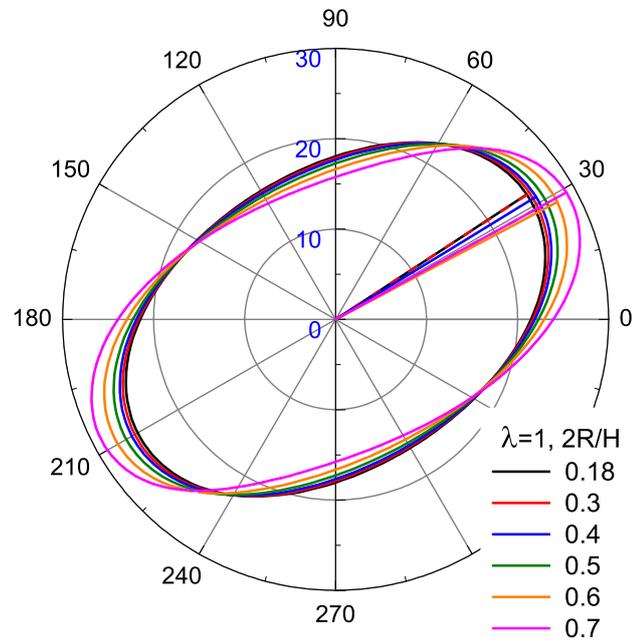
Figure 2.5: Polar graph of the Newtonian droplets shapes of $\lambda = 1$ in various $2R/H$, in the $x - z$ middle plane for $Re = 0.1$, $Ca = 0.2$.
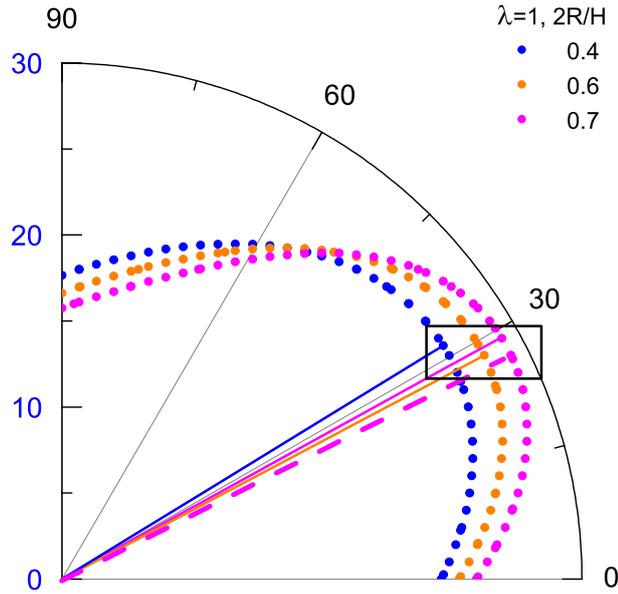
Figure 2.6: Enlarged image of figure (2.5) in the area of 0 to 90° for $2R/H = 0.4$, 0.6 and 0.7.

2.4.6   Stresses

The deformation and orientation of the droplet are closely related to the deviatoric stresses exerted on its surface. Their evaluation provides a deeper understanding of the droplet behaviour. Again, the calculations consider local properties at a specific time in the $x - z$ middle plane. The strain rate is calculated *in the post-processing* procedure using *Tecplot* and applying equation (2.5) and then equation (2.3).

Figure (2.7) illustrates the normal-x (T_{xx}), the normal-z (T_{zz}) and the shear stress (T_{xz}) components with the contours in *l.u.* in *Tecplot*. The droplet refers to the 'standard' case and its surface is shown with the black line. From these plots one can only estimate the magnitudes of the stresses on the interface. Furthermore, the impact of the different stresses cannot be contrasted. Additionally, a considerable large amount of figures (and space) would be needed to draw conclusions on the effects of different stresses on different droplets.

To avoid these drawbacks, the three stresses are replotted in figure (2.8) for the 'standard' case droplet in the same graph, with the help the graphics software *Origin*. This graph is similar to the polar one shown in figure (2.4) where the radial axes are

replaced by the ellipsoidal ones depicting the magnitude of the stresses. The angular axes are identical to those shown in figure (2.4) and the dashed thick black line shows the orientation (θ) of the droplet corresponding to the line OA. The solid black ellipsoidal is a reference to the original droplet shape, but here it shows the locations where the stresses become zero.

Hence, the graph in figure (2.8) reads the magnitude and the angular position a stress is exerted on the surface. The values along the ellipsoids are in $l.u.$ in the order of -6. Green, blue and red thick lines depict the stresses T_{xx}, T_{zz} and T_{xz}, respectively. An alternative representation to evaluate the stress components on a droplet, "*figure 8*" in reference [55] plots the shear rates against the height of the domain at a fixed x-coordinate where the tip of the droplet lies.

Additionally, the stresses projected to the unit normal to the interface vector $\vec{n} = -\frac{\nabla \rho^N}{|\nabla \rho^N|}$ are considered by calculating the dot product:

$$\vec{T} = \vec{n} \cdot \mathbf{T} \tag{2.51}$$

When these vectors are plotted on the surface of a droplet, an image as shown in figure (2.9) is produced. The solid black line linking the centre to the tip of the droplet shows the orientation angle of the droplet, which calculation is described in the previous Section 2.4.5. The two most important stress vectors are schematically reproduced on the right-hand side of figure (1.1), representing the 'elongation' and 'compression' stresses on an ellipsoidal droplet.

Finally, the deformation and orientation of the droplet are closely related to the velocity and pressure features of the flow in the matrix fluid, which are described in the following Section 2.5.
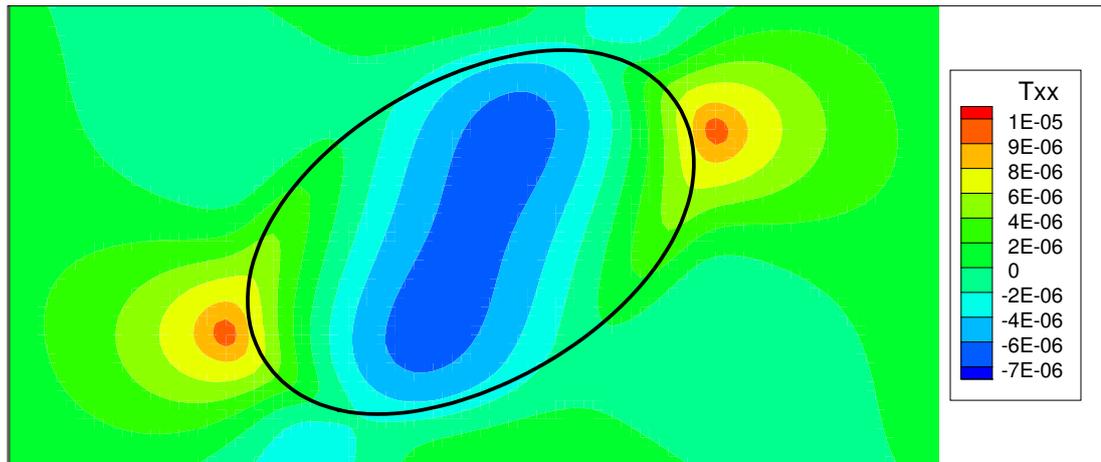
(a)
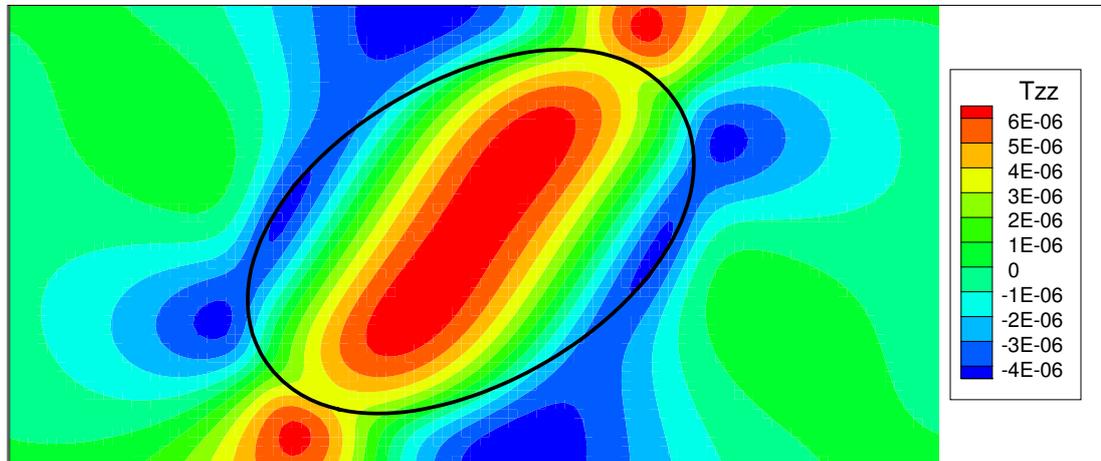
(b)
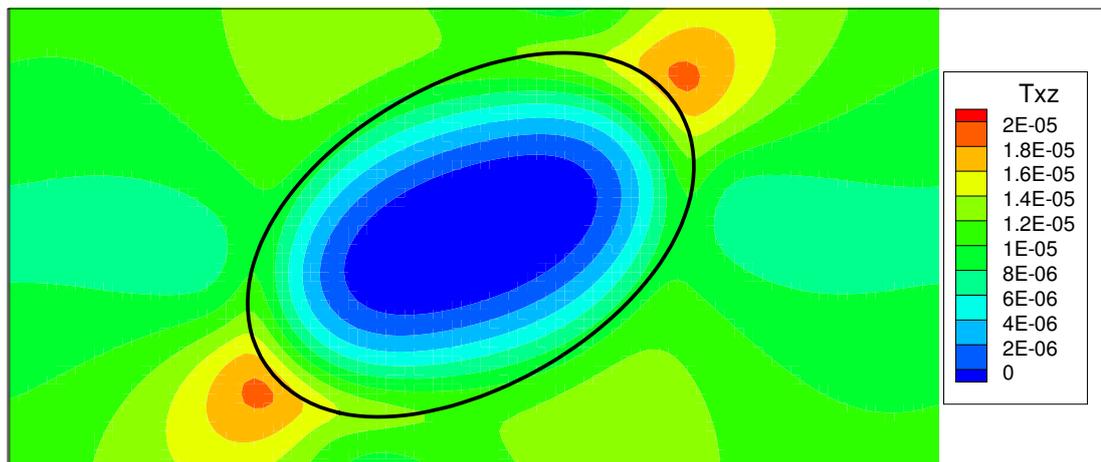
(c)

Figure 2.7: Shape of a Newtonian droplet (black lines) and stresses contours in the domain at the $x - z$ middle plane: (a) T_{xx}, (b) T_{zz} and (c) T_{xz}, for the case $Re = 0.1$, $Ca = 0.2$, $2R/H = 0.4$, $\lambda = 1$, stated as the 'standard' case. Legend in lattice units.
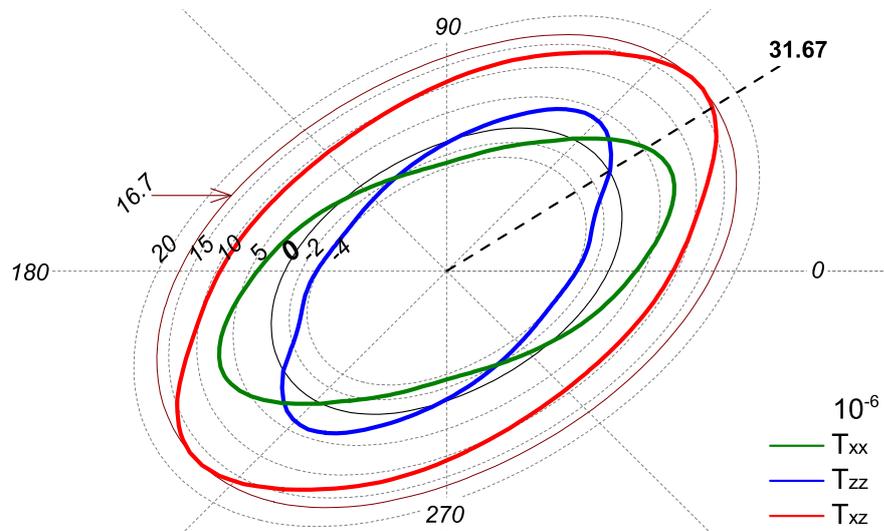
Figure 2.8: Graph of the stress components on the surface of Newtonian droplet, for $Re = 0.1$, $CA = 0.2$, $\lambda = 1$, $2R/H = 0.4$, stated as the 'standard' case.
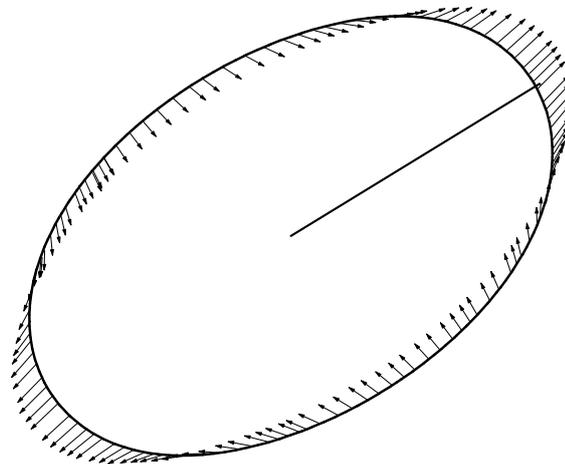
Figure 2.9: Graph of the stress vectors on the surface of Newtonian droplet, for $Re = 0.1$, $CA = 0.2$, $\lambda = 1$, $2R/H = 0.4$, stated as the 'standard' case.

2.5   Evolution of the Flowfield

This section describes briefly the transient evolution of the system in shear to provide a first insight on the evolution of the flow.

In the beginning, continuous and dispersed phases are quiescent. A sudden onset of the walls movement towards opposite directions imposes the shearing. The carrier fluid parcels at the proximity of the walls move along. With increasing simulation time (t), they drag neighbouring fluid parcels residing in the interior of the domain until all fluid parcels are involved in this procedure. At an early *time instant* comparing to the shearing *duration*, the droplet fluid parcels also experience the imposed shear. Consequently, the droplet evolves and according to its final state the flow is characterised by two regimes: the steady state and the breakup, as described in *Chapter* 1.

The motion of the walls generates a pressure field as the matrix fluid flows past the droplet. Figure (2.10) illustrates the flow on the surface of the droplet and in the matrix fluid in the middle $x - z$ plane at the steady state. Pressure magnitudes are showed with the contours, i.e. green-to-blue colours represent large-to-low values, and the velocity trajectories are showed with the black lines and arrows. The red thick line shows the surface of the droplet in the middle plane. Notice here the pressure difference, which is high at the flattened area of the droplet (point **B**) and low at the area close to the tip of the droplet (point **A**). This pressure difference is linked to the degree of the final tilting of the droplet, and is a key aspect when considering the orientation angles among different droplets, as later discussed in *Chapter* 3.

The observation of the low pressure at the area close to the tips may be related to the work on droplet deformation and breakup at *high Reynolds* numbers reported in [54, 55]. In these works, the highest values of velocity are observed at the tips of the droplet. By connecting the velocity to the pressure through the Bernoulli principle, which is considered valid at high Re values, the authors claim that relatively lower pressure areas are indicated at the tips of the droplet compared to the pressure in different sites of the domain. This lower pressure at the tips results to a suction at these regions which is related to the further tilting of the already elongated droplet and the induced breakup behaviour.

Figure (2.11) illustrates the same image as figure (2.10), but the contours depict the velocity instead of the pressure magnitudes. Again, green-to-blue colours represent large-to-low values. More view points of the flow on the surface are illustrated in *Appendix A* in which the streamlines resemble qualitatively the pathlines in the experimental observations [154].

Evidently, the droplet has obtained an ellipsoid shape and its fluid circulates on the surface. Notice that, at the same time the matrix fluid flows above and below the droplet towards opposite directions. However, part of the matrix fluid circulates around the drop shown by the closed streamlines around the drop. Additionally, the streamlines present variations in the velocity magnitude downstream; the velocity is greater at the top (and bottom sides) of the droplet (point **B**) and lower at the 'edges' of the recirculation located at about the middle height of the domain ($z \approx NZ/2$), noted with the red circle in figure (2.11).
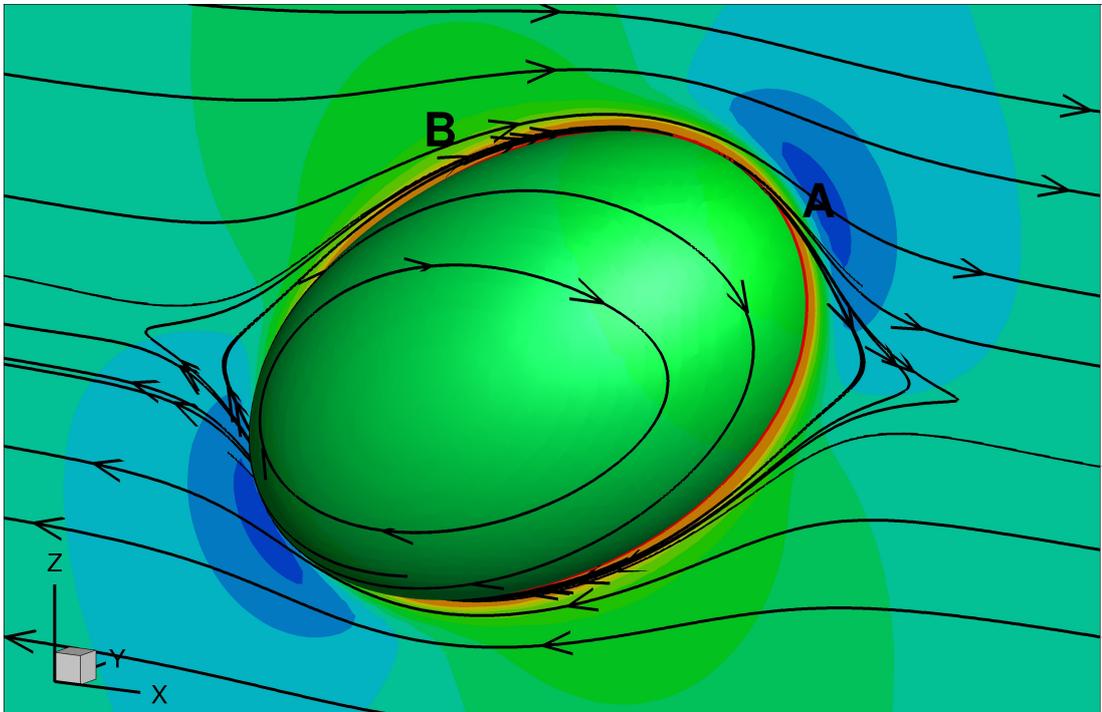
Figure 2.10: Flowfield of the matrix fluid in the $x - z$ middle plane, and on the surface of the droplet. Contours represent the pressure with green for larger and blue for lower values.
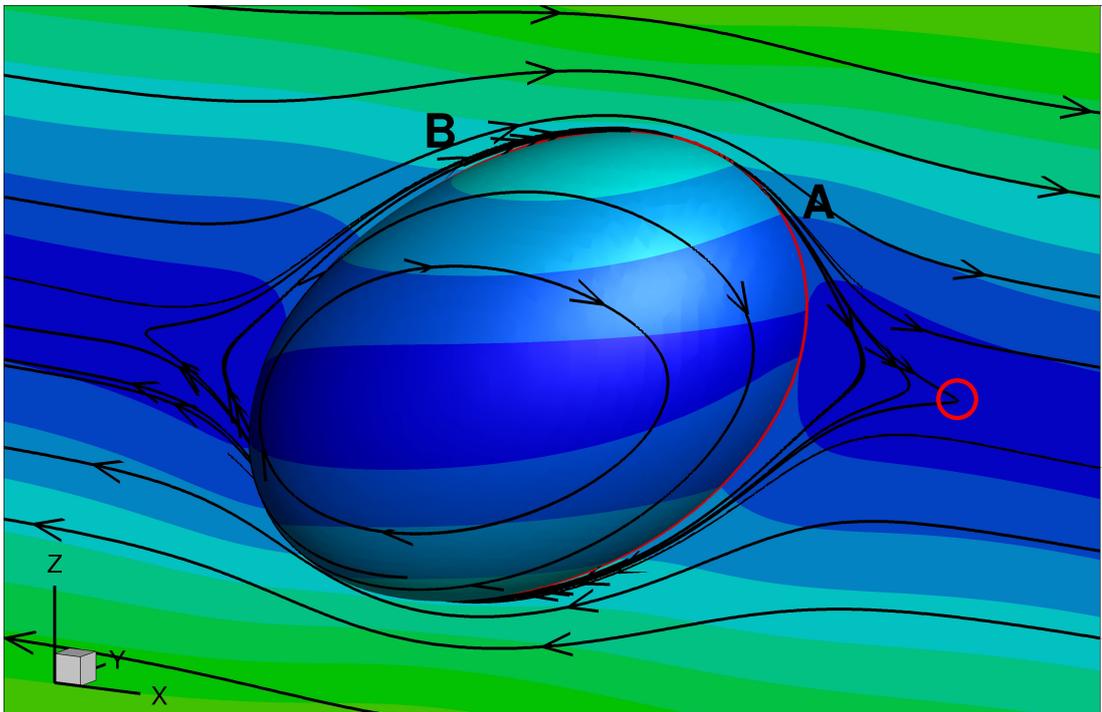
Figure 2.11: Flowfield of the matrix fluid in the $x - z$ middle plane, and on the surface of the droplet. Contours represent the velcoity magnitude with green for larger and blue for lower values.

Chapter 3

Newtonian Droplets in Shear

3.1 Introduction

The previous *Chapter* specifies the numerical method, computational setup and data acquiring methods. This *Chapter* discusses the simulations results in three parts. The first two parts describe the behaviour of a confined Newtonian droplet in the steady state regime with plots of the deformation and the orientation angle. The carrier fluid is Newtonian in Section 3.2.1, and changes to a power-law fluid in Section 3.2.2. Velocity fields images and evaluation of stresses on the surface explain the observed behaviour. In the third section, the critical capillary number Ca_{cr} is investigated in a range of confinement ratios. The final section summarises the findings and conclusions.

3.2 Droplet Deformation

3.2.1 Newtonian Matrix Fluid

Initially, droplet deformation simulations in the confinement ratio of $2R/H = 0.18$ are performed to test the numerical method in weakly bounded shear flows. The capillary number, Ca, varies from 0.1 to 0.3 and the viscosity ratio, λ, is 1, i.e. the droplet and the carrier fluids have the same viscosity. Hereafter this droplet is called equi-viscous. When $\lambda < 1$, the droplet has a lower viscosity than the matrix fluid and is referred to as a low-viscous droplet. When $\lambda > 1$, the respective droplet is called high-viscous.

Figure (3.1(a)) plots the equi-viscous droplet deformation parameter as a function

of the capillary number. Our numerical results are compared with the predictions from the Taylor theory and the MMSH model, alternative numerical results obtained by the BIM [35, 49] and the VOF method [52], as well as experimental data in [20, 31]. The degree of confinement does not match for all cases. Furthermore, *the confinement* is not available for data reported in [35, 49] where the flow is considered being unbounded. Good agreement is observed among the data depicted. Not only does this agreement validate our numerical method but also suggests a negligible influence of the walls for low confinement ratios such as the present one. This observation is consistent with the previous numerical studies [37] (see therein the matching results for $2R/H = 0$, 0.25, in figures(8) and (9) for $\lambda = 1$), [39] (see therein the matching results for $2R/H = 0$, 0.1, 0.25, in figure (6) for $\lambda = 0.1$, and figure (7) for $\lambda = 10$), and the experimental observations, i.e. Taylor [26] performed experiments in 2R/H=0.2 and validated his theoretical predictions where no wall effects are included, and [20] (see therein the results for $2R/H \gtrapprox 0.2$, in figure (10) for $\lambda = 0.3$, and figure (11) for $\lambda = 5.2$).

Additionally, figure (3.1(b)) compares the orientation angles of the deformed droplet (θ) from our simulations to those reported in [35, 38, 49, 52]. There is a fairly good agreement between our results and those obtained in [38], *at a matched confinement ratio* $2R/H = 0.18$, both by the experiments and the BIM.

Further more, *keeping other parameters the same*, the tests in confinements $2R/H = 0.5$ and 0.69 are conducted. Figure (3.2) shows the comparison among the deformation parameter obtained with the present method, the Taylor theory and the MMSH model predictions, and the experimental results in [31] and [20]. Our simulation results agree quite well with the predictions from the MMSH model and the experimental data, verifying that the present LBM modelling can successfully predict the deformation of a relatively highly confined droplet. Moreover, *consistent with the previous findings*, the MMSH model can provide experimentally-matched predictions of the droplet deformation. Notably, predictions from the Taylor theory are no longer accurate for high confinement ratios.

At this point, a remark on our results is necessary. The shape of the droplet, i.e. to which degree it resembles an ellipse, affects the accuracy of our calculations. Figure (3.3) shows the final shape of the deformed droplet in the $x-z$ middle plane for capillary
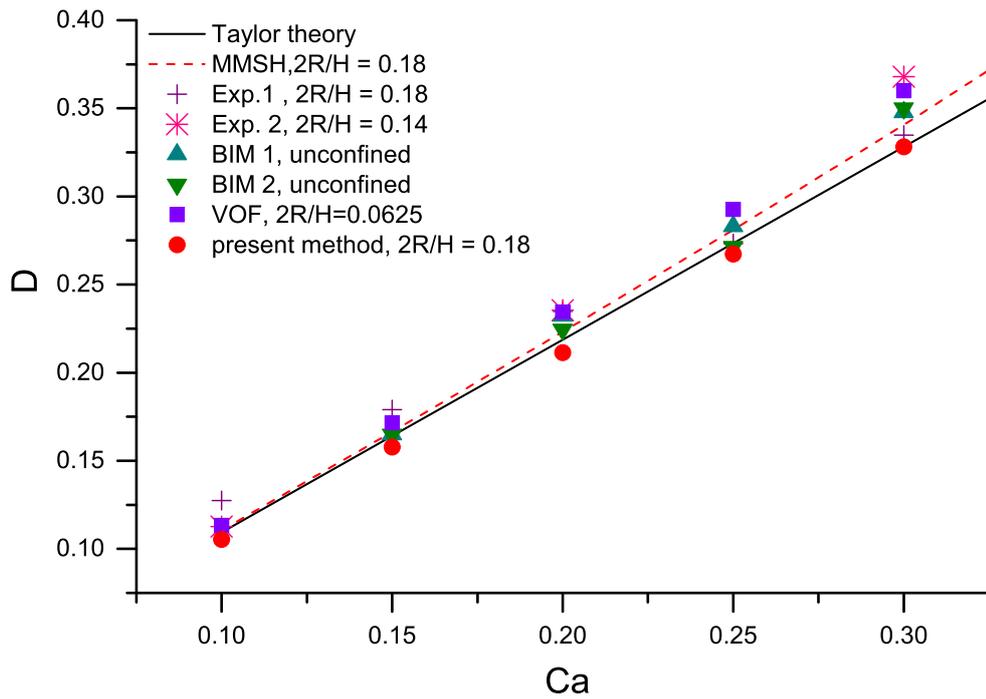
(a)
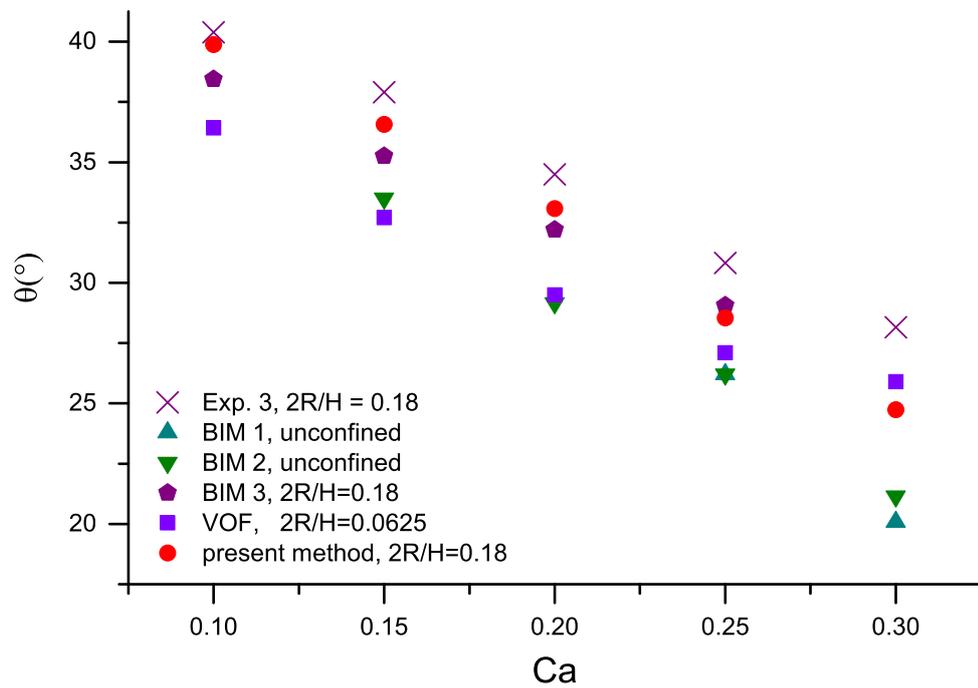
(b)

Figure 3.1: (a) Deformation parameter, and (b) orientation angle as a function of the capillary number, Ca, for $\lambda = 1$, in weakly confined or unconfined domains. Exp.1: [20], Exp.2: [31], BIM 1: [35], BIM 2 [49], BIM 3: [38], VOF: [52], Exp. 3 and BIM 3: [38].

numbers $Ca = 0.2$, 0.25 and 0.3 in confinement $2R/H = 0.69$. The contours display the colour function for values $\rho^N = -0.5$, 0, and 0.5. It is clear that the droplet deviates from the ellipsoidal shape *to some extent* at high capillary numbers, e.g. $Ca = 0.25$ and 0.3. This deviation leads to a difficulty in determining the accurate value of the deformation parameter and the orientation angle. To avoid high deviation from the ellipsoidal droplet, the confinement ratio and the capillary number are restricted to $2R/H \leq 0.7$ and $Ca \leq 0.3$ in the rest of the simulations.

The effect of confinement is investigated in three viscosity ratios: $\lambda = 0.3$, 1 and 3. Figure (3.4) plots our results as a function of the capillary number in four confinement ratios: $2R/H = 0.18$, 0.4, 0.5 and 0.7. On the left-hand side, the deformation parameter is compared to the Taylor theory and MMSH model predictions. For viscosity ratio $\lambda = 0.3$, our LBM results agree well with the MMSH model predictions at low capillary numbers, e.g. $Ca \leq 0.2$, and low confinements. With increasing Ca the numerical results underestimate the predictions. The deviation also increases with rising confinement with the greatest being 20% at $Ca = 0.3$ in $2R/H = 0.7$. The reason for this deviation remains an open question and needs further study. Similar observations are reported in [20] between the experimental data and the prediction of the phenomenological model.
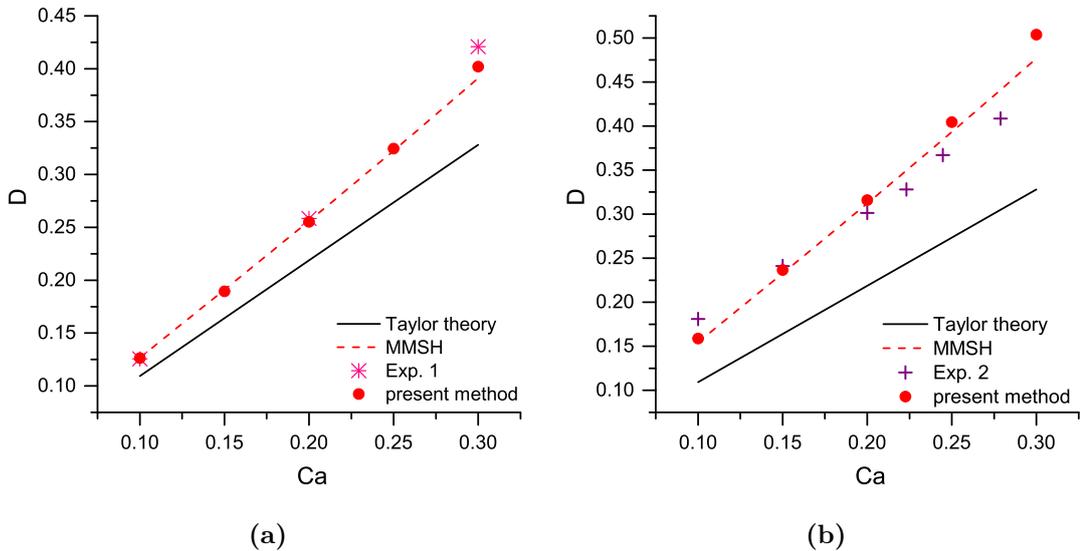
Figure 3.2: Deformation parameter as a function of the capillary number, Ca, for $\lambda = 1$, in confinements (a) $2R/H = 0.5$ and (b) $2R/H = 0.69$. Exp. 1: [31], Exp. 2: [20].
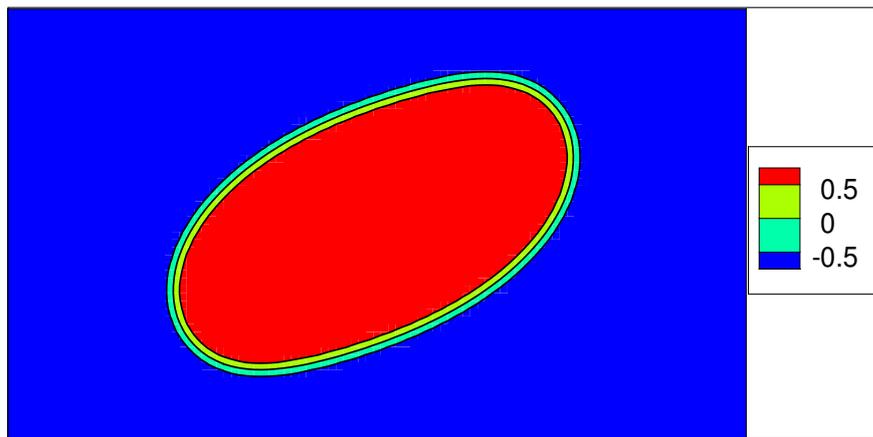
(a) $Ca = 0.2$
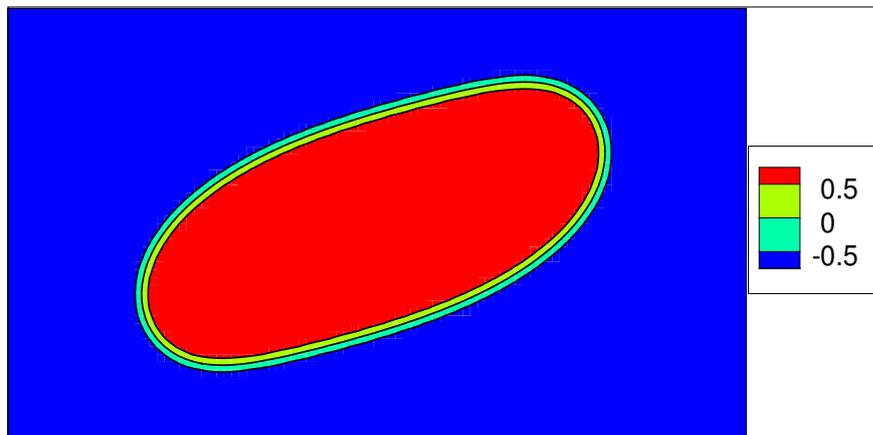
(b) $Ca = 0.25$
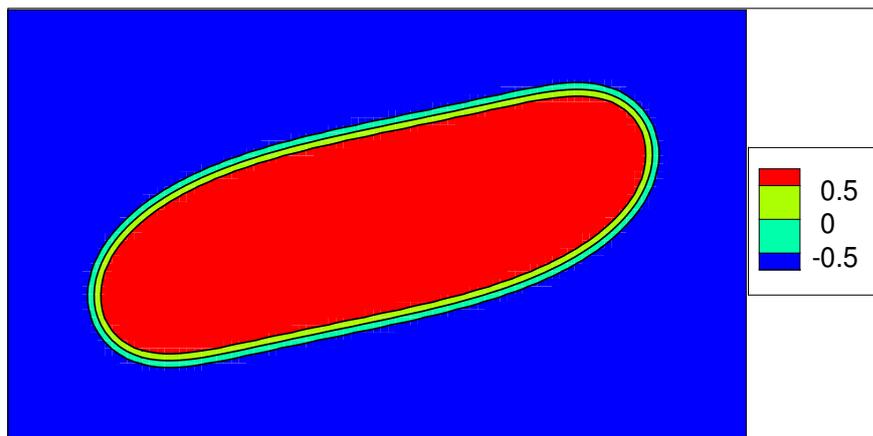
(c) $Ca = 0.3$

Figure 3.3: Shape of the final deformed droplet, in the $x - z$ middle plane for $\lambda = 1$ and $2R/H = 0.69$, at capillary numbers $Ca = 0.2, 0.25, 0.3$. The contours show the colour index function.

For viscosity ratios $\lambda = 1$ and 3, the deformation parameter is calculated slightly above or below the predictions from the MMSH model. Nevertheless, they show quite good agreement. The highest divergences appear in confinement $2R/H = 0.7$ due to the non-ellipsoidal shape of a tightly suspended droplet under strong shear.

More specifically, the simulations show that the deformation of the low-viscous droplet is the least affected by wall confinement. On the other hand, the deformation of the *high-viscous* droplet is most affected, as shown by the difference in the deformation increment trend with increasing Ca, observed in figure (B.1) in *Appendix* B. Additionally, this figure illustrates that among the three viscosity ratios the *high-viscous* droplet presents the smallest deformation in low confinements, $2R/H \leq 0.5$, with exceptions at capillary numbers 0.1 and 0.15. However, in $2R/H = 0.7$ the high-viscous droplet deforms more than the low-viscous one, and even more than the equi-viscous at $Ca \leq 0.2$.

As far as the Taylor theory is concerned, its predictions show a remarkable agreement for viscosity ratios $\lambda = 0.3$ and 1 in the lowest confinement ratio $2R/H = 0.18$. As expected, and commented earlier, it cannot predict the deformation in higher confinements, and it also fails to estimate the deformation of a high-viscous droplet. Therefore, it can be concluded that the Taylor theory is not well suited to describe the droplet deformation for $2R/H \geq 0.4$, or even smaller for high-viscous high-capillary cases (figure (3.4) bottom left).

Figure (3.4) on the right-hand side shows the orientation angles against the capillary number as calculated in our simulations. Increasing capillary numbers result in decreasing orientation angles. This reflects the fact that droplets become more oriented to the direction of the flow in stronger shears. The increasing wall confinement produces the same effect although clearly less pronounced. Additionally, among the three droplets studied the low-viscous turn less to the direction of the flow. On the other hand, the high-viscous droplet (of viscosity ratio $\lambda = 3$) turns the most. This behaviour is easily observed in figure (B.2) in *Appendix* B, and will be further examined.

The *effect of the walls* is further investigated on different viscosity droplets in varying confinements, from $2R/H = 0.18$ to 0.7, at a fixed capillary number $Ca = 0.2$.

Figure (3.5(a)) shows the variation of the deformation parameter for viscosity ratios
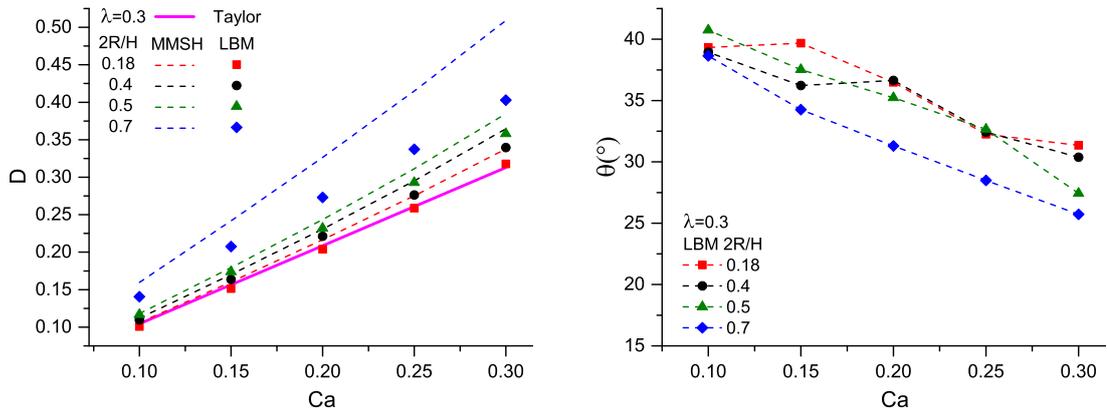
(a) $\lambda = 0.3$
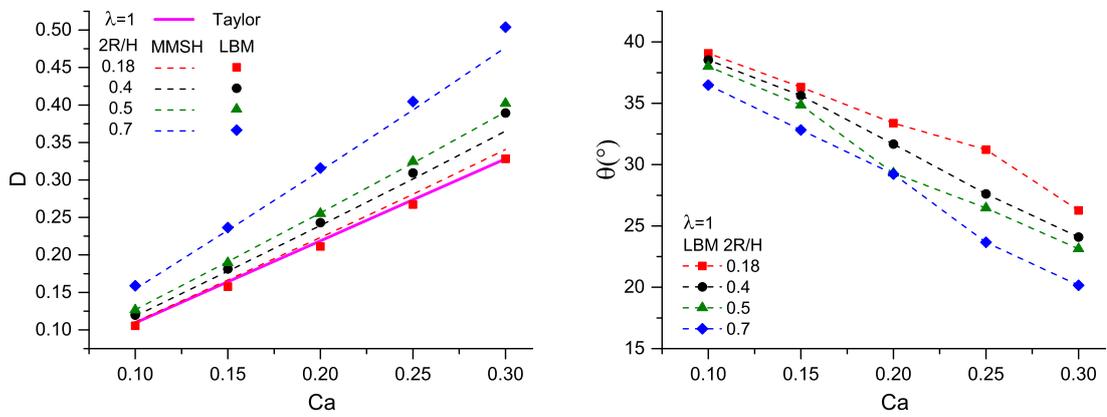
(b) $\lambda = 1$
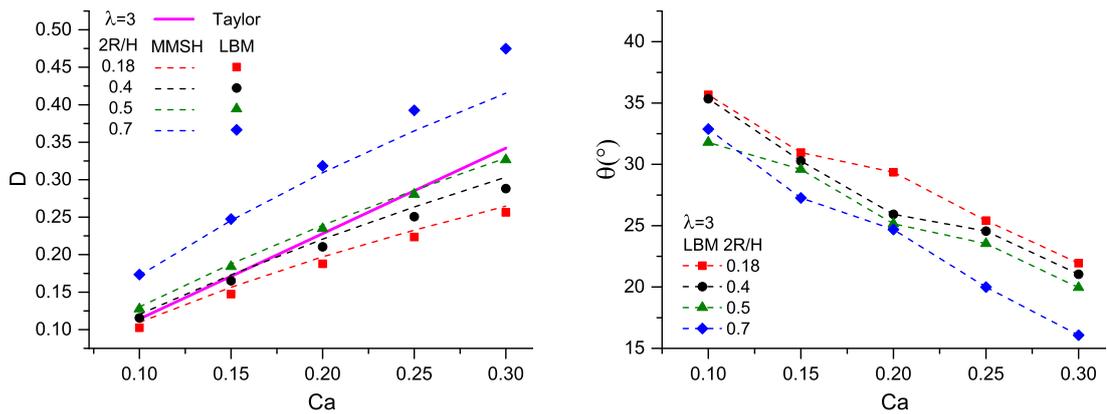
(c) $\lambda = 3$

Figure 3.4: (Left) Deformation parameter, and (right) orientation angle as a function of the capillary number, Ca, in various confinements, for viscosity ratios $\lambda = 0.3$, 1, 3.

$\lambda = 0.3$, 0.5, 1, 3, and 5 as a function of the confinement $2R/H$. Notably, the equi-viscous droplet presents the highest values. The deformation of low-viscous droplets (red lines) increases as the viscosity ratio increases, from $\lambda = 0.3$ to 0.5. On the contrary, the deformation of high-viscous droplets (blue lines) decreases as the viscosity ratio increases, from $\lambda = 3$ to 5. Interestingly, the deformation does not present a linear correlation with the proximity of the walls. It increases almost linearly, with different rates for each viscosity ratio λ, before and after the confinement ratio $2R/H = 0.4$. Up to this value, the deformation exhibits a slow growth rate which increases upon higher values. Hence the *walls effect* becomes more significant at confinement ratios above 0.4. Especially, high-viscous droplets of $\lambda > 1$ show more significant variations. This feature suggests that the wall proximity has a stronger effect on the deformation of more viscous droplets, also reported in [35]. The orientation behaviour along with the exerted stresses on the droplet can justify this deformation feature.

The corresponding orientation angles (θ) are shown in figure (3.5(b)). More viscous droplets align to a greater extent to the direction of the shear flow. In addition, the proximity of the walls promotes the alignment of every droplet. Hence, higher viscosity and confinement ratios lead to smaller orientation angles. Evidently, the decline rate of orientation angle values θ for low-viscous droplet is higher comparing to the high-viscous one.

Inset (i) in figure (3.5) contrasts the droplets shapes in confinement $2R/H = 0.7$ for $\lambda = 1$ and 3. The deformation differs by 2% and the orientation angle changes slightly more than 4 degrees. However, these differences lead to an insignificant deviation between the droplets shapes, especially noteworthy the fact of 4 degrees in highly deviated shapes. The close proximity of the walls leads two droplets of completely different viscosity, $\lambda = 0.3$ and 5 seen in inset (ii), to turn to different directions; their orientation angles differ by 9 degrees. Nevertheless, they deform to the same extent. These findings show the complexity of interplay among shear intensity, viscosity ratio and wall proximity.

The pressure and the flow in the matrix fluid strongly affects the droplet behaviour. Figures (3.6) and (3.7) illustrate the pressure and the velocity fields inside and around the droplet at the $x - z$ middle plane, respectively. The thick red lines represent the

(a)

(b)
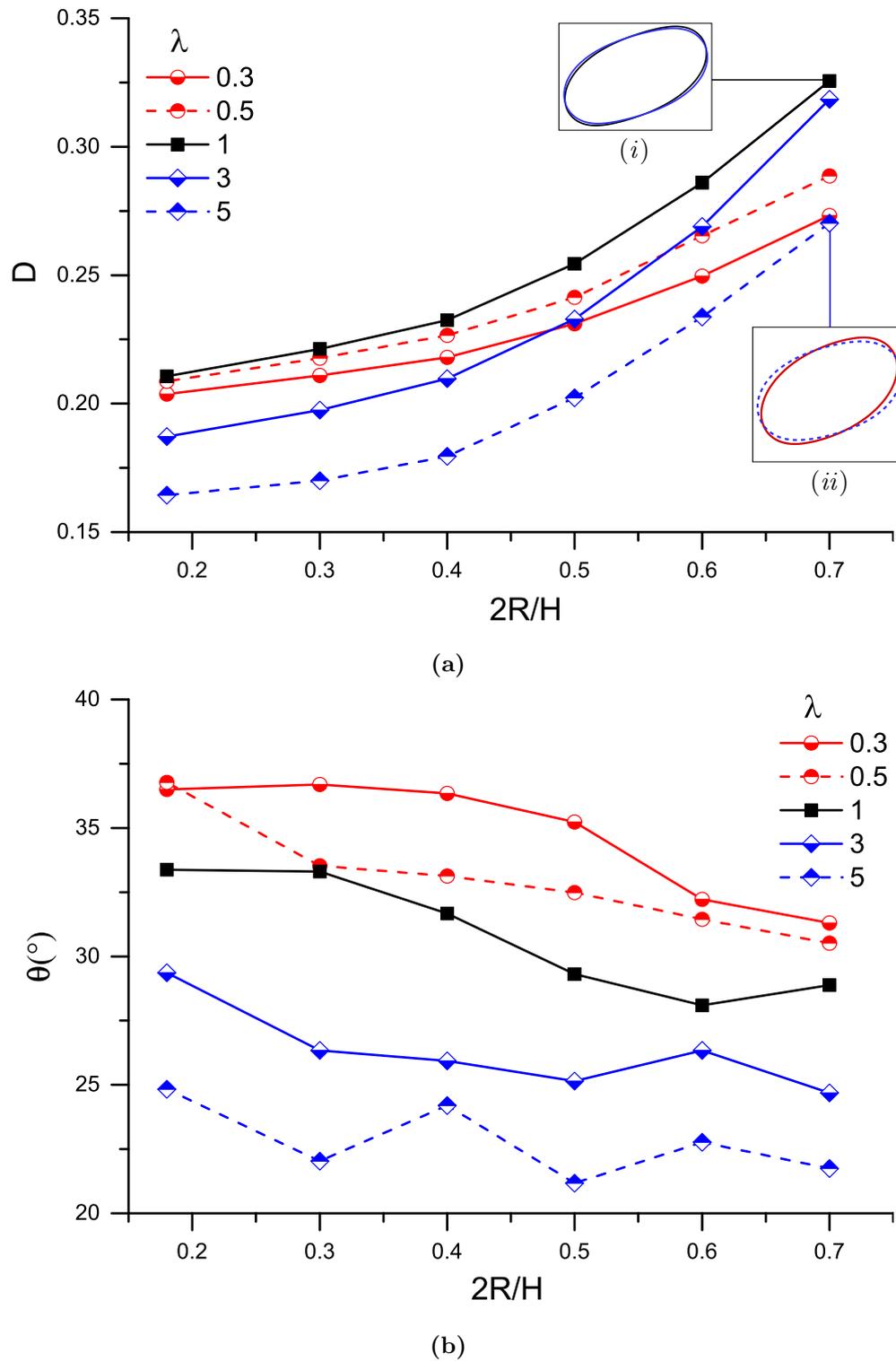
Figure 3.5: (a) Deformation parameter, and (b) orientation angle as a function of the confinement ratio, $2R/H$, for various viscosity ratios, λ, at $Ca = 0.2$. Inset (i) shape comparison of the final deformed droplets for $\lambda = 1$ (black) and 3 (blue), inset (ii) shape comparison of the final deformed droplets for $\lambda = 0.3$ (red) and 5 (dashed blue), in confinement $2R/H = 0.7$

droplet surface and the black lines show the streamlines with arrows pointing to the direction of the local flow. Contours display the pressure and the velocity magnitudes: red for maximum and blue for minimum values, which are the same in all images to allow for comparisons among different cases. From top to bottom, the viscosity ratio, λ, varies at values of 0.3, 1, 3, 5. Since the wall approximation effect becomes more significant at confinement ratios larger than $2R/H = 0.4$, we limit this investigation to $2R/H = 0.4$ (left) and 0.7 (right).

Clearly, viscosity and confinement ratios affect not only the droplet shape and orientation angle, but also the pressure and velocity field patterns. The following analysis considers the right half of the images in figures (3.6) and (3.7). Due to symmetry, the same findings are valid for the left part but in the opposite directions.

In the earlier Section 2.5, it is discussed the locations of the areas where the highest and lowest pressure are presented. Here, the difference between these pressures is shown qualitatively. For higher viscosity ratios the difference between the pressure is greater. This correlates with the tumbling to a greater extend (lower θ values) of higher viscosity droplets. With respect to the wall effects, the pressure difference is more pronounced in high confinements leading also to lower orientation angles.

The relative position of the *high* and *low-velocity* points along the longest recirculating streamline plays also an important role, as it is related to the amount of the recirculated matrix fluid around the droplet, and thus the interplay between the droplet and the suspending fluid.

For both confinement ratios $2R/H = 0.4$ and 0.7 the *low-velocity* point resides at a greater distance in the $x-$ direction from the droplet surface for more viscous droplets, indicating the stronger impact of high-viscous droplet with the flow of the matrix fluid. This is less pronounced in the highly confined system, where the droplet shows greater tumbling, i.e. smaller orientation angle.

The confinement ratio increment from 0.4 to 0.7 has two effects. First, the *low-velocity* location shifts closer to the droplet surface and deviates from the centreline. Notably, this deviation becomes greater *for lower viscosity ratios.* Secondly, the magnitude of the velocity at the top of the droplet increases for the confinement ratio $2R/H = 0.7$. This velocity is greater for low-viscous droplets; an indication that *low-*

viscous droplets interfere insignificantly with the flow of the matrix fluid.

The interior streamline pattern in a droplet of $\lambda = 0.3$ presents a double vortex structure, where a single vortex structure is visible in an equi- or high-viscous droplet. Interestingly, an analogous variation in the streamline pattern is shown in numerical studies on inertial effects [52, 54, 81, 82] where the Reynolds number has a relatively high value. The inclination angle of the internal vortices (streamlines) and the orientation angle of a droplet both decrease, and their difference also reduces, for higher viscosity ratio systems. For two different confinement ratios, the streamline patterns are qualitatively similar but quantitatively different, e.g. the inclination of stream-lines inside the droplet is smaller at the confinement ratio of 0.7. This observation corresponds to a smaller orientation angle and larger deformation of the droplet.

Further on, the deformation of the droplet and its connection to the stresses exerted on the droplet surface are investigated. Figure (3.8) shows the stress components for three viscosity ratios $\lambda = 0.3, 1, 3$. Three characteristic confinement ratios are considered for weak, moderate and high confinement, i.e. $2R/H = 0.18, 0.4, 0.7$. With increasing confinement the carrier fluid has a narrower passage to flow past the droplet; this fact leads to built-up stresses on the droplet surface.

As the walls approach from a confinement ratio $2R/H = 0.4$ to 0.7 the droplet of viscosity ratio $\lambda = 0.3$ turns to the direction of the flow by 5 degrees, considerably more than the tumbling of more viscous droplets. The tumbling assists the flow past the droplet. Hence, the increase of the maximum shear stress component rises by about 23 %. On the contrary, for viscosity ratio $\lambda = 3$ the orientation angle reduces by 1 degree in average with increasing confinement. The maximum magnitude of shear stress component increases by almost 50 %. Consequently, the deformation increasing rate grows slightly for $\lambda = 0.3$ and rapidly for $\lambda = 3$. Droplets for $\lambda = 0.5$ and 5 show similar features to $\lambda = 0.3$ and 3, respectively. The behaviour of the equi-viscous droplet shows intermediate characteristics, regarding its orientation and deformation deviations.

Figure (3.9) shows the stress vectors on the droplets and the orientation angle for three viscosity ratios for $2R/H = 0.4$, on the left-hand side with black colour, and $2R/H = 0.7$ on the right-hand side with red colour. Additionally, table (3.1) presents

(a) $\lambda = 0.3$

(b) $\lambda = 1$

(c) $\lambda = 3$

(d) $\lambda = 5$
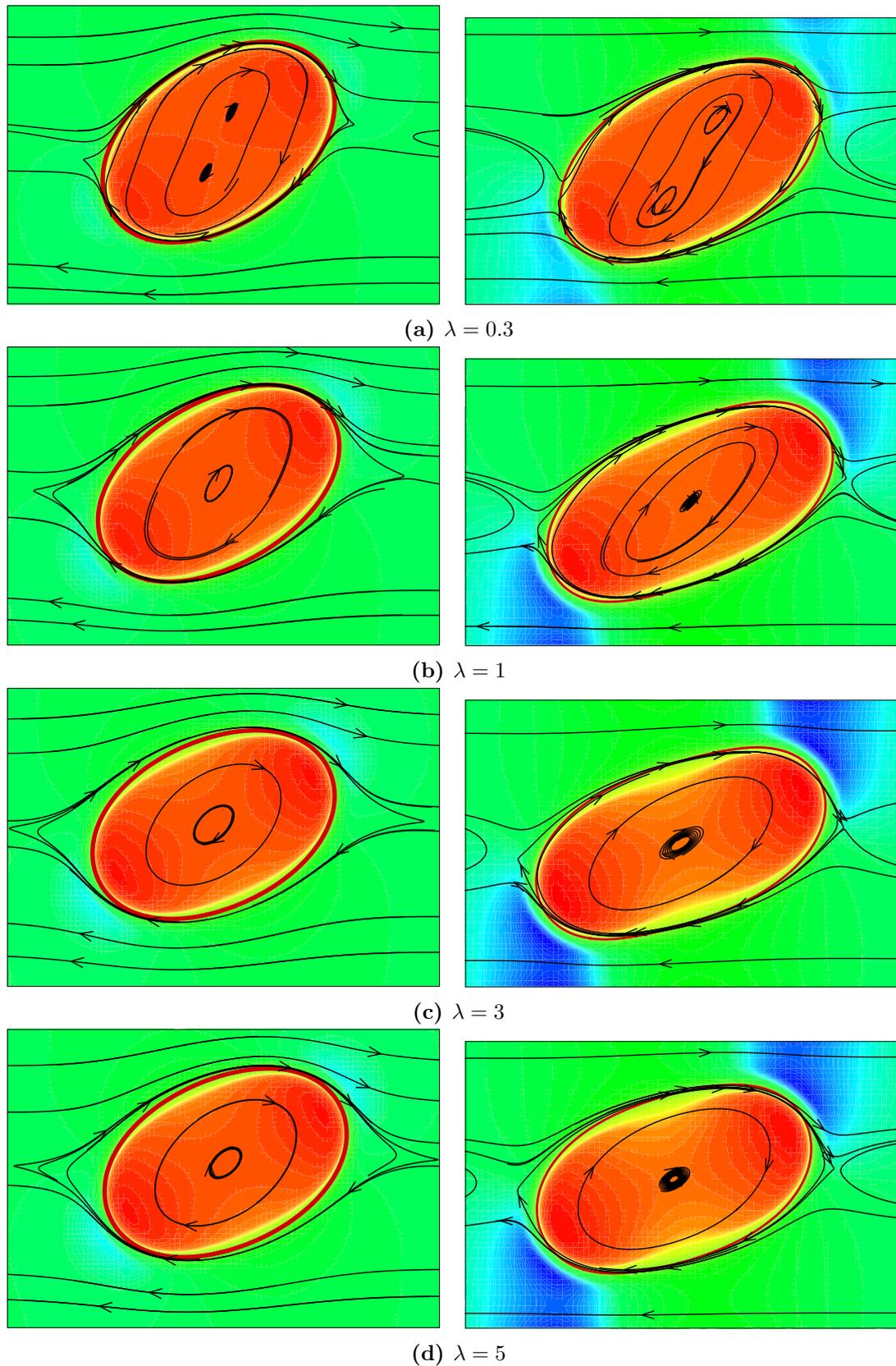
Figure 3.6: Flowfields in confinement ratios (left) $2R/H = 0.4$, and (right) $2R/H = 0.7$, in the $x - z$ middle plane at $Ca = 0.2$, for various viscosity ratios λ. Circles depict the low-velocity – high-pressure point.

71

(a) $\lambda = 0.3$

(b) $\lambda = 1$

(c) $\lambda = 3$

(d) $\lambda = 5$
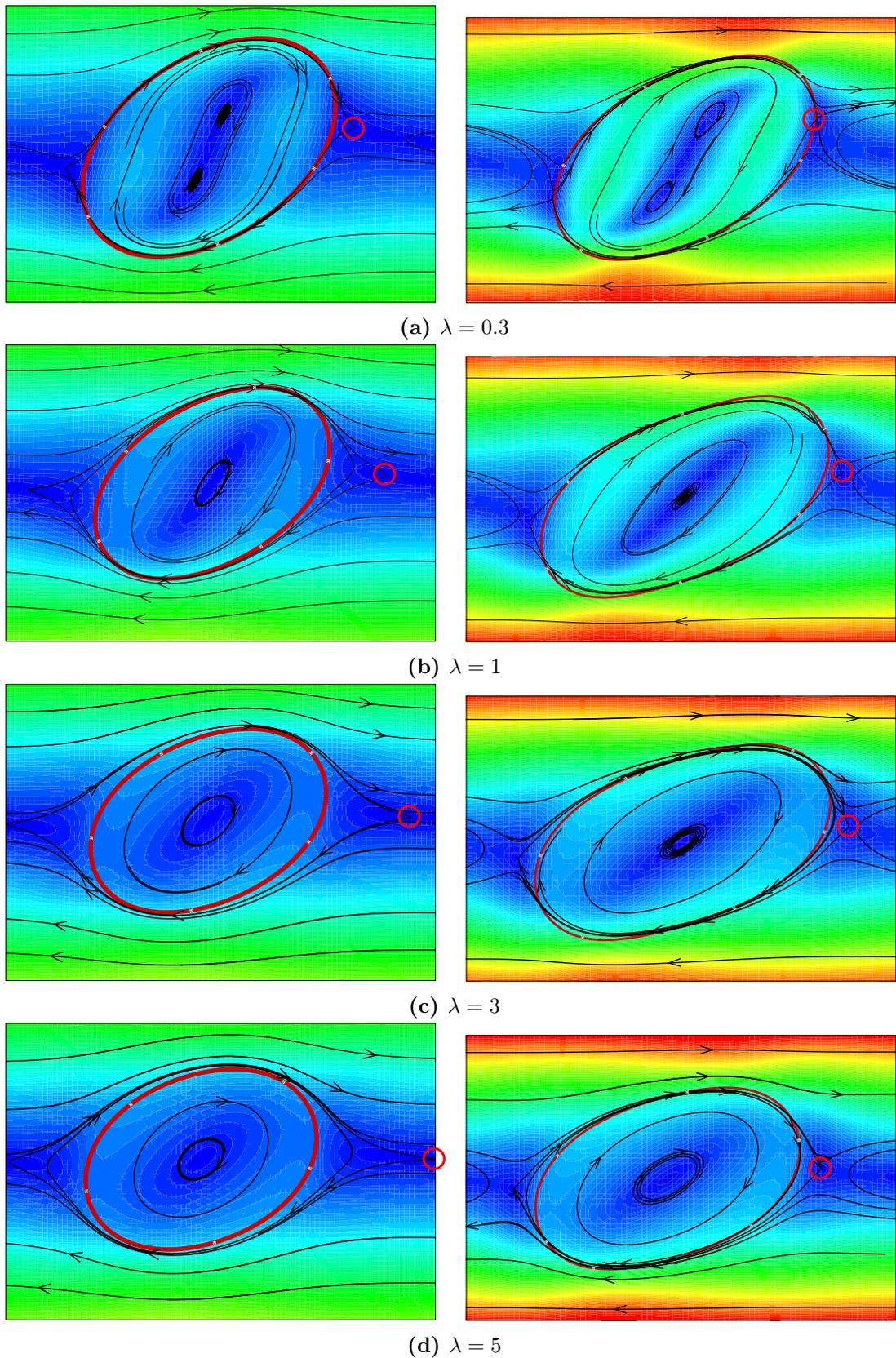
Figure 3.7: Flowfields in confinement ratios (left) $2R/H = 0.4$, and (right) $2R/H = 0.7$, in the $x - z$ middle plane at $Ca = 0.2$, for various viscosity ratios λ. Circles depict the low-velocity – high-pressure point.

the orientation angles and the magnitude of the maximum stresses for these cases.

Interestingly, the maximum stresses do not occur at a point which defines the longest axis of the ellipse, i.e. the orientation of the maximum stress does not align with θ. This trend is evidently enhanced as λ and $2R/H$ increase. In addition, the equi-viscous droplet which presents the highest values of deformation shows also the highest developed shear stresses on its surface are in $2R/H = 0.4$. The discrepancy between the orientation of the deformation and the maximum shear stress, which is evidently larger for $\lambda = 3$, also plays a signicant role.

This discrepancy is even more pronounced in $2R/H = 0.7$, in which case the equi-viscous is again more deformed, albeit the stresses are greater for the high-viscous droplet. An additional reason is that the equi-viscous droplet is less resistant to deforming, due to the smaller viscosity comparing to the droplet of $\lambda = 3$.

Finally, the percentage increase of the stress components for each viscosity ratio between confinement ratios $2R/H = 0.4$ and 0.7 is *three to four* times larger than the respective increase from $2R/H = 0.18$ to 0.4. This difference correlates to the increased significance of wall approximation on the deformation parameter above $2R/H = 0.4$.

Table 3.1: Orientation angles (θ) and maximum stresses magnitude $\|\vec{T}\|$, in l.u. in the order of E-06.

	$2R/H = 0.4$		$2R/H = 0.7$	
	θ	$\|\vec{T}\|$	θ	$\|\vec{T}\|$
$\lambda = 0.3$	36.35°	15.1	31.3°	18.6
$\lambda = 1$	31.67°	19.8	28.88°	26.4
$\lambda = 3$	25.94°	18.5	24.68°	27.7
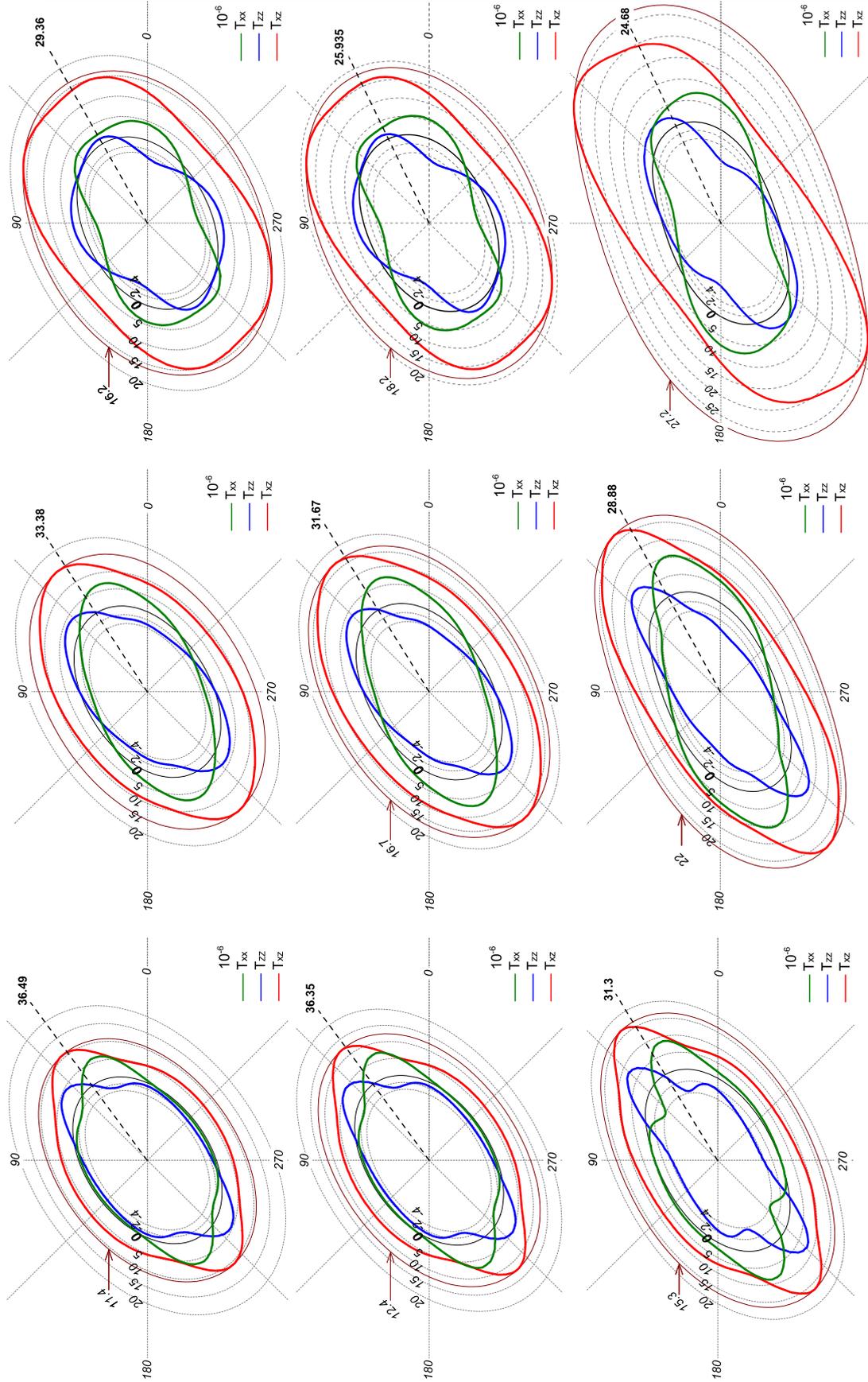
Figure 3.8: Stresses on Newtonian droplets confined in Newtonian fluid.
Left to right: $\lambda = 0.3$, 1, 3. Top to bottom: $2R/H = 0.18$, 0.4, 0.7.

(a) $\lambda = 0.3$

(b) $\lambda = 1$

(c) $\lambda = 3$

l
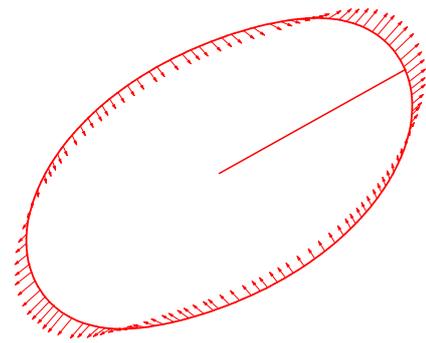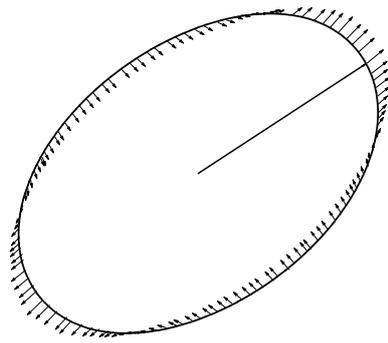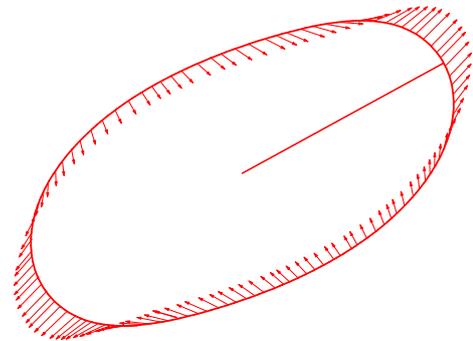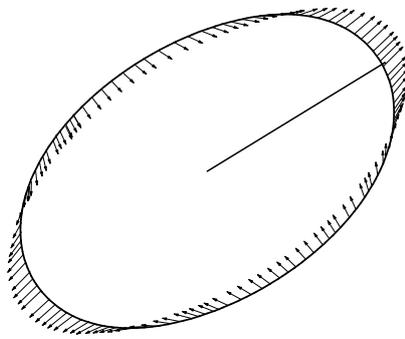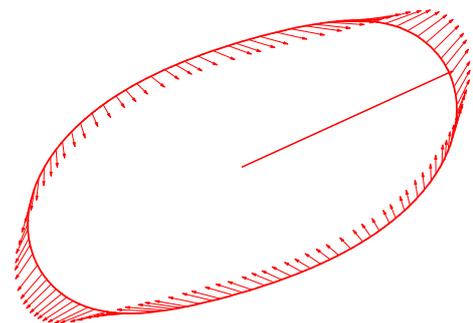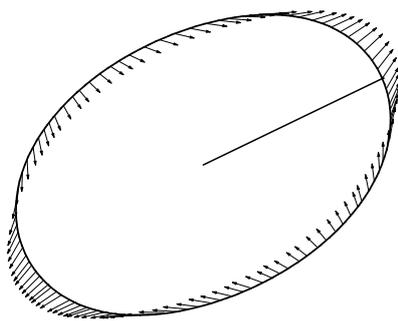
Figure 3.9: Droplets shapes and stresses on the surface in confinement ratios (left) $2R/H = 0.4$, and (right) $2R/H = 0.7$, in the $x - z$ middle plane at $Ca = 0.2$, for various viscosity ratios λ.

3.2.2   Power-law Matrix Fluid

In this section the matrix fluid obeys the power-law relation, equation (2.6)

$$\eta\left(|\dot{\gamma}|\right) = k\left(|\dot{\gamma}|\right)^{n-1}. \qquad (3.1)$$

In the rest of the *Chapter* the viscosity, the consistency parameter and the power-law exponent of the matrix fluid are referred to as η_c, k_c and n_c, respectively. Experimental and analytical studies on droplet sheared in power-law matrix fluid are scarce

The first tests consider two power-law carrier fluids of exponents $n_c = 0.75$ and 1.25 in varying shear intensity, i.e. the capillary number varies from $Ca = 0.1$ to 0.3. Three confinement ratios $2R/H = 0.18$, 0.4, and 0.7 are simulated. Figure (3.10) shows the deformation parameter on the left-hand side and the respective orientation angle on the right-hand side as a function of the capillary number for specific confinement ratios. The results for the Newtonian matrix fluid $(n_c = 1)$ are illustrated for comparison.

The results show that a droplet deforms and orients to the direction of the shear flow to higher degrees with increasing exponent. Moreover, with increasing capillary numbers the deformation parameter curves diverge with respect to each other. The difference becomes bigger in higher confinement ratios. Noteworthy, the orientation angle curve does not show this behaviour, except for the exponent $n_c = 1.25$ at $2R/H = 0.7$. This observation shows that, upon shear intensification or walls proximity the deformation is clearly affected to a higher degree than the tumbling of the droplet. The droplet response to the increase of confinement is the same for every exponent tested, except for the case $n_c = 1.25$ in $2R/H = 0.7$ at $Ca > 0.2$. Complementary plots in Appendix B, figure (B.3), further illustrate this feature.

Further more, while keeping the capillary number fixed at $Ca = 0.2$, the *effects of confinement* are studied. Figure (3.11) shows the variation of the deformation parameter and the orientation angle as a function of the confinement $2R/H$. For every exponent value, increasing confinement leads to more deformed droplets which are more oriented towards the shear flow. Additionally, the droplet deforms and tumbles to greater extents in a shear-thickening carrier fluid $(n_c > 1)$ than in a Newtonian carrier fluid $(n_c = 1)$. More shear-thickening fluids enhance these behaviour character-

istics. When the carrier fluid is shear-thinning ($n_c < 1$) the droplet acts to the opposite behaviour. The droplet deforms and tumbles less in a more shear-thinning matrix fluid.

The pressure and velocity fields are similar to the equi-viscous Newtonian case. The difference is that the *low-velocity* point shifts further from the droplet surface and slightly closer to the centreline when the matrix fluid becomes more shear-thickening. The exact opposite events happen within a more shear-thinning matrix fluid. These facts are related to the orientation angles, which are shown in figure (3.11(b)).

To support the findings regarding the deformation, the stress components on the surface of the droplet are illustrated for three power-law exponents $n_c = 0.75, 1, 1.25$ in three confinement ratios $2R/H = 0.18, 0.4, 0.7$. The images reveal that the stresses are qualitatively similar but quantitatively different. Clearly, the more confined the droplet the higher shear stresses are exerted on its surface. Additionally, shear stress components become larger as the power-law exponent increases. The percentage increase can explain the behaviour of the deformation curves in figure (3.11(a)). In a specific confinement, from left to right the increment from $n_c = 0.75$ to 1 leads to the same percentage increase as the increment from 1 to 1.25. Therefore, the deformation parameter presents a constant deviation with increasing exponent at a specific confinement.

Between confinements $2R/H = 0.18$ and 0.4 the percentage increase of the maximum shear stress increases with increasing exponents, i.e. 8.5, 11.3 and 12.3 % for $n_c = 0.75, 1, 1.25$, respectively. This observation reflects in the difference among the inclination of the deformation curves. Even more, for each exponent the increase of the shear stress from confinement ratio 0.4 to 0.7 is three times higher than the increase from 0.18 to 0.4. This correlates to the similar degree of increment in the inclination of the deformation curves.

Figure (3.13) shows the stress vectors on the droplets and the orientation angle for three power-law exponents for $2R/H = 0.4$, on the left-hand side, and $2R/H = 0.7$ on the right-hand side. Notice, that the orientation of the droplet does not coincide with the orientation of the maximum stress vector. However, the trend of discrepancy is similar for all power-law exponents tested. Additionally, table (3.2) presents the orientation angles and the magnitude of the maximum stresses for these cases.
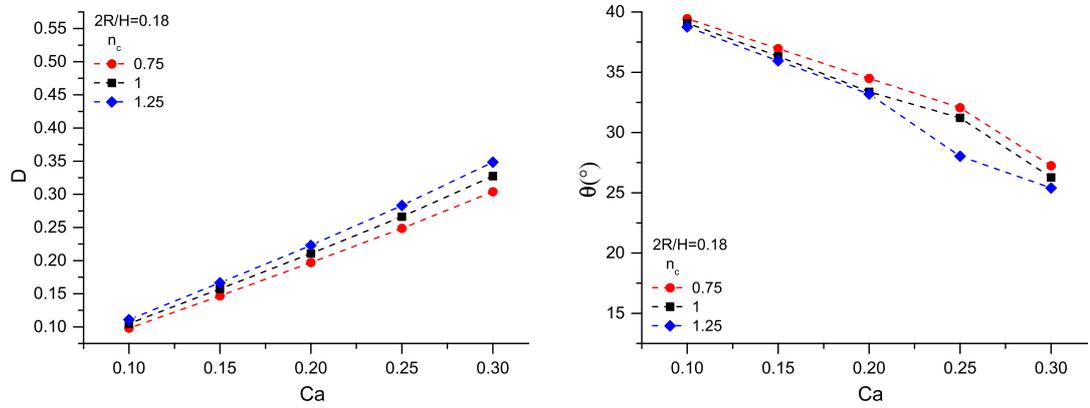
(a) 2R/H=0.18
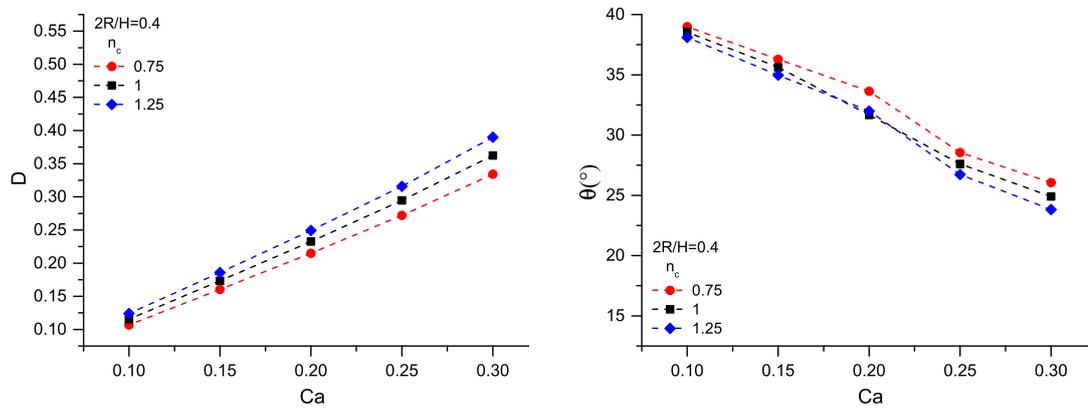
(b) 2R/H=0.4
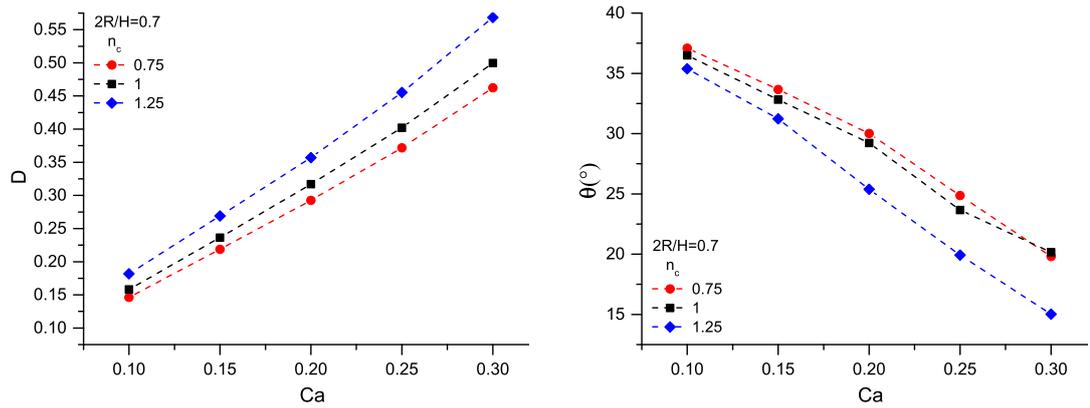
(c) 2R/H=0.7

Figure 3.10: (Left) Deformation parameter, and (right) orientation angle as a function of the capillary number Ca for various power-law exponents in three confinement ratios $2R/H = 0.18, 0.4, 0.7$.
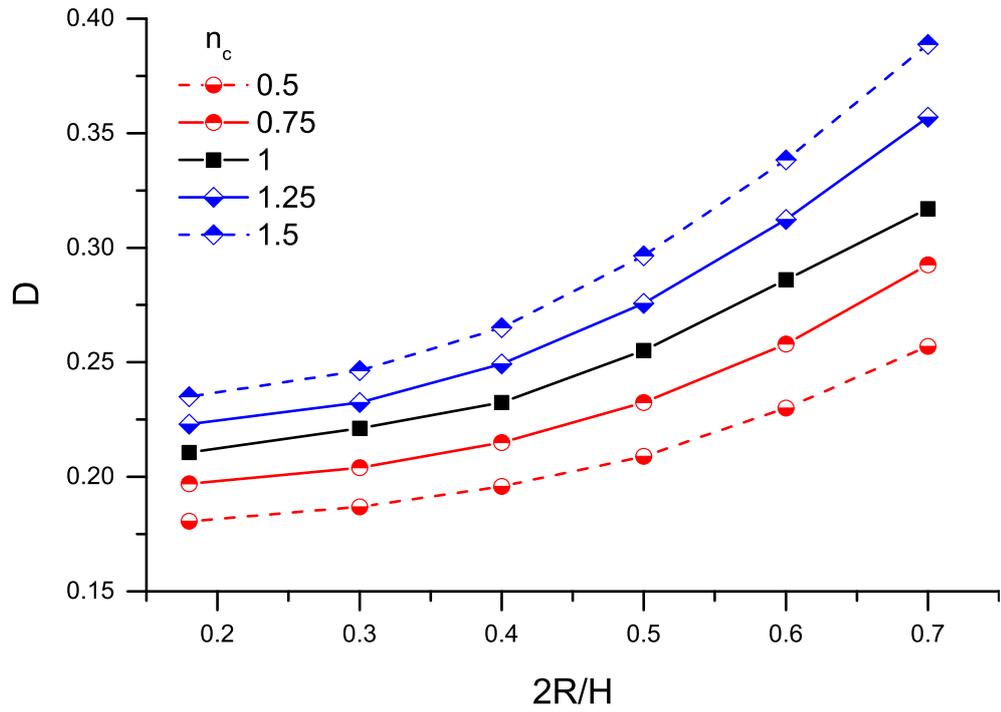
(a)
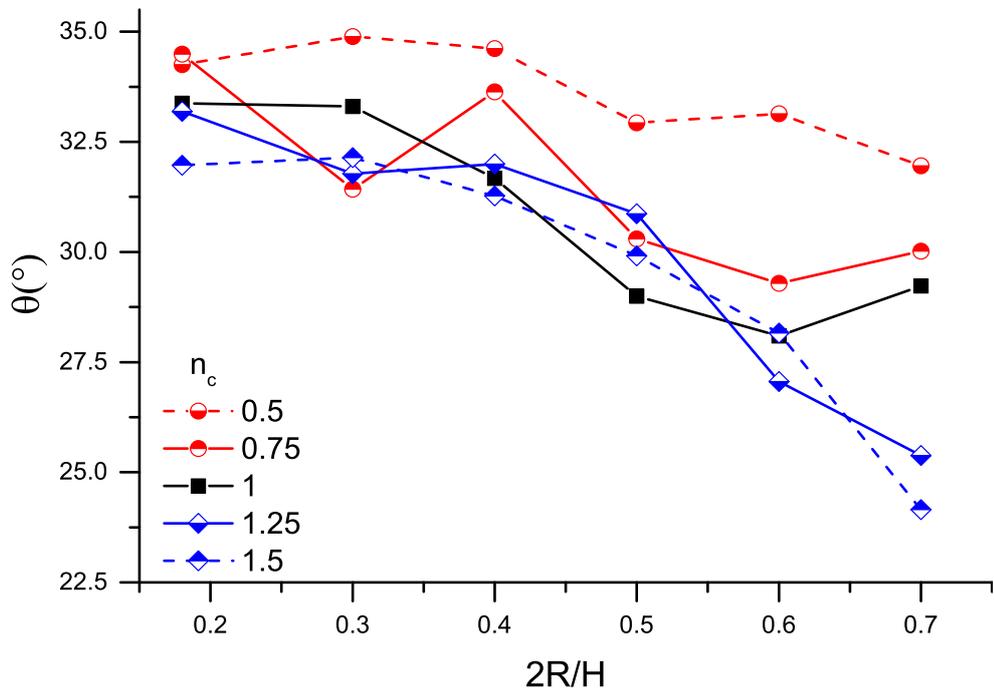
(b)

Figure 3.11: (a) Deformation parameter, and (b) orientation angle as a function of the confinement ratio, $2R/H$, for various power-law exponents, n_c, at $Ca = 0.2$.
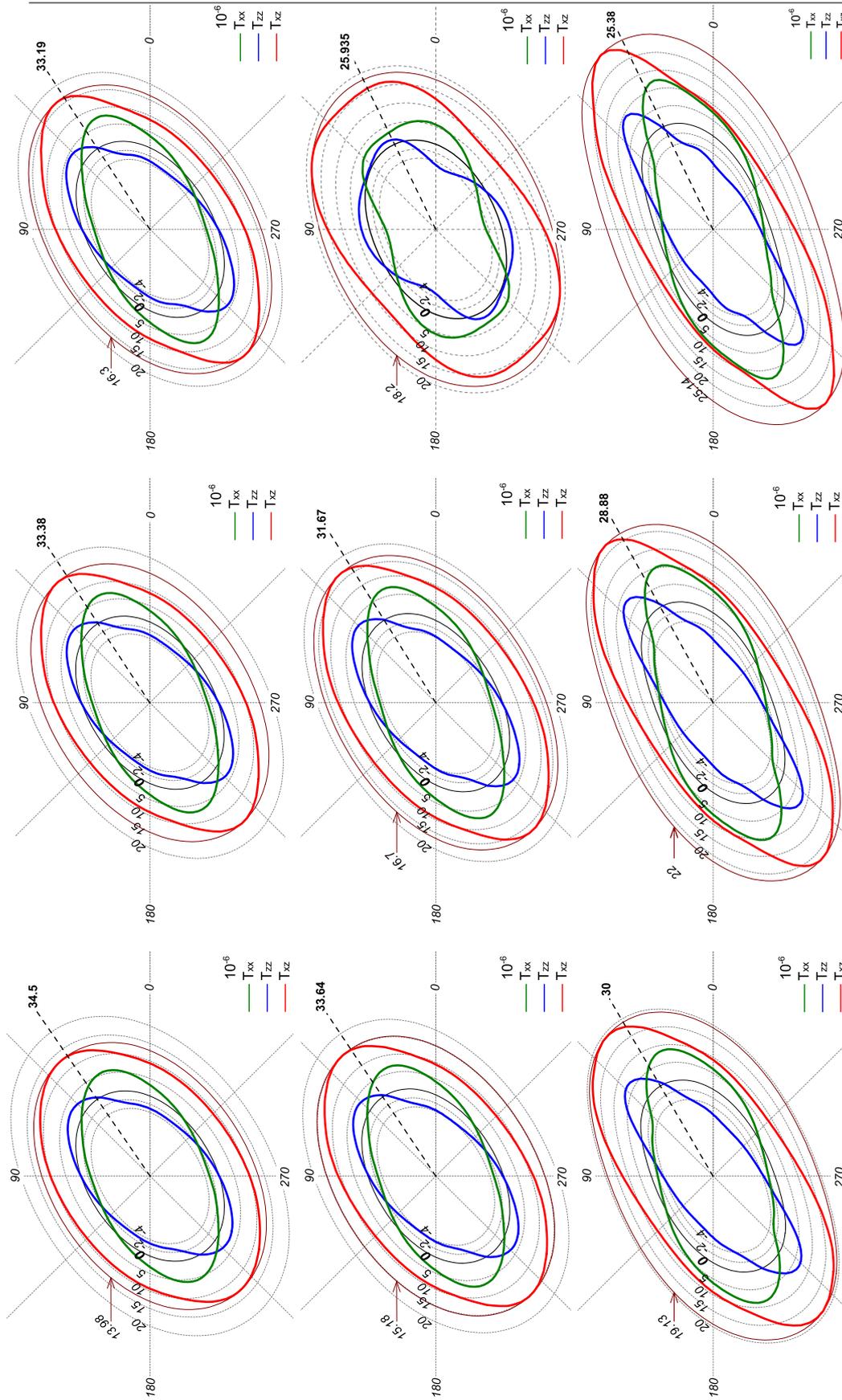
Figure 3.12: Stresses on Newtonian droplets confined in power-law fluid.
Left to right: $n_c = 0.75$, 1, 1.25. Top to bottom: $2R/H = 0.18$, 0.4, 0.7.
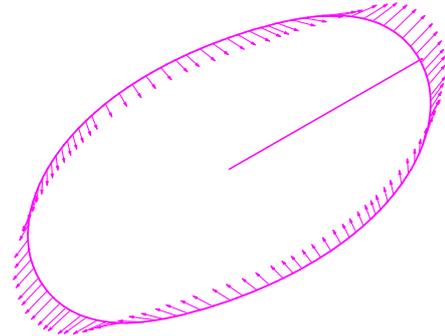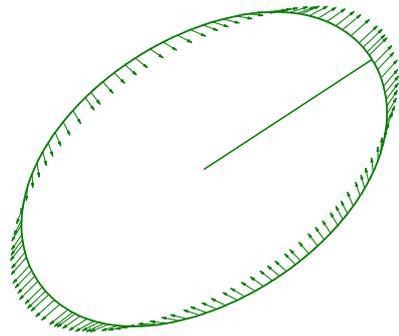
(a) $n_c = 0.75$
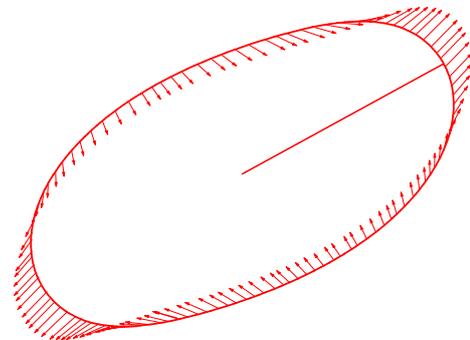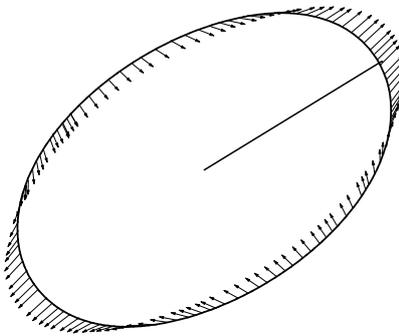
(b) $n_c = 1$ (Newtonian with $\lambda = 1$)
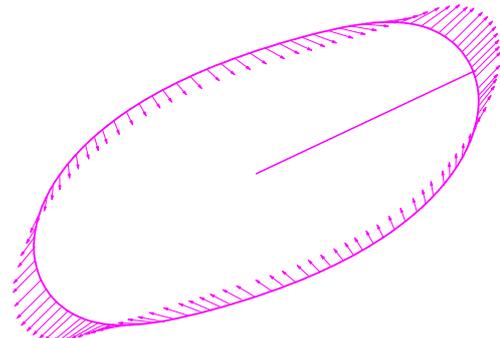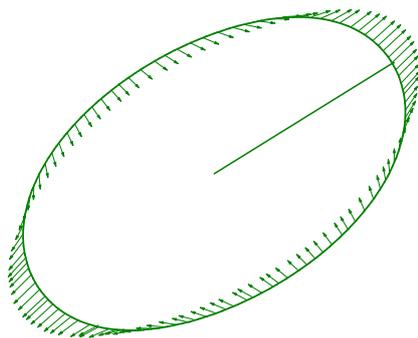
(c) $n_c = 1.25$

Figure 3.13: Droplets shapes and stresses on the surface in confinement ratios (left) $2R/H = 0.4$, and (right) $2R/H = 0.7$, in the $x - z$ middle plane at $Ca = 0.2$, for various power-law exponents n_c.

Table 3.2: Orientation angles (θ) and maximum stresses magnitude $\|\vec{T}\|$, in l.u. in the order of E-06.

	$2R/H = 0.4$		$2R/H = 0.7$	
	θ	$\|\vec{T}\|$	θ	$\|\vec{T}\|$
$n_c = 0.75$	33.64°	17.9	30°	22.6
$n_c = 1$	31.67°	19.8	28.88°	26.4
$n_c = 1.25$	32°	21.8	25.38°	30.4

3.3 Droplet Breakup

In this section, the numerical method is used to investigate the critical capillary number for confinement ratios ranging from 0.37 to 0.8. Although the LBM has been used extensively to simulate the droplet breakup [80, 81, 82, 89], to the best of the author's knowledge at the time of writing, no studies to date have considered such a range of parameters. This is partially because of the unsolved issues of the existing models themselves, such as the artificially enlarged interface thickness and case-dependent mobility in the phase-field-based model, high spurious currents as well as the numerical instability in the interparticle-potential model.

For a Newtonian carrier fluid, the simulations consider three typical viscosity ratios, i.e. $\lambda = 0.3$, 1 and 5. For the power-law matrix fluid two exponents $n_c = 0.75$ and 1.25 are tested. Figure (3.14) shows the effect of the confinement ratio on the droplet breakup at the viscosity ratios of $\lambda = 0.3$, 1 and 5, which are represented by circles, squares, and diamonds, respectively. Empty symbols represent the steady state regime. Half-filled and full-filled symbols distinguish the binary and ternary breakup modes. The dashed lines are illustrated to guide the eye and do not show the specific Ca_{cr}. The same graph includes two cases of breakup in a power-law matrix fluid. The green ellipses show the cases for $n_c = 0.75$ and the purple for $n_c = 1.25$. Crossed symbols denote binary breakup. Following the aforementioned definitions, the critical capillary number (Ca_{cr}) lies between the empty and filled or crossed symbols (the lines for the power-law matrix fluid are not illustrated).

The confinement ratio has different effects on the critical capillary number, depending on the viscosity ratio. For the low viscosity ratio, i.e. $\lambda = 0.3$, the critical capillary

Figure 3.14: The effect of capillary numbers and confinement ratio on the droplet steady deformation or breakup. The open symbols depict steady states. The half-filled symbols depict binary, and the full symbols ternary breakups for the Newtonian cases, while the crossed symbols show binary breakup for droplets in power-law matrix fluid.

number is varied from $0.4 \leq Ca_{cr} \leq 0.5$ at $2R/H = 0.37$, to $0.5 \leq Ca_{cr} \leq 0.6$ at $2R/H = 0.5$ and finally to $0.55 \leq Ca_{cr} \leq 0.625$ at $2R/H = 0.625$, suggesting that Ca_{cr} increases with increasing confinement. Figure (3.15) shows the snapshots of the droplet breakup process for $Ca = 0.625$, $\lambda = 0.3$ and $2R/H = 0.625$. The droplet elongates to a high degree in worm-like shape until $t^* = 8$. At $t^* = 16$ along with the increased elongation, disturbances on the surface appear to grow more intensely. The combined effects from the shearing and capillary instabilities result in a pinch off point in the middle of the droplet. The breakup results into two daughter droplet of sigmoidal shapes.

Contrary to the low viscosity ratio case, Ca_{cr} decreases with increasing confinement for the high viscosity ratio, i.e. $\lambda = 5$. Specifically, the critical capillary number decreases from $0.5 \leq Ca_{cr} \leq 0.6$ to $0.3 \leq Ca_{cr} \leq 0.35$ when the confinement ratio increases from 0.55 to 0.8. Figure (3.16) shows the snapshots of the droplet breakup process for $Ca = 0.35$, $\lambda = 5$ and $2R/H = 0.8$. The droplet deforms continuously

and eventually breaks up into two equal-sized daughter droplets, as opposed to the unbounded case where the high viscosity ratio droplet ($\lambda > 4$) does not break regardless of the capillary number.

Furthermore, figure (3.14) shows that the confinement ratio has a small effect on the critical capillary number for $\lambda = 1$, which is around 0.4. These findings agree well with the previous experimental and numerical studies [23, 38]. However, it is found for $\lambda = 1$, through a large number of experiments and simulations, that the critical capillary number first decreases slightly and then increases slightly with a minimum capillary number occurring at $2R/H = 0.5$. This subtle variation of the critical capillary number with the confinement ratio requires a large number of simulations to be captured.

Even though the overall agreement is quite satisfactory between the present results and those obtained by Janssen et al. [23], some quantitative differences are also noticed. For example, Janssen et al. [23] finds experimentally that binary breakup occurs for a unit viscosity ratio droplet at $Ca = 0.45$ and $0.37 \leq 2R/H \leq 0.45$, where our simulations produce a ternary breakup. Figure (3.17) shows the snapshots of the droplet breakup process for $Ca = 0.45$, $\lambda = 1$ and $2R/H = 0.45$. As the droplet is stretched by the external shear flow, it first deforms to an ellipsoidal shape ($t^* = 4$). The major axis lengthens while the minor axis shrinks, leading to the formation of a neck near the centre of the droplet at $t^* = 16$. The droplet is then elongated to a 'dumbbell-like' shape, and at the same time the bulbs at the end of the droplet achieve a stable shape ($t^* = 20$). At $t^* = 26$, two visible necks are formed between the central portion of the droplet and the bulbs. The droplet continues to thin and eventually breaks up into three parts. The two daughter droplets have much larger size than the one residing in the centre ($t^* = 28$).

In addition, the previous experimental study indicates that the lowest Ca_{cr} for all of viscosity ratios ($0.3 \leq \lambda \leq 5$) and confinement ratios ($0.1 \leq 2R/H \leq 0.9$) is around 0.4 [23]. However, our simulations produce the lowest Ca_{cr} between 0.3 and 0.35, which can be clearly seen in figure (3.14). The reason for these differences remains unclear, and is likely to be the result of a combination of factors, such as the experimental errors, model accuracy in describing the interfacial dynamics, or other uncertainties.

In the cases where the droplets are immersed in a shear-thinning or thickening

fluid the critical capillary number is lower. In the confinement $2R/H = 0.4$, the Ca_{cr} lies between 0.35 and 0.4, for $n_c = 0.75$ and decreases slightly for confinement to 0.7, between 0.3 and 0.35. The respective range for $n_c = 1.25$ is between 0.3 and 0.35 in both confinements. Finally, for each exponent the breakup events are similar to the equi-viscous Newtonian cases.

3.4   Conclusions

The influence of the capillary number, confinement and viscosity ratios are systematically studied for a Newtonian droplet sheared in a Newtonian carrier fluid. When the matrix fluid is described by a power-law relation, the power-law exponent replaces the viscosity ratio in the investigations.

In the first section, our numerical method is validated through comparisons with the available experimental and numerical data in the literature. The phenomenological model MMSH, whose predictive accuracy is verified by the experimental data, provides further support to the numerical method in cases of moderate confinements at various viscosity ratios.

Further on, the impact of confinement on different viscosity ratios is investigated. The increasing confinement leads to greater droplet deformation for a wide range of viscosity ratios. The equi-viscous droplet, i.e. the droplet of the same viscosity as the carrier fluid, presents the greatest deformation in every confinement ratio. Regarding the orientation angle of the deformed droplet, it decreases with increasing confinement or viscosity ratios. Moreover, the presence of the walls has a higher impact on the droplet deformation when the confinement ratio becomes equal to or higher than $2R/H = 0.4$.

Complimentary, the behaviour of the droplet is linked to the pressure and velocity fields and stresses on the droplet surface. The shear stimulates a droplet to orient to a specific degree towards the direction of the flow. Low-viscous droplets orient less than high-viscous ones. Upon wall approximation the developed stresses on the droplet increase with a different rate for each case. Additionally, the orientation adjusts in a different way for every viscosity ratio. For example, for $\lambda < 1$ a droplet turns by considerably more degrees than for $\lambda > 1$. This behaviour couples with the shear

(a) $t^* = 0$

(b) $t^* = 1$

(c) $t^* = 8$

(d) $t^* = 16$

(e) $t^* = 24$

(f) $t^* = 29$

(g) $t^* = 30$

(h) $t^* = 31$
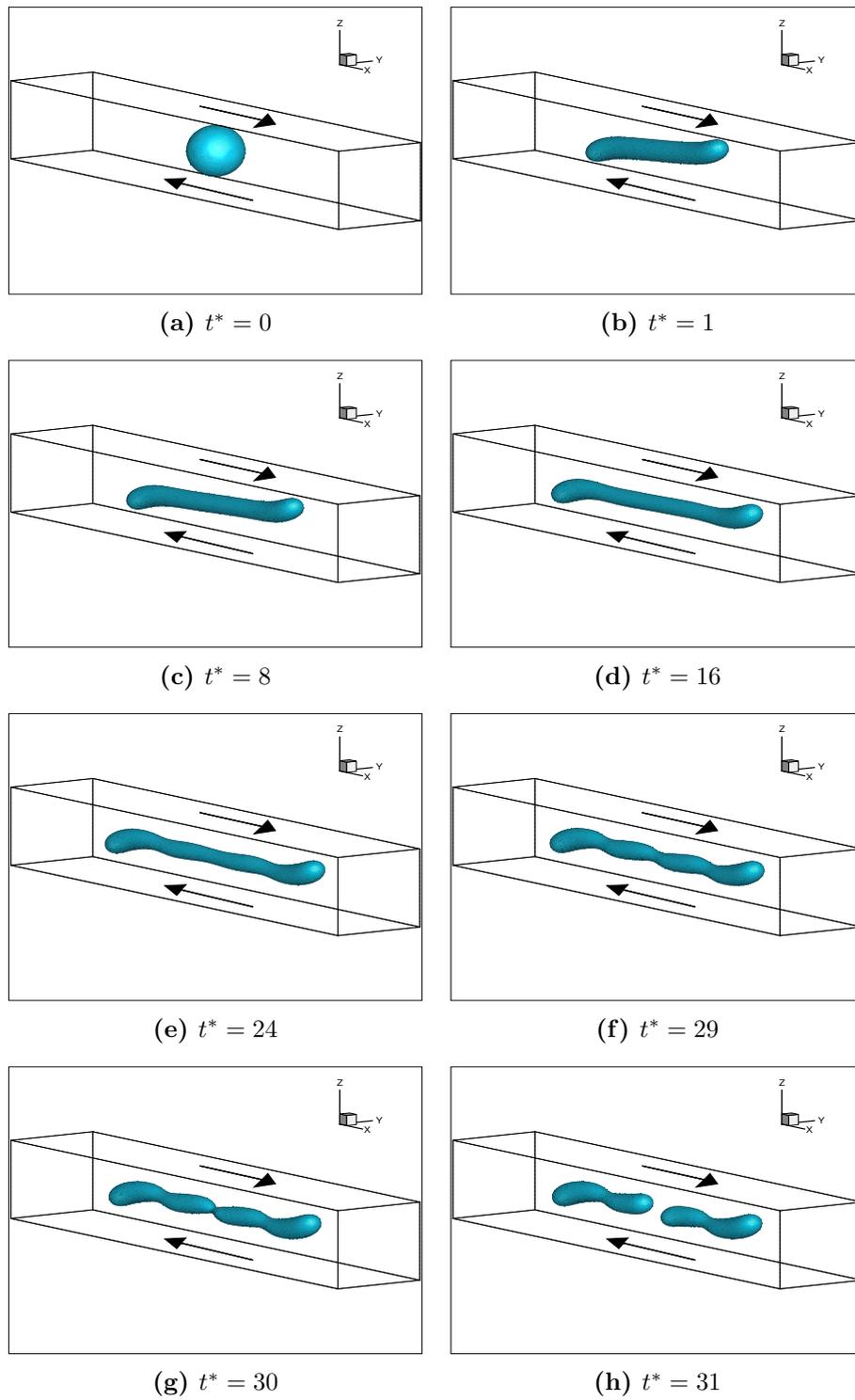
Figure 3.15: Transient droplet shape for $Ca = 0.625$, $\lambda = 0.3$, and $2R/H = 0.625$.

(a) $t^* = 0$ **(b)** $t^* = 4$

(c) $t^* = 9$ **(d)** $t^* = 17$

(e) $t^* = 25$ **(f)** $t^* = 34$

(g) $t^* = 38$ **(h)** $t^* = 39$
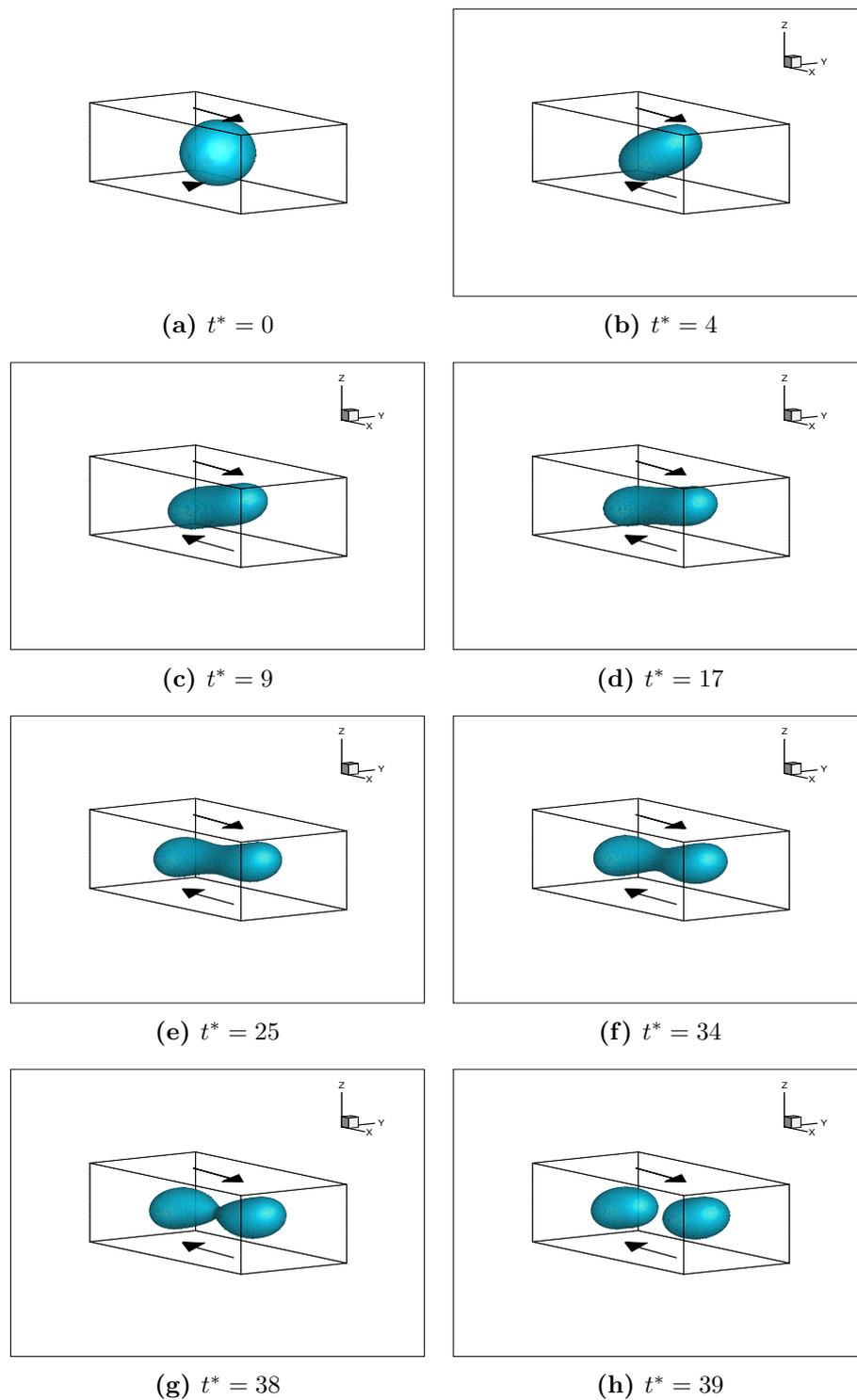
Figure 3.16: Transient droplet shape for $Ca = 0.35$, $\lambda = 5$, and $2R/H = 0.8$.

(a) $t^* = 0$ **(b)** $t^* = 4$

(c) $t^* = 8$ **(d)** $t^* = 12$

(e) $t^* = 16$ **(f)** $t^* = 20$

(g) $t^* = 26$ **(h)** $t^* = 28$
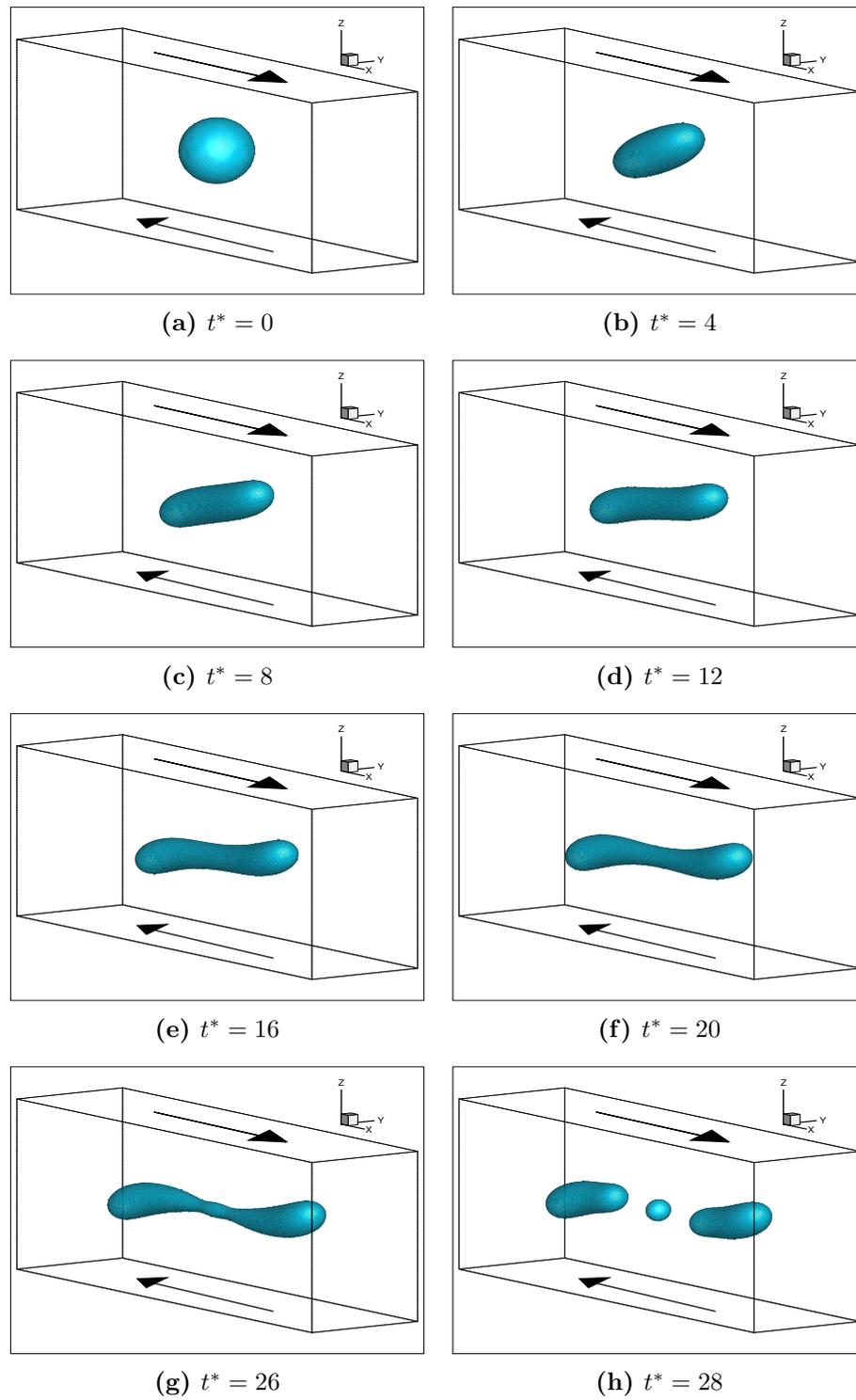
Figure 3.17: Transient droplet shape for $Ca = 0.45$, $\lambda = 1$, and $2R/H = 0.4$.

stress increment. These events result to distinctive deformation behaviours in increasing confinements, i.e. low deviations for $\lambda < 1$ and high deviations for $\lambda > 1$. The case of $\lambda = 1$ is characteristic: it presents the greatest deformation although its orientation behaviour dictates that it would deform less than the high-viscous one. The key element is the magnitude of the shear stress, at the point which dictates the direction of orientation.

For a droplet immersed in a power-law matrix fluid, again, increasing confinement leads to an increase in droplet deformation for a wide range of power-law exponents. The orientation angle of the deformed droplet decreases with increasing confinement ratio or exponent. The correlated increase of the maximum shear stress leads to evenly deviation in the deformation parameter.

Finally, the critical capillary number is investigated for a broad range of flow conditions. Depending on the value of the viscosity ratio, the confinement ratio has different effects on the critical capillary number: as the confinement increases, the critical capillary number increases for $\lambda < 1$, but decreases for $\lambda > 1$. Specifically, for $\lambda = 1$ the critical capillary number is kept at a value of around 0.4, regardless of the confinement ratio. When the droplet is immersed in a shear-thinning or thickening matrix fluids, it experiences breakup under less intense shearing than in the equal viscosity Newtonian fluid. The confinement plays an insignificant role in this case.

Chapter 4

Power Law Droplets in Shear

4.1 Introduction

The previous *Chapter* discusses Newtonian droplets which are sheared in Newtonian or power-law matrix fluids. This *Chapter* investigates the behaviour of sheared droplets made of power-law fluids. In the rest of this work, these type of droplets are also referred to as 'power-law droplets'.

To the author's knowledge at the time of writing, numerical studies are scarce in the literature for the simple shear of a single power-law droplet. For example, the behaviour of shear-thinning droplets in *circular/rotational* Couette flow is studied in [21] using the boundary element method (BEM). The same numerical method is utilised in the investigation of the droplet mobility [42], i.e. the relative motion upon shear of two droplets in close proximity, one of which lies in the centre of the domain.

This *Chapter* is structured as follows. First, it introduces specific simulation settings and aspects for the power-law droplet shearing cases, which are not described in *Chapter* 2. The following sections present and discuss the results, and conclude with a summary of the findings.

4.2 Simulation Setup

To begin with, the viscosity, consistency index and the exponent of a power-law droplet are noted with η_d, k_d and n_d, respectively. Moreover, a droplet is characterised as shear-

thinning for $n_d < 1$, Newtonian for $n_d = 1$, and shear-thickening for $n_d > 1$. Note that in all cases the matrix fluid is Newtonian; therefore the respective systems are referred to as *'Power-law–Newtonian'*. In the distinct case of $n_d = 1$, i.e. a Newtonian droplet is sheared, the respective system is referred to as *'Newtonian–Newtonian'*.

Comparisons between *Newtonian–Newtonian* and *Power-law–Newtonian* systems are helpful to characterise the behaviour of power-law droplets. Therefore, the same setup conditions are used here as in *Chapter* 3 for the *Newtonian–Newtonian* systems.

Supplementary, to set the consistency index of the power-law fluids, a similar artificial number to the viscosity ratio λ is defined as *power-law viscosity ratio* expressed as

$$\lambda_{(PL)} = k_d/\eta_c. \tag{4.1}$$

Hence, with the viscosity of the matrix fluid (η_c) set as described in Chapter 2, the value of $\lambda_{(PL)}$ determines the value of k_d. Notice that the term 'power-law' is preferred in this work as more consistent with the topic, unlike the term "non-Newtonian viscosity ratio" depicted as λ^{NN} in [21] which would correspond to a more general type of fluids.

Using the definitions of the imposed shear rate magnitude, $\dot{\gamma}_0 = 2U/H$, and the single phase power-law formulation, $\eta_d = k_d\dot{\gamma}_0^{n_d-1}$, equation (4.1) leads to the so-called *equivalent viscosity ratio* of a *Newtonian-Newtonian* system as:

$$\lambda_{eq} = \lambda_{(PL)}\dot{\gamma}_0^{n_d-1}. \tag{4.2}$$

Expression (4.2) correlates two systems: a *Newtonian–Newtonian* with characteristic parameter λ_{eq} to a *Power-law–Newtonian* with characteristic parameter n_d. This correlation is possible because in both systems the stresses exerted on the surface of the droplet depend on the term $\eta_c\dot{\gamma}_0$. The same dimensionless number as used in [13] (see p.82 therein) is referred to as "apparent viscosity ratio" and depicted with λ_a. In the rest of this *Chapter* the aforementioned systems are noted as '*N-N*/λ' and '*PL*-N/n_d', for short. Note that equation (4.2) is useful for non-unity magnitudes of shear rate.

In the simulations, the shear rate magnitude is lower than unity, e.g. $\dot{\gamma}_0 = 5 \times 10^{-5}$ (see *Chapter* 2, Section 2.4.3). Hence, the aforementioned correlation leads to two most important assumptions:

1. shear-thinning droplets, i.e. $n_d < 1$, would behave like high-viscous Newtonian, i.e. $\lambda > 1$,

2. shear-thickening droplets, i.e. $n_d > 1$, would behave like low-viscous Newtonian, i.e. $\lambda < 1$.

Nevertheless, as depicted in figure (3.7) and also stated in [13] the flow patterns in the interior of a Newtonian droplet, where viscosity is constant, cannot be straightforwardly predicted. This fact is even more emphasised in the present cases in which the velocity gradients affect strongly the viscosity patters inside a droplet. This observation would affect the validity of the aforementioned assumptions. However, our results show that despite the different interior viscosity fields in the equivalent Newtonian and the power-law droplets, their interior flow patterns and the final droplet shapes in the steady state regime are indistinguishable.

Clearly, the magnitude of the imposed shear rate varies with the capillary number. Hence, a specific value of n_d leads to different equivalent viscosity ratios with varying capillary numbers. For example, for $n_d = 1.125$ and $\lambda_{(PL)} = 1$ at $Ca = 0.2$ the equivalent viscosity ratio is $\lambda_{eq} \approx 0.29$. However, at $Ca = 0.4$ the value of $\lambda_{(PL)}$ exceeds 0.3. Assuming $\lambda_{(PL)} = 1$ and for various capillary numbers ranging from 0.1 to 0.5, table (4.1) shows the values of λ_{eq} when $n_d = 1.125$. This example is extended to the opposite case, i.e. table (4.1) also shows values of n_d which lead the equivalent viscosity ratio 0.3. Therefore, the correlation between n_d and λ_{eq} depends on the capillary number.

Table 4.1: Equivalent viscosity ratio (λ_{eq}) for exponent $n_d = 1.125$, and exponent value (n_d) to achieve equivalent viscosity ratio $\lambda_{eq} = 0.3$, for capillary numbers ranging from 0.1 to 0.5, and $\lambda_{(PL)} = 1$.

Ca	0.1	0.2	0.3	0.4	0.5
$n_d = 1.125$, λ_{eq}	0.27768	0.28998	0.2974	0.3028	0.30705
$\lambda_{eq} = 0.3$, n_d	1.11746	1.12157	1.12411	1.12598	1.12747

4.3   Results

4.3.1   Droplet Deformation in Two Dimensions

The study of the problem in 2D provides a "quick" insight into the behaviour of the power-law droplets. However, the physics implied in 2D simulations may differ from the three dimensional (3D), especially at large capillary numbers [79]. Therefore, three dimensional simulations are also conducted including the breakup case which is presented in the next section. Note that, the confinement is set to $2R/H = 0.4$ in every 2D simulation, to ensure small wall influence (see *Chapter* 3) and low computational cost.

The first tests are conducted for fixed $Re = 0.1$, $Ca = 0.2$, and $\lambda_{(PL)} = 1$, while the power-law exponents range from $n_d = 0.5$ to 1.4. Note that in [84] the power-law index takes values $0.6, 1, 1.4$.

Figure (4.1) compares the characteristics of two *PL-N* systems: $n_d = 0.5$ and $n_d = 0.6$. More specifically, figure (4.1(a)) illustrates the shapes of the two droplets which match identically. On the other hand, the plots of the relaxation parameter along the centreline at $x = 0$ show a large difference as illustrated in figure (4.1(b)). Figures (4.1(c)) and (4.1(d)) depict the flow patterns around and inside the droplets and the relaxation parameter contours separately for these exponents. Evidently, the flow-fields are identical even in the interior of the droplets, albeit the large variations between the relaxation parameters (or viscosities). This resemblance indicates the limitation of the BGK model to solve cases below a certain power-law exponent. This limitation is a consequence of the very high values of τ. The implementation of the *MRT* model in the present numerical method may resolve this issue.

Complementary, figure (4.2(a)) contrasts the shapes of droplets for every n_d, except for $n_d = 0.5$. The deformation parameters and orientation angles are plotted in figures (4.2(b)) and (4.2(c)), respectively. Droplets deform to higher extends with increasing n_d values. At $n_d = 1$ (Newtonian droplet) the deformation exhibits the greatest value. With further increase of n_d from 1 to 1.4 the deformation decreases. At all times, even for the Newtonian case, the orientation angle increases with increasing n_d values. This reflects that shear-thinning droplets align more to the flow than the Newtonian, con-

trary to the shear-thickening ones. The observations for shear-thinning and -thickening droplets relate to those in *Chapter* 3 regarding the high- and low-viscous droplets, respectively, and support the assumptions stated in Section 4.2.

Further more, the impact of the power-law viscosity ratio is examined, i.e. $\lambda_{(PL)} = 0.5, 1, 2$, at capillary numbers $Ca = 0.2$ and 0.4. In these tests the exponents are limited to values $n_d = 0.75, 1, 1.25$. The deformation parameters and orientation angles are plotted on the left- and the right-hand side of figure (4.3), respectively.

First of all, with increased Ca from 0.2 to 0.4 every droplet deforms to a greater extent and orients more to the direction of the flow. Furthermore, contrary to the findings in *Chapter* 3 the deformation of the Newtonian droplet at $Ca = 0.2$ con-
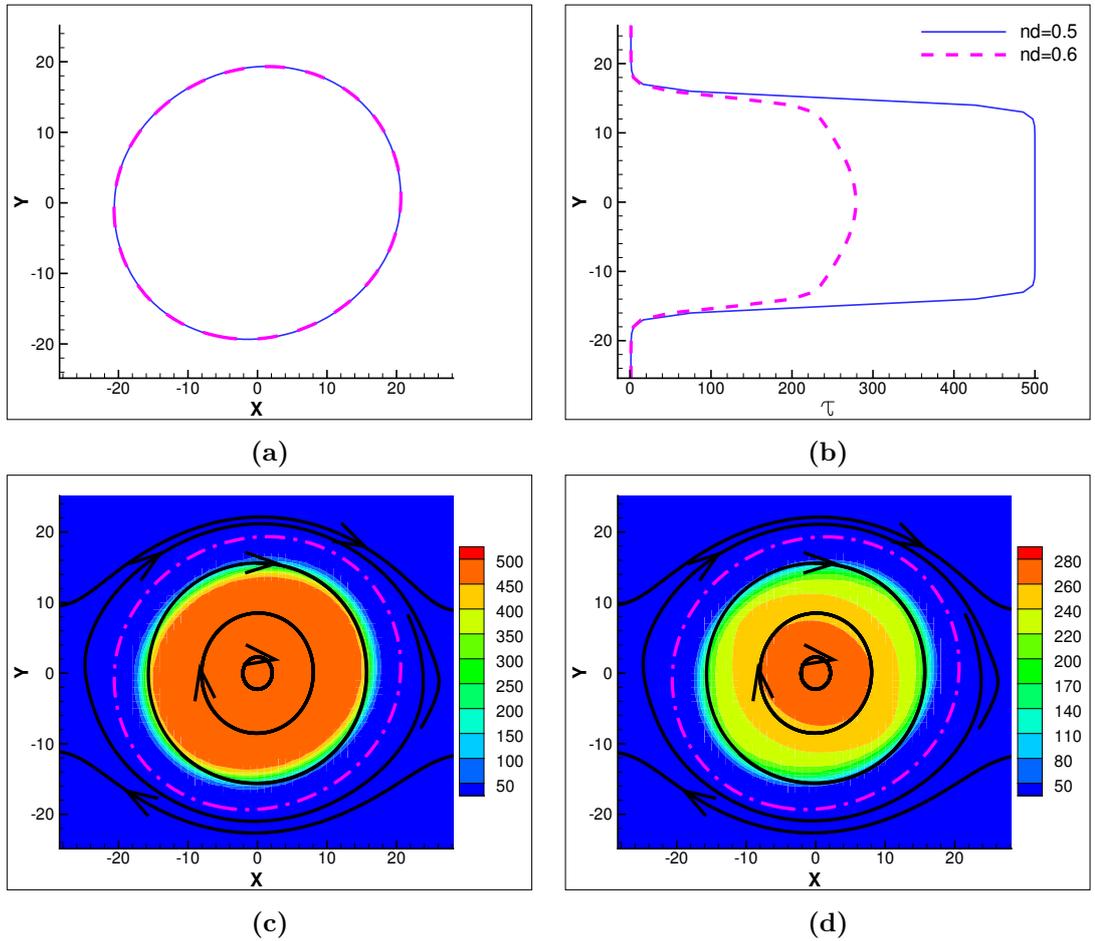
Figure 4.1: (a) Shapes of final deformed droplets and (b) relaxation parameter, τ, at $x = 0$, for $n_d = 0.5$ (blue) and $n_d = 0.6$ (dashed magenta). Shapes of final deformed droplets (dashed-dotted magenta lines), relaxation parameter (see legend for contours), and streamlines for (c) $n_d = 0.5$ and (d) $n_d = 0.6$. 2D simulations of droplet deformation at $Ca = 0.2$, $2R/H = 0.4$.

(a)

(b)

(c)
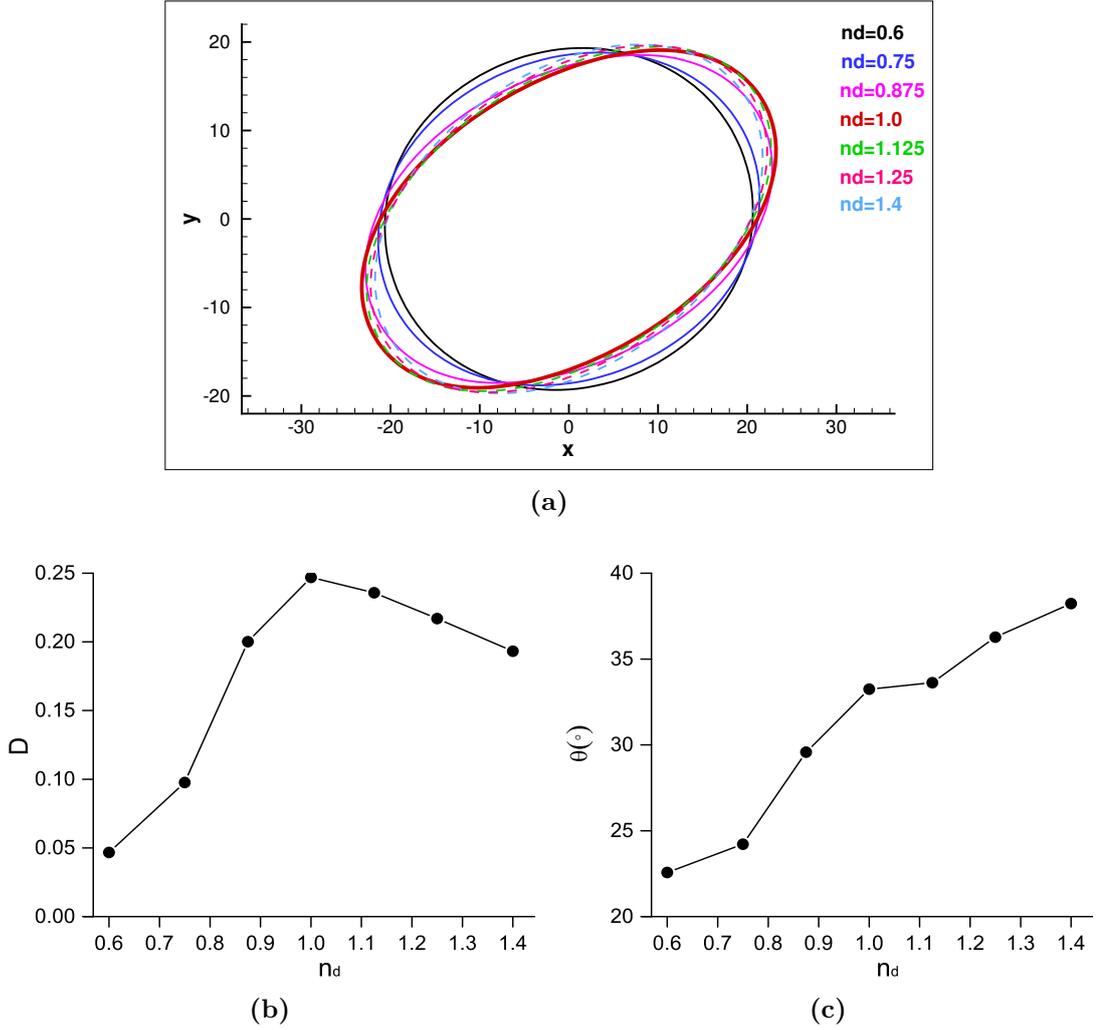
Figure 4.2: (a) Shapes of final deformed droplets for various exponents, n_d. (b) Deformation, and (c) orientation angle as a function of the droplet power-law index, n_d. 2D simulations of droplet deformation for $Ca = 0.2$, $2R/H = 0.4$.

stantly decreases with increasing viscosity ratio. The same trend is more pronounced for $Ca = 0.4$. Noteworthy, here the droplets present an ellipsoid shape, although the 3D simulations show a sigmoidal shape close to the breakup point. On the other hand, shear-thickening droplets exhibit the opposite deformation trend in comparison with the Newtonian droplets. However, both Newtonian and shear-thickening droplets orient more to the direction of the flow with increasing $\lambda_{(PL)}$. Finally, it is clear that shear-thinning droplets are affected the most. The decrease in both deformation parameters and orientation angles is rapid upon increasing viscosity ratios.

Moreover, shear-thinning droplets show the lowest orientation angles. This finding
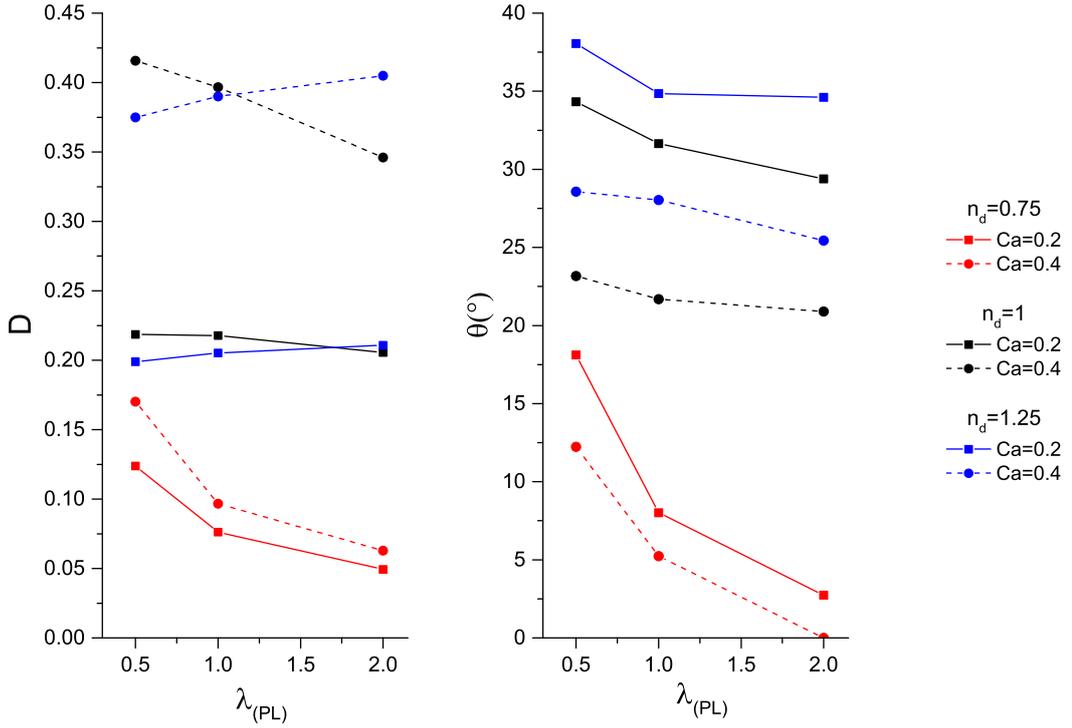
Figure 4.3: (Left) Droplet deformation, and (right) orientation angle as a function of the power-law viscosity ratio, $\lambda_{(PL)}$, for power-law exponents $n_d = 0.75, 1, 1.25$. 2D simulations in confinement ratio, $2R/H = 0.4$.

correlates with the conclusion in *Chapter* 3 that high-viscous droplets align more to the direction of the flow. Similarly, at a fixed Ca shear-thickening droplets turn less than the Newtonian. This observation relates to the low-viscous *N-N* systems. On the other hand, the same type of correlations cannot be established for the deformation, as it depends on the viscosity ratio and capillary number in a more complex way than the orientation angle.

4.3.2 Droplet Deformation in Three Dimensions

This section first reports the behaviour of power-law droplets for $n_d = 0.75, 1, 1.25$ in three dimensions. While the viscosity ratio is set to $\lambda_{(PL)} = 1$, the confinement ratios vary from $2R/H = 0.18$ to 0.4 to 0.7 to investigate the effects from the walls. Thus, the tests compare a shear-thinning, a Newtonian and a shear-thickening droplet, i.e. $n_d = 0.75, 1, 1.25$ in very weak, moderate and highly confined cases, i.e. $2R/H = 0.18, 0.4$ and 0.7.

In the tests, the capillary numbers range from 0.1 to 0.5. At $Ca = 0.5$ the correlations between power-law exponents and equivalent viscosity ratios are

- shear-thinning: $n_d = 0.75 \rightarrow \lambda_{eq} \approx 13$,

- shear-thickening: $n_d = 1.25 \rightarrow \lambda_{eq} \approx 0.08$.

The critical capillary numbers in N-N systems of such viscosity ratios exceed greatly the value of 0.5, as reported in [23], and therefore no breakups are expected. However, some droplets deviate from the ellipsoid shape, e.g. for $n_d = 1.25$.

Figures (4.4(a)) and (4.4(b)) show the deformation parameters and the orientation angles as a function of Ca. Red circles plot results for $n_d = 0.75$, black squares for $n_d = 1$, and blue diamonds for $n_d = 1.25$. Confinement ratios are illustrated with a combination of symbols/lines as:

1. $2R/H = 0.18$: bottom-filled/dotted,

2. $2R/H = 0.4$: filled/solid ,and

3. $2R/H = 0.7$: top-filled/dashed.

Starting with general remarks, droplets deform to higher extents and turn more to the orientation of the flow with increasing capillary numbers and confinements. In particularly, the Newtonian droplets (black lines) present the biggest deformation, and their orientation angle trend lines lie between those for $n_d = 0.75$ and 1.25. Furthermore, droplets with $n_d = 0.75$ show the smaller values of both deformation and orientation angle (red lines). Contrariwise, droplets with $n_d = 1.25$ (blue lines) depict the highest orientation angles values, even though they deform less than the Newtonian ones.

The deformation parameter trend lines indicate that the walls increasing proximity has a weak influence on the deformation up to the degree of confinement $2R/H = 0.4$. More specifically, the increase of the confinement ratio from $2R/H = 0.18$ to 0.4 affects mildly droplets with $n_d = 0.75$ and even insignificantly with $n_d = 1.25$. However, upon further increase to $2R/H = 0.7$ droplets with $n_d = 0.75$ deform considerably more. The specific droplets are subjected to high built-up stresses on the surface due to lack of further tumbling, as indicated from the orientation angle values, in
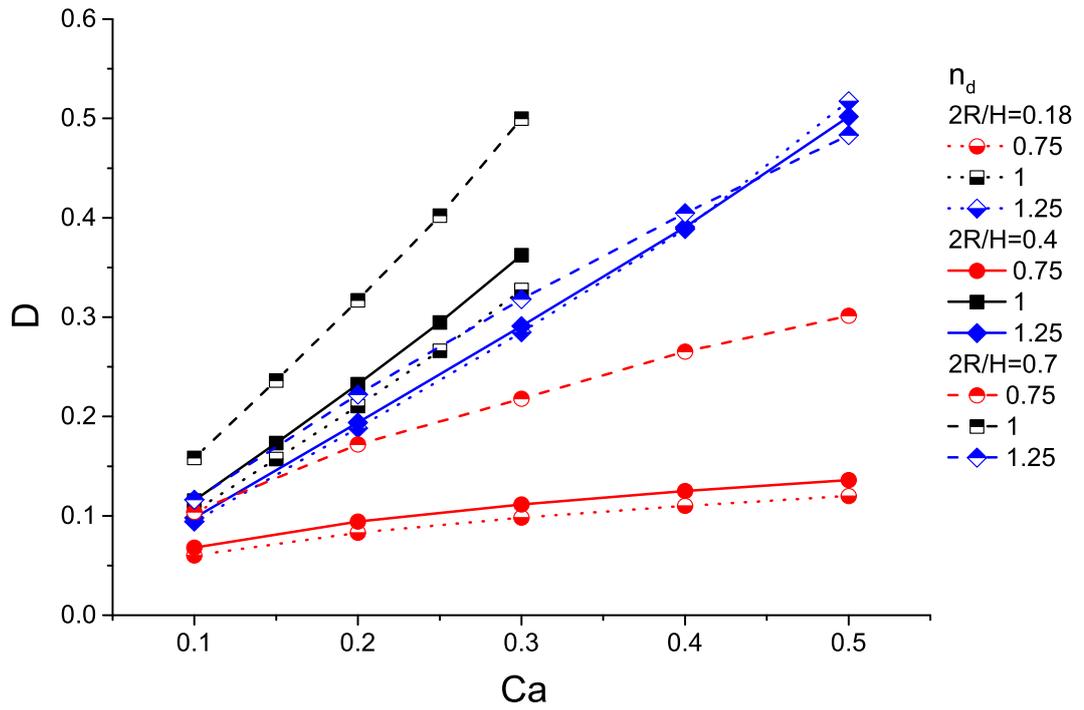
(a)
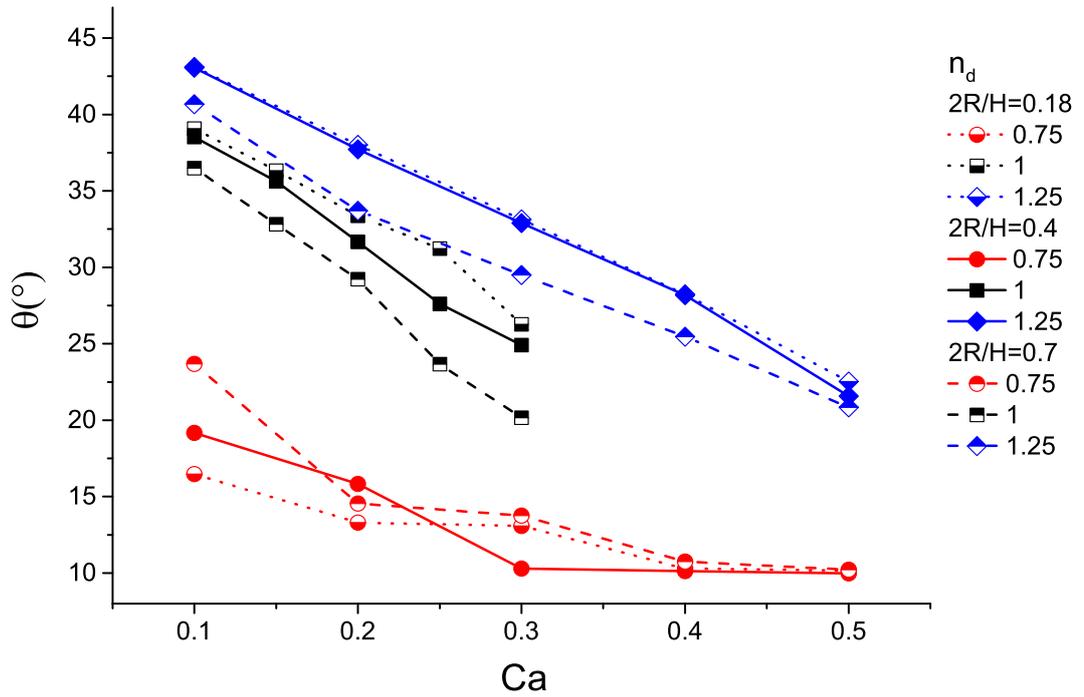
(b)

Figure 4.4: (a) Droplet deformation, and (b) orientation angle as a function of the capillary number, Ca, for exponents $n_d = 0.75$, 1, 1.25, in various confinement ratios, $2R/H$.

a similar mechanism described in *Chapter* 3 regarding the high-viscous Newtonian droplets. On the other hand, the droplets with $n_d = 1.25$ intensify their tumbling, i.e. decreasing θ in figure (4.4(b)), hence the built-up stresses have a moderate impact on the deformation. This behaviour is, also, illustrated by a low-viscous Newtonian droplet. Interestingly, in $Ca = 0.5$ the increasing confinement of droplets with $n_d = 1.25$ leads to smaller deformations. This feature cannot be explained in the framework of the present dissertation due to the very small viscosity ratio value, i.e. $\lambda = 0.08$. However, it can be linked to the finding that increasing confinement suppresses breakup for low viscosity Newtonian droplets [23, 33].

Furthermore, the effect of the walls is investigated for different *PL-N* systems in varying confinements (from 2R/H = 0.18 to 0.7). The tests include the exponential factors $n_d = 0.875$ and 1.125, while the capillary number is fixed at $Ca = 0.2$ to avoid non-ellipsoidal drops.

Figure (4.5) shows the deformation and the orientation angle as a function of the confinement ratio. The insets compare the results from the $PL\text{-}N/n_d = 1.125$ and the $N\text{-}N/\lambda = 0.3$ systems, shown with triangle magenta symbols. Complementarily, figure (C.1) in Appendix C plots all available data, i.e. the deformation and the orientation angles against the confinement at $Ca = 0.2$, from the *N-N* and *PL-N* systems.

In general, increasing confinement ratios lead to increasing deformation parameters and decreasing orientation angles. Similar to the findings in figure (4.4) the Newtonian droplet deforms the most, while it turns less than shear-thinning and more than shear-thickening droplets. More interestingly, power-law droplets with different exponents behave similarly under the same characterisation.

For example, both red lines in figure (4.5(a)), representing shear-thinning drops with $n_d = 0.75$ and $n_d = 0.875$, show a moderate inclination up to $2R/H$=0.4 and then a sharper trend. In addition, their orientation is weakly affected by the presence of the walls, as seen in figure (4.5(b)). Similarly, depicted by the blue lines, the deformation of shear-thickening droplets presents considerably less variations and lowest increment rate. Their orientation seems to be also mildly affected, but more than the shear-thinning cases.

Overall, the change in tumbling presents comparable decreasing levels for all the
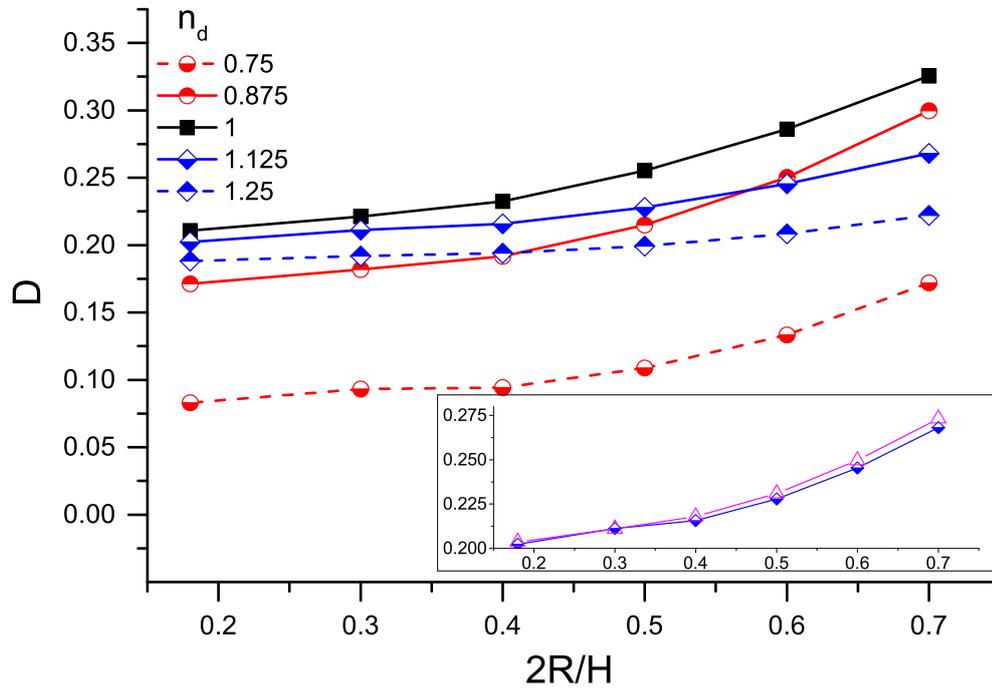
(a)
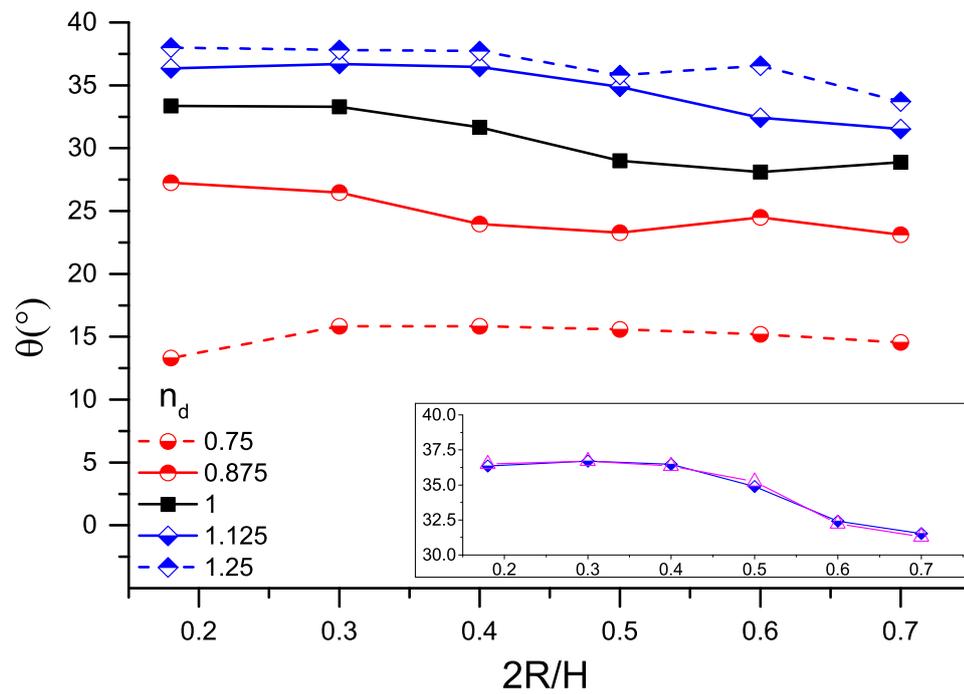
(b)

Figure 4.5: (a) Droplet deformation and (b) orientation angle as a function of the confinement ratio, $2R/H$, for various power-law exponents, n_d, at $Ca = 0.2$. Insets: comparison of droplet characteristics for $n_d = 1.125$ and the Newtonian droplet of $\lambda = 0.3$ (magenta - triangle).

exponents, approximately $8 - 15$ %, which translates to a difference between 1.2° and 5.21°. On the other hand, the deformation percentage change spans from 18 to 107 %. The percentage increase of the deformation and decrease of the orientation angle are reported in table (C.1) in Appendix C for each exponent. In conclusion, shear-thinning *PL-N* systems respond more to the presence of the walls compared with the shear-thickening. *Chapter* 3 draws the same conclusion for the high- and low- viscosity ratios *N-N* systems.

Finally, two almost equivalent systems are compared at $Ca = 0.2$ in confinement ratio $2R/H = 0.4$, in which case the magnitude of shear is $\dot{\gamma}_0 = 5 \times 10^{-5}$: the *N-N*$/\lambda = 0.3$ to the *PL-N*$/n_d = 1.125$. These systems are correlated through equation (4.2). Figure (4.6) compares the characteristics of these two systems. Almost identical results are observed for the power-law droplet with $n_d = 1.125$ and the Newtonian droplet with $\lambda = 0.3$. These droplets can be correlated through equation (4.2), as already discussed.

Figure (4.6(a)) shows that the shapes of the two droplets coincide at the $x - z$ middle plane. However, the relaxation parameter (or viscosity) inside the droplet differs. Figure (4.6(b)) plots τ along the $z-$ direction, in the middle of the droplet and at the position $x = 10$ (dashed lines) where the lowest τ value is observed. Furthermore, figures (4.6(c)) and (4.6(d)) contrast the viscosity and the velocity patterns for the Newtonian and the power-law droplet, respectively. All properties match except for the viscosity inside the droplets; the power-law droplet shows two minimum value regions. However, the viscosity of the power-law droplet is a result of the shear and does not alter the dynamics on the interface of the droplet once in the steady state. Therefore, the viscosity may not play a significant role in the evolution of the deformation, and thus a power-law droplet may behave identically to a Newtonian droplet of a specific corresponding viscosity.

This statement is true for ellipsoidal droplets in a steady, or transient state. However, it may not be the same for highly deformed non-ellipsoidal droplets.

The following section studies the breakup of power-law droplets, and also the correlation of *Power-law–* to *N-N* systems in the transient state.
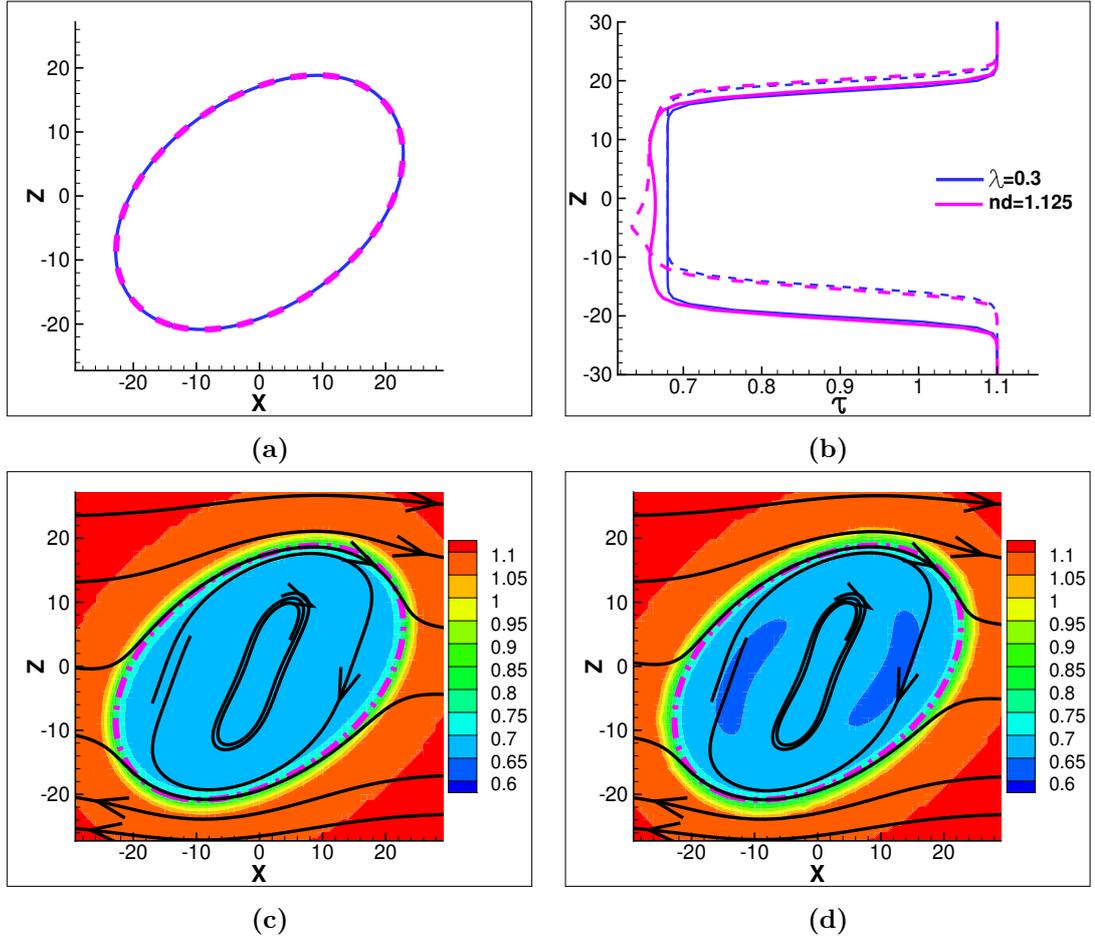
Figure 4.6: (a) Shapes of final deformed droplets and (b) relaxation parameter, τ, at $x = 0$ (solid) and $x = 10$ (dashed), for $\lambda = 0.3$ (blue) and $n_d = 1.125$ (magenta). Shapes of final deformed droplets (dashed-dotted magenta lines), relaxation parameter (see legend for contours), and streamlines for (c) N-$N.\lambda = 0.3$, and (d) PL-$N/n_d = 1.125$ systems, in the middle $x - z$ plane. 3D simulations of droplet deformation for $Ca = 0.2$, $2R/H = 0.4$.

4.3.3   Droplet Breakup

The previous sections examine the deformation in PL-N systems. This section evaluates the breakup process of power-law droplets. Again, the PL-N systems are compared to the equivalent N-N.

Simulations are performed in a domain with length of $400\,l.u.$ or more to avoid the computational artefacts regarding the high intensity shearing, as described in Section 2.4.1, *Chapter* 2. The considerable large length leads to high computational costs, hence here we consider a moderate confinement ratio, i.e. $2R/H = 0.37$, and a large confinement ratio , i.e. $2R/H = 0.7$.

The first tests include the N-$N/\lambda = 0.3$ and PL-$N/n_d = 1.125$ systems, where the capillary number, Ca, is 0.5. The confinement ratio $2R/H = 0.37$ is preferred in order to focus on the contribution of the power-law nature of the fluid and avoid significant effects from the wall. Notice that the Newtonian droplet undergoes a binary breakup in these conditions (see *Chapter* 3, figure (3.14)).

According to equation (4.2) the exponent $n_d = 1.125$ leads to the equivalent viscosity ratio $\lambda_{eq} \approx 0.30705$. Table (4.1) shows that the exponent to achieve an equivalent viscosity ratio $\lambda_{eq} = 0.3$ is $n_d \approx 1.2747$. Therefore, the system PL-$N/n_d = 1.2747$ is also included in this comparison. Hence, three systems are evaluated at $Ca = 0.5$, $2R/H = 0.37$:

- N-$N/\lambda = 0.3$, depicted with black lines in figures (4.7) and (4.8),

- PL-$N/n_d = 1.125$, with blue lines, and

- PL-$N/n_d \approx 1.127$, with red lines.

Figure (4.7) shows the evolution of the droplets at three time instants: $t^* = 1$, 5, 15, where $t^* = \dot{\gamma}_0 t$ and t is the time step. At the first time instant the droplets obtain practically an identical ellipsoidal shape. This finding is similar to the one discussed in the previous section regarding the steady state (see figure (4.6(a))). Here, it is shown that the effects of the viscosity adaptation to the shear rate are not consequential to the behaviour of the droplet also in the transient state. At a later time instant, i.e. $t^* = 5$,
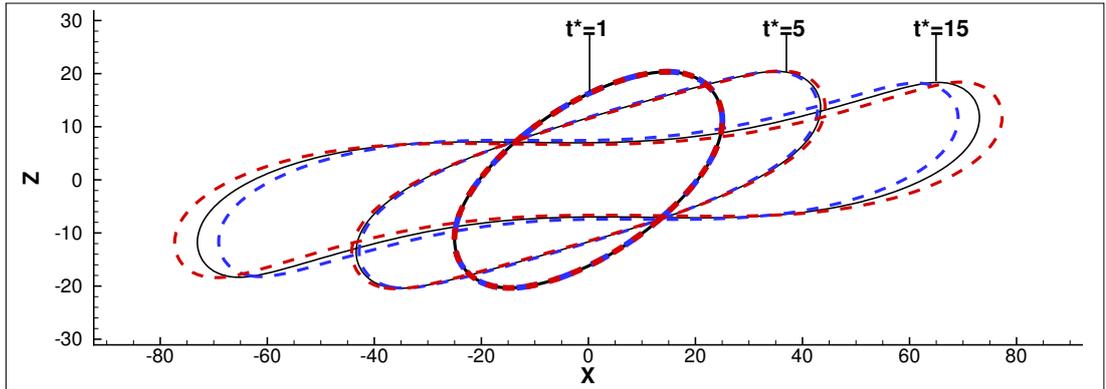
Figure 4.7: Transient droplet shapes, in the $x - z$ middle plane, in systems N-$N/\lambda = 0.3$ (solid-black), PL-$N/n_d = 1.125$ (dashed-blue), and PL-$N/n_d \approx 1.127$ (dashed-red lines), at time instants $t^* = 1$, 5, 15.

the shapes of each droplet are slightly different and they deviate from the ellipsoidal. Specifically, in $PL\text{-}N/n_d = 1.125$ the droplet has elongated less compared to the one in $N\text{-}N/\lambda = 0.3$, while the opposite is observed in $PL\text{-}N/n_d \approx 1.127$. Finally, at $t^* = 15$ a long neck and different oriented curvatures have been formed in all systems. The shapes of the droplets differ considerably more than those in time instant $t^* = 5$.

The evolved stresses at the tips and the neck of the droplet can evaluate the elongation and thinning of each droplet, i.e. how much the two edges are "pulled" and the neck is "compressed". Note that the tip is located at the rightmost position where the elongational component ($\partial u_z/\partial z$ as reported in [55]) is 0, marked for each droplet in figures (C.2) and (C.3) in Appendix C, and the neck at the centre ($x = 0$). Table (4.2) shows the magnitude of the T_{xx}, T_{xz} and T_{zz} stresses at the described locations in the $x - z$ middle plane at the times instants $t^* = 5$ and 15.

The droplet in $PL\text{-}N/n_d = 1.125$ presents the lowest stress values at the tip, explaining the smallest elongation at both $t^* = 5$ and 15. In addition, the same droplet experiences the lowest absolute T_{zz} values at the neck. Hence, this droplet elongates the least and has the thickest neck. Contrariwise, at $t^* = 5$ the droplet in $PL\text{-}N/n_d \approx 1.127$ exhibits a slightly more elongated shape, which is due to the larger stresses on its surface comparing to respective droplet in $N\text{-}N/\lambda = 0.3$. The effect of the larger stress magnitude builds up and thus the specific droplet stretches even more at $t^* = 15$. Additionally, due to the highest absolute T_{zz} values at the neck, this droplet also has the thinnest neck.

Note that $n_d = 1.125$ leads to a higher equivalent viscosity ratio than $\lambda = 0.3$ at

Table 4.2: Stresses at the tip and the neck at time instants $t^* = 5$ and 15 of the respective droplets in systems: *i.* $N\text{-}N/\lambda = 0.3$, *ii.* $PL\text{-}N/n_d = 1.125$, and *iii.* $PL\text{-}N/n_d \approx 1.127$. Units are in lattice units E-06.

Location	System	$t^* = 5$			$t^* = 15$		
		T_{xx}	T_{xz}	T_{zz}	T_{xx}	T_{xz}	T_{zz}
Tip	*i.*	12.2	34.9	0.824	11.84	34.25	0.91
	ii.	11.7	32.8	0.635	11.75	33.03	0.65
	iii.	12.7	36.7	0.824	12.48	35.72	0.766
Neck	*i.*	-2.33	12.2	-0.135	1.08	12.84	-0.104
	ii.	-2.61	11.0	-0.093	0.72	11.91	-0.0135
	iii.	-2.35	12.4	-0.1246	1.21	13.35	-0.2233

$Ca = 0.5$ (see table (C.1)). Nevertheless, the viscosity inside the power-law droplet of system PL-$N/n_d = 1.125$ is actually smaller than in the respective N-$N/\lambda = 0.3$ droplet. In Appendix C, each droplet in the aforementioned N-N and PL-N systems is illustrated individually (figures (C.2) and (C.3)), and the viscosity along the $z-$ direction is plotted at the middle ($x = 0$), for time instants $t^* = 5$ and 15.

The continuous exposure to a strong shear leads to highly deformed droplets. Figure (4.8) illustrates the evolution sequence of each droplet close to the breakup point for each system. At a specific time instant the elongation ceases almost completely, but due to the ongoing decreasing neck width a pinch-off point is created. Finally, binary breakup occurs at a time instant which is referred to as critical breakup time and noted as t^*_{cr}. The critical breakup times for each system are:

- $23 < t^*_{cr} < 24$ for N-$N/\lambda = 0.3$,

- $24 < t^*_{cr} < 25$ for PL-$N/n_d = 1.125$, and

- $28 < t^*_{cr} < 29$ for PL-$N/n_d \approx 1.127$.

Both PL-N systems take longer to breakup than the N-N system. Following the previous discussion, the power-law droplet in the system PL-$N/n_d = 1.125$ experiences smaller stresses at the neck area. Therefore its neck "pinches-off" at a later time point comparing to the Newtonian droplet.

On the other hand, even though the power-law droplet in PL-$N/n_d \approx 1.127$ experiences greater stresses than the Newtonian one at $t^* = 15$ (see table (4.2)) the neck narrows at a very slow rate up to $t^* = 26$. Figure (C.5), in Appendix C, shows the negligible change in the droplet shape during the time period $t^* = 23 - 26$. A possible explanation is that this specific droplet has the ability to respond to the neck narrowing by increasing the viscosity locally and thus oppose to the local deformation.

To support this statement two droplets are compared: in system N-$N/\lambda = 0.3$ at t^*=21 and in PL-$N/n_d \approx 1.127$ at $t^* = 24$. Figures (4.9(a)) and (4.9(b)) illustrate the droplets shapes and the viscosity contours in lattice units. Clearly, the viscosity of the Newtonian droplet is constant. On the other hand, the power-law droplets exhibits two low viscosity areas close to the tips and increased viscosity in the middle. Additionally, figure (4.9(c)) plots the viscosity along the height at $x = 0$ and marks the position of
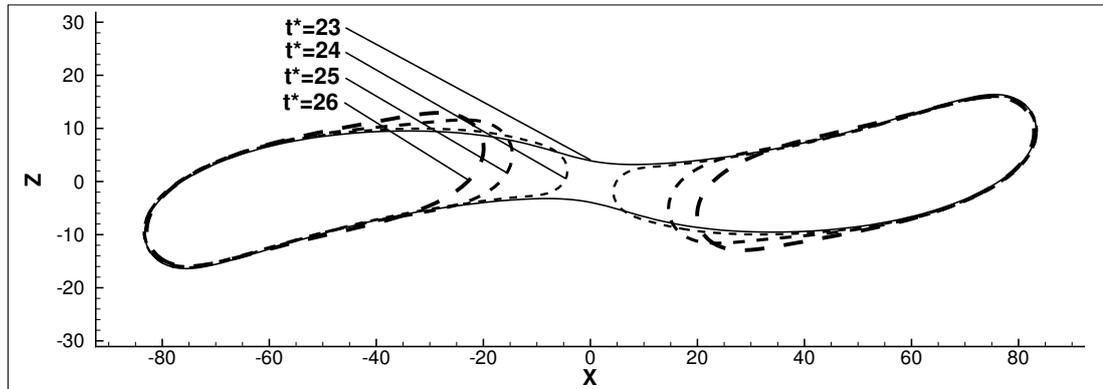
(a)
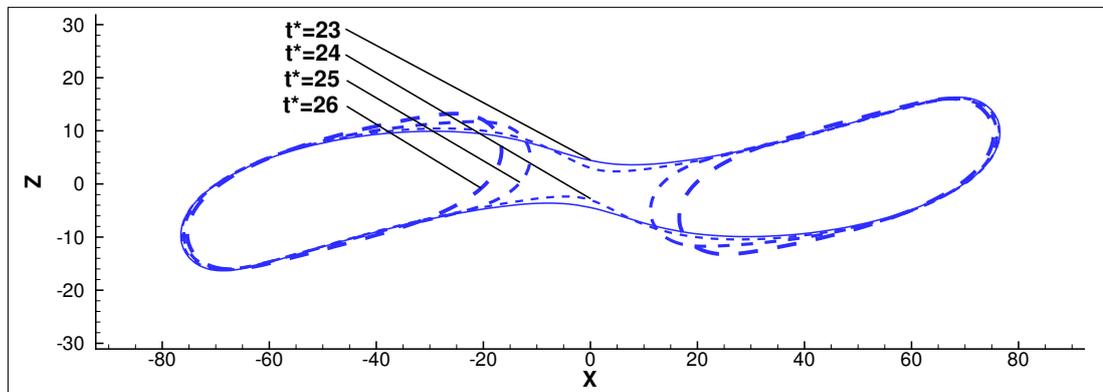
(b)
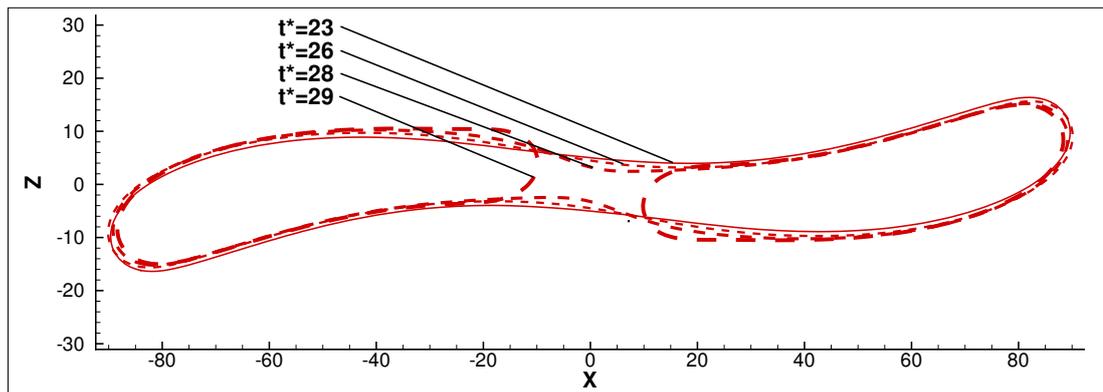
(c)

Figure 4.8: Transient droplet shapes close to the critical breakup time, in the $x-z$ middle plane, in systems (a) N-$N/\lambda = 0.3$, (b) PL-$N/n_d = 1.125$, and (c) PL-$N/n_d \approx 1.127$.
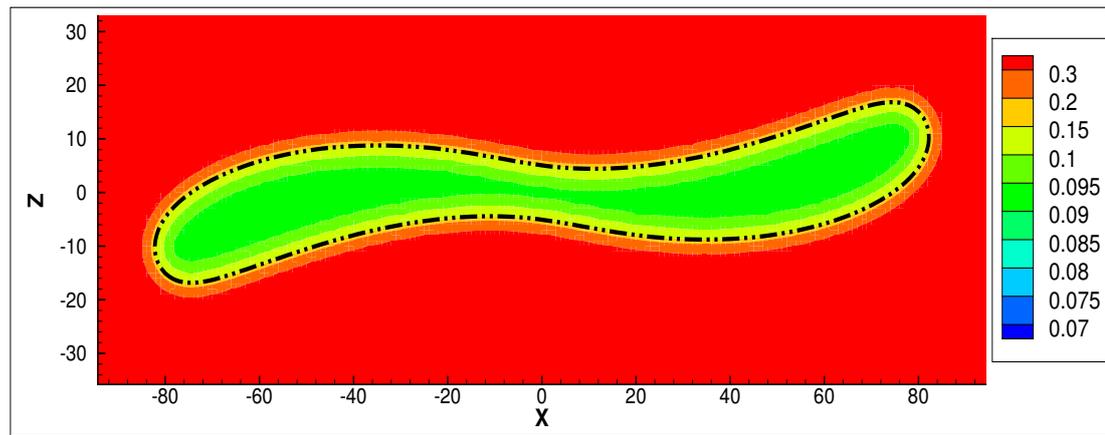
(a)
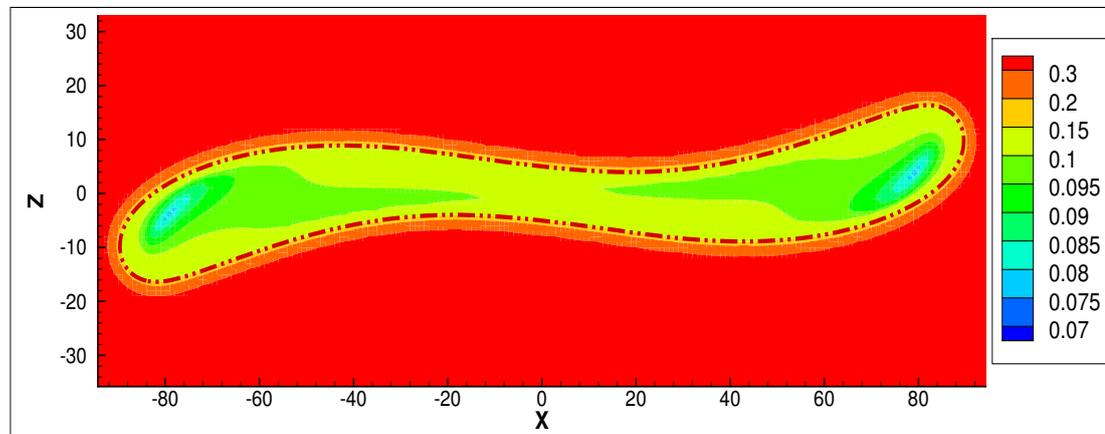
(b)
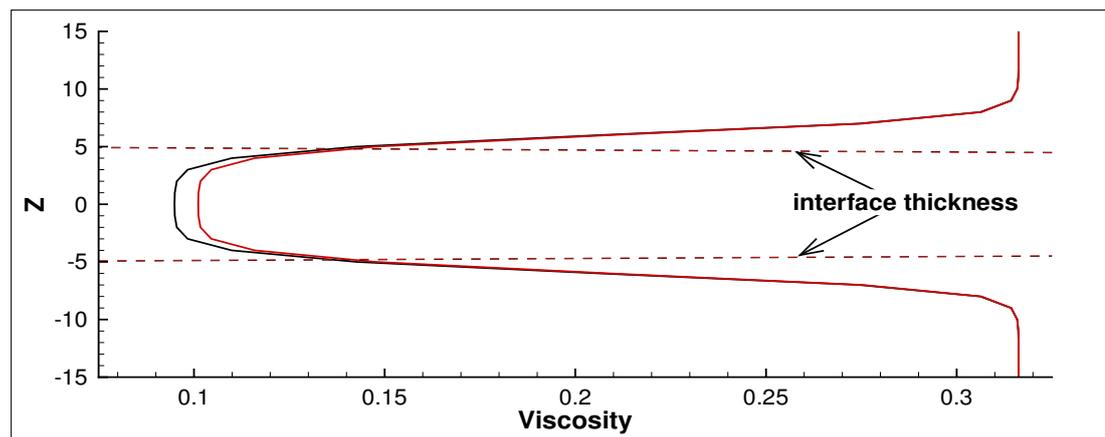
(c) Viscosity and interface position.

Figure 4.9: Shapes of deformed dropelts (dashed-dotted lines) and viscosities (see legend for contours in $l.u.$), in the $x - z$ middle plane, for two characteristic systems and time instants: (a) $N\text{-}N/\lambda = 0.3$ at $t^* = 21$, (b) $PL\text{-}N/n_d \approx 1.127$ at $t^* = 24$. (c) Viscosity contrast along height, z, and interface thickness at the centre ($x = 0$), for the two droplets in (a) black, $N\text{-}N/\lambda = 0.3$ - $t^* = 21$, and (b) red $PL\text{-}N/n_d \approx 1.127$ - $t^* = 24$.

Table 4.3: Stresses at the neck and percentage increment since $t^* = 15$ of the respective droplet in systems: *i.* system $N\text{-}N/\lambda = 0.3$ at $t^* = 21$, and *ii.* $PL\text{-}N/n_d \approx 1.127$ at $t^* = 24$. Units are in lattice units E-06.

System	T_{xx}	↗ %	T_{xz}	↗ %	T_{zz}	↗ %
i.	3.67	240	13.9	8.2	-3.56	3323.1
ii.	2.54	110	13.82	3.5	-3.99	1686.8

the interfaces for both droplets. The necks at this location have the same width in both systems, which is the reason we choose to compare this pair of droplets at the specific time instants, but the viscosity is greater by 6.58% for the power-law droplet. Moreover, table (4.3) contrasts the stresses at the neck and the percentage increase since $t^* = 15$. The increment rate of stresses on the neck of the Newtonian droplet is twice as large as the respective power-law droplet of $n_d \approx 1.127$. The slowly build-up of stress and the enhanced viscosity lead to a higher t^*_{cr}.

Furthermore, the behaviour of a Newtonian droplet with viscosity ratio $\lambda = 3$ is compared to the behaviour of a shear-thinning droplet characterised by a power-law index $n_d \approx 0.8837$, which leads to the specific equivalent viscosity ratio $\lambda_{eq} = 3$. Henceforth, these systems are referred to as '$N\text{-}N/\lambda = 3$' and '$PL\text{-}N/n_d \approx 0.8837$', respectively. The droplet in the first system breaks at $Ca = 0.5$ in a highly confined domain of $2R/H = 0.7$. Hence, these values are set in the simulations.

Figure (4.10) shows the evolution of these droplets at various time instants, with the black lines for the Newtonian and the red lines for the power-law droplet. At the first time instant $t^* = 1$ they both obtain an identical shape, similarly to the case
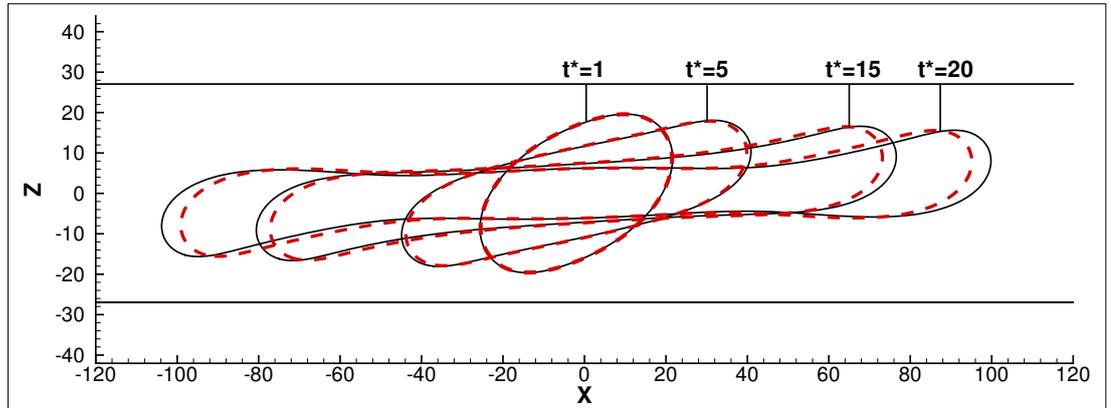
Figure 4.10: Transient droplet shapes, in the $x - z$ middle plane, in systems $N\text{-}N/\lambda = 3$ (black-solid lines) and $PL\text{-}N/n_d \approx 0.8837$ (red-dashed lines), at time instants $t^* = 1, 5, 15, 20$.

of low-viscous and shear-thickening droplets in figure (4.7). At later times they both elongate extensively. Gradually, the shear-thinning droplet elongates less due to the lower normal stresses that are exerted in the $x-$ direction on its tips compared to the Newtonian drop. The stresses at this location, are presented in table (C.2) in Appendix C.

Figures (4.11(a)) and (4.11(b)) illustrate the evolution sequence of the droplets close to the breakup point. Contrary to the previous observations regarding the low-viscous and shear-thinning droplets, the elongation does not cease due to the effects from the high proximity of the walls. Additionally, two regions between the centre and the two edges of the drop become very thin at $t^* = 27$. These regions produce two pinch-off points at later times leading to ternary breakups.
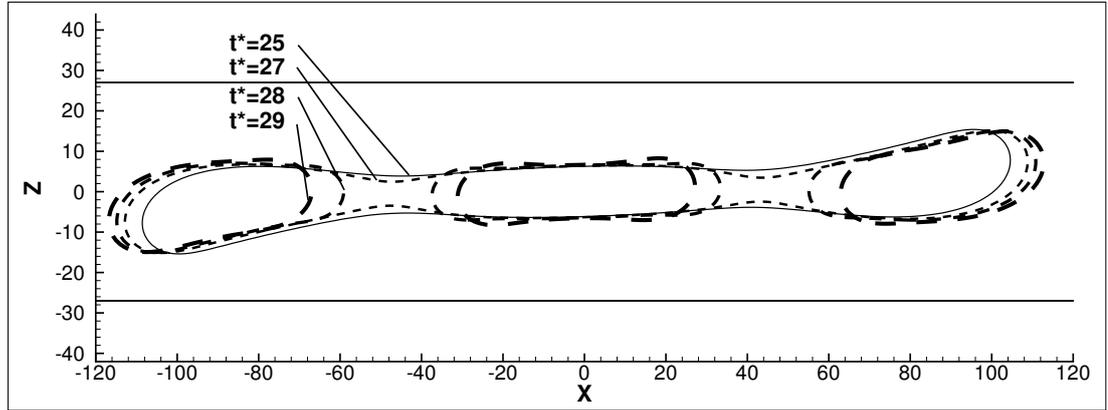
(a)
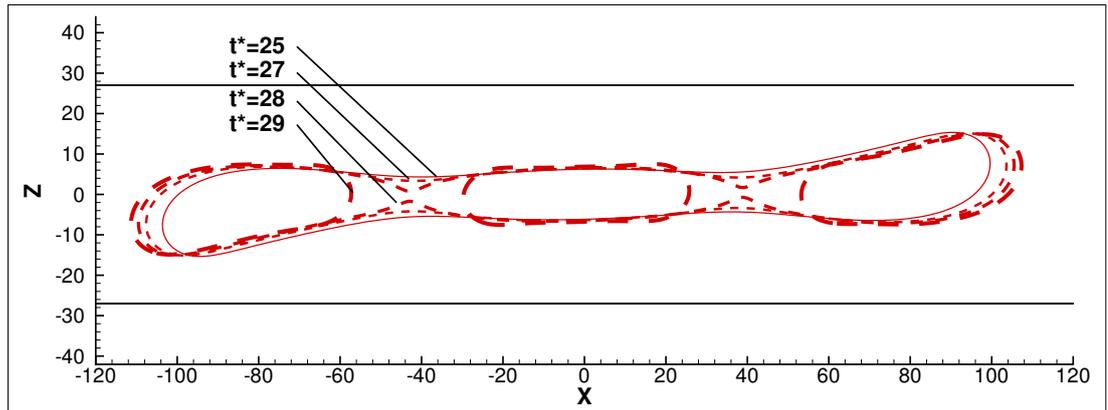
(b)

Figure 4.11: Transient droplet shapes close to the critical breakup time, in the $x - z$ middle plane, in systems (a) N-$N/\lambda = 3$, and (b) PL-$N/n_d \approx 0.8837$.

Table 4.4: Stresses (in *l.u.*) at the neck for N-$N/\lambda = 3$ ($x = 44$) and PL-$N/n_d = 0.8837$ ($x = 38.35$) at time instant $t^* = 27$ [E-06], and their absolute percentage difference. The last column shows the thickness (in *l.u.*).

Case	T_{xx}	T_{xz}	T_{zz}	Thickness
N-$N/\lambda = 3$	15.68	30.02	-6.221	6
PL-$N/n_d = 0.8837$	8.93	30.97	-4.1523	7
Difference	75.6 %	3 %	49.9 %	1

More specific, table (4.4) presents the stresses on these regions along with their absolute percentage differences and their thickness. The Newtonian droplet cannot resist to the further narrowing at the specific regions and presents the pinch-off points at the next instant. On the other hand, the shear-thinning droplet experiences lower T_{xx} stresses by 75.6 % and also almost half of the T_{zz} stresses comparing to its counter Newtonian droplet. Thus, the relative weaker "stretching" and "compressing" on these regions delay the breakup until $t_{cr}^* > 28$, but due to the extremely thin necks (less than 3 lattices) it finally bursts.

As a general comment, the contrast of N-N to PL-N systems demonstrates that the initial estimation that a non-Newtonian droplet would behave as a Newtonian under the same shear conditions is incorrect when the droplets are not ellipsoidal.

4.4   Conclusions

This *Chapter* studies the behaviour of power-law droplets confined in a Newtonian matrix fluid.

The initial 2D tests show that power-law–Newtonian systems of $n_d = 0.5$ and $n_d = 0.6$ behave identically. The investigation shows that although the relaxation parameters differ significantly along the droplet for these cases, the shear has the same impact. Hence, the lattice BGK model is unsuitable for the investigation in such low power-law exponents.

Further tests on increasing power-law exponents, i.e. $n_d = 0.6 - 1.4$ showed that the Newtonian droplet deforms the most, while the orientation angle increases monotonously. Additionally, each type of droplet, i.e. shear-thinning/thickening, behaves differently depending on the power-law viscosity ratio ($\lambda_{(PL)}$). The deformation and orientation angle of a shear-thinning droplet decrease steeply with increasing $\lambda_{(PL)}$,

contrary to the shear-thickening droplet whose deformation increases and while its orientation decreases slightly.

The impacts of the shear rate intensity and the approximation of the walls are evaluated 3D simulations in a similar fashion to those described in *Chapter* 3. It was shown that, the shear-thinning droplets produce similar or even identical characteristics as high-viscous Newtonian droplets, and they are affected more significantly when compared to the shear-thickening. On the other hand, the shear-thickening droplets, which behave similar to low-viscous Newtonian drops are weakly affected.

In particularly, when the droplets obtain an ellipsoidal shape, the power-law–Newtonian systems exhibit similar characteristics to the Newtonian–Newtonian ones, even though the viscosities inside the droplets clearly differ. This feature is observed for both the steady state at low capillary numbers ($Ca \leq 0.3$), and the transient state at early times at a higher capillary numbers ($Ca = 0.5$). Therefore, in these cases the dominant factor for the overall behaviour are the stresses exerted by the matrix fluid to the droplet.

However, upon the transition from the ellipsoidal to a more elongated sigmoidal shapes, the same droplets differ gradually in their shapes and their overall behaviour. These variations and the different breakup times are correlated to the viscosities and the stresses observations at the characteristic locations, e.g. the tip and the neck of a droplet.

In summary, the breakup of a Newtonian droplet occurs earlier than the corresponding power-law one. Interestingly, the droplet in the low-viscous or the shear-thickening systems elongates to a specific length prior to the "pinch-off" event. Moreover, the stresses in characteristic positions on the droplet surface, i.e. the neck and the tips, evolve differently even with slight variation of the power-law exponent. Regarding the high-viscous Newtonian system and its shear-thinning counterpart, the droplets deform more and continue to elongate while the breakup points are forming, due to the high wall confinement ($2R/H = 0.7$), producing three daughter droplets.

Chapter 5

Conclusions and Future Work

5.1 Conclusions

This work has addressed computationally the problem of a droplet subjected to a simple shear flow, where inertia plays an insignificant role ($Re = 0.1$). Relevant theoretical, experimental and computational studies were discussed, providing the background and the state-of-the-art of this research topic. The numerical method we developed to solve the flow and interfacial dynamics is the lattice Boltzmann colour-gradient method which implements a CSF formulation at the interface to account for the surface tension effects.

Our interest was focussed on the interplay of three characteristics: the magnitude of the shear rate which was adjusted by the velocity of the walls and translated by the capillary number (Ca); the effects of the wall vicinity to the droplet expressed by the confinement ratio ($2R/H$); and the relation between the viscosities of the matrix and the droplet fluids related either by the viscosity ratio (λ), or by the power-law exponent of the matrix (n_c) or the droplet fluids (n_d).

After the validation of the method, we investigated the sheared droplet in three configurations depending on the viscosity modelling of the dispersed and bounding fluids. The range of the parameters examined was broad to cover both steady and breakup regimes:

- capillary numbers: $Ca = 0.1 - 0.65$,

- confinement ratios: $2R/H = 0.18 - 0.8$,

- viscosity ratios $\lambda = 0.3 - 5$,

- power-law exponents for matrix (n_c) and droplet fluids (n_d): $n = 0.5 - 1.5$.

The behaviour of the droplet was evaluated with respect to its deformation, orientation and breakup, while the evaluations of the pressure, velocity, viscosity and stresses contributed to the understanding of the findings. The overall conclusions are that the deformation increases and the orientation angle decreases with increasing Ca and $2R/H$ for all droplets.

Regarding the Newtonian droplets suspended in a Newtonian matrix fluid, the most interesting finding is that the equi-viscous droplet deforms the most at every confinement ratio tested, at $Ca = 0.2$. However, no conclusive argument can be stated regarding which droplets deform the most between low and high viscosity ratios. The results suggest that in low confinements droplets of low viscosity deform more. Nevertheless, the deformation trend of the high-viscous droplets alters significantly in confinement ratios of $2R/H \geq 0.4$ and their elongation is favoured over the low-viscous ones. This behaviour is supported by the analyses of the flow fields, and stresses on the surfaces which show that the interplay between droplet and carrier fluid becomes more intense upon the increment of the viscosity ratio. Additionally, less viscous droplets turn less to the flow (present higher θ values) and they are also more prone to change their orientation upon increasing the confinement.

Furthermore, a Newtonian droplet deforms less and also tumbles less to the direction of the flow when sheared in a shear-thinning environment and more in a shear-thickening one. The increasing confinement shows to have a uniform effect in the increment of the deformation; the stresses involved show the same patterns but with increasing magnitudes. Moreover, the degree of confinement affects significantly more the orientation of the droplet when the matrix fluid is shear-thickening comparing to the shear-thinning.

Complementary, our investigations included the breakup procedure. The critical capillary number (Ca_{cr}) differs for droplets of different viscosities and depends on the confinement. It is shown, consistent with previous findings, that a low viscous droplet requires higher shear intensity conditions to break with increasing confinement, while the opposite is found for high viscous droplets. The equi-viscous Newtonian droplets depend weakly on the confinement, and also show lower Ca_{cr} when sheared in a power-

law fluid.

Meanwhile, the power-law droplet was simulated in a wide range of parameters. Our simulations showed that the lattice BGK model has an application limit with respect to the power-law exponent. Furthermore, power-law and Newtonian droplets are correlated, and hence the findings match to those of the *equivalent* low- and high-viscous droplets regarding deformation, orientation and critical capillary numbers.

However, during the breakup process the shapes of the *equivalent* droplets differ even with minor differences in the power-law index and show different breakup times; in all cases power-law droplet breakup at later time instants. The elongation and neck thinning are correlated with the stresses in characteristic droplet locations, hence revealing the reasons behind these differences. Ultimately, a Newtonian droplet of a certain viscosity can reproduce the effects of a power-law one, as long as the droplet shapes are close to the ellipsoidal form. Therefore equivalent Newtonian droplets cannot be utilised in applications which involve "pinch-off" events.

5.2 Future Work

The extension of the present work can include:

- the investigation of the power-law droplet behaviour in power-law matrix fluids. Although in the steady state regime the power-law droplet is expected to behave like a Newtonian one, the breakup still presents interest due to the capillary effects and the strong variation of the velocity gradients. An approach could be similar to the one described in Section 2.4. The equivalent constant Newtonian viscosities can be calculated from the dimensionless numbers and used as an input for the consistency indices, while the power-law exponents can be tuned for each fluid individually.

- the implementation of Generalized Newtonian Fluids (GNF) expressions; many numerical works report to implement the Carreau model [40, 58, 155, 156].

- the investigation of dense emulsions by

  - introducing more droplets and model their interaction as in [91], or

– by implementing the sliding bi-periodic frame described in [157].

- simulations from simple to more complex geometries for future implementation, e.g. in T-junction, cross-flow and porous-media configurations. The contact line dynamics can be addressed by the model proposed in [94].

- the implementation of the MRT instead of the BGK collision operator. This extension will allow for simulations in a wider range of power-law exponents than those considered in this work.

- the study of deformation and breakup in oscillatory shear flows following the work in [158].

References

[1] H. Song, D. L. Chen and R. F. Ismagilov. Reactions in droplets in microfluidic channels. *Angewandte Chemie International Edition*, 45(44), 7336–7356, 2006.

[2] P. Day, A. Manz and Y. Zhang. *Microdroplet Technology Principles and Emerging Appplications in Biology and Chemistry*. Springer, 2012.

[3] C. D. McAuliffe. Oil-in-water emulsions and their flow properties in porous media. *Journal of Petroleum Technology*, 25, 727–733, 1973.

[4] J. Higdon. Multiphase flow in porous media. *Journal of Fluid Mechanics*, 730, 1–4, 2013.

[5] T. Fu, Y. Ma and H. Z. Li. Breakup dynamics of slender droplet formation in shear-thinning fluids in flow-focusing devices. *Chemical Engineering Science*, 144, 75–86, 2016.

[6] Y. Ren, Z. Liu and H. C. Shum. Breakup dynamics and dripping-to-jetting transition in a Newtonian/shear-thinning multiphase microsystem. *Lab on a Chip*, 15, 121–134, 2015.

[7] F. Boyer, E. Sandoval-Nava, J. H. Snoeijer, J. F. Dijksman and D. Lohse. Drop impact of shear thickening liquids. *Physical Review Fluids*, 1, 013901, 2016.

[8] J. S. Hong and J. Cooper-White. Drop formation of carbopol dispersions displaying yield stress, shear thinning and elastic properties in a flow-focusing microfluidic channel. *Korea-Australia Rheology Journal*, 21(4), 269–280, 2009.

[9] S. Guido and F. Greco. Dynamics of a liquid drop in a flowing immiscible liquid. *Rheology Reviews*, 99–142, 2004.

[10] F. Gauthier, H. L. Goldsmith and S. G. Mason. Particle motions in non-Newtonian media. *Rheologica Acta*, 10(3), 344–364, 1971.

[11] R. W. Flumerfelt. Drop breakup in simple shear fields of viscoleastic fluids. *Industrial & Engineering Chemistry Fundamentals*, 11(3), 312–318, 1972.

[12] J. J. Elmendorp. A study on polymer blending microrheology. *Polymer Engineering & Science*, 26(6), 418–426, 1986.

[13] R. de Brujin. *Deformation and breakup of drops in simple shear flows*. Ph.D. Thesis, Technische University of Eindhoven, Nederlands, 1991.

[14] M. Boufarguine, F. Renou, T. Nicolai and L. Benyahia. Droplet deformation of a strongly shear thinning dense suspension of polymeric micelles. *Rheologica Acta*, 49(6), 647–655, 2010.

[15] M. Minale. A phenomenological model for wall effects on the deformation of an ellipsoidal drop in viscous flow. *Rheologica Acta*, 47, 667–675, 2008.

[16] A. Gupta and M. Sbragaglia. Deformation and breakup of viscoelastic droplets in confined shear flow. *Physical Review E*, 90, 023305, 2014.

[17] R. G. Larson. *The structure and rheology of complex fluids*. New York , Oxford University Press, 1999.

[18] F. A. Morrison. *Understanding rheology*. Oxford University Press, 2001.

[19] J. M. Rallison. A numerical study of the deformation and burst of a viscous drop in general shear flows. *Journal of Fluid Mechanics*, 109, 465–482, 1981.

[20] A. Vananroye, P. Van Puyvelde and P. Moldenaers. Effect of confinement on the steady-state behavior of single droplets during shear flow. *Journal of Rheology*, 51(1), 139–153, 2007.

[21] M. Giraldo, H. Power and W. F. Flórez. Numerical simulation of the motion and deformation of a non-Newtonian shear-thinning drop suspended in a Newtonian circular couette flow using DR-BEM. *Engineering Analysis with Boundary Elements*, 33(1), 93–104, 2009.

[22] S. Guido and M. Villone. Three-dimensional shape of a drop under simple shear flow. *Journal of Rheology*, 42, 395, 1998.

[23] P. J. A. Janssen, A. Vananroye, P. V. Puyvelde, P. Moldenaers and P. D. Anderson. Generalized behavior of the breakup of viscous drops in confinements. *Journal of Rheology*, 54(5), 1047–1060, 2010.

[24] F. Rumscheidt and S. Mason. Particle motions in sheared suspensions XII. Deformation and burst of fluid drops in shear and hyperbolic flow. *Journal of Colloid Science*, 16(3), 238–261, 1961.

[25] P. V. Puyvelde, A. Vananroye, R. Cardinaels and P. Moldenaers. Review on morphology development of immiscible blends in confined shear flow. *Physics of Fluids*, 20, 013101, 2008.

[26] G. I. Taylor. The formation of emulsions in definable fields of flow. *Proceedings of the Royal Society of London A: Mathematical, Physical and Engineering Sciences*, 146(858), 501–523, 1934.

[27] M. Shapira and S. Haber. Low Reynolds number motion of a droplet in shear flow including wall effects. *International Journal of Multiphase Flow* 16(2), 305–321, 1990.

[28] C. E. Chaffey and H. Brenner. A second-order theory for shear deformation of drops. *Journal of Colloid and Interface Science*, 24(2), 258–269, 1967.

[29] F. Greco. Second-order theory for the deformation of a Newtonian drop in a stationary flow field. *Physics of Fluids*, 14(3), 946–954, 2002.

[30] P. Maffettone and M. Minale. Equation of change for ellipsoidal drops in viscous flow. *Journal of Non-Newtonian Fluid Mechanics, 78, 227–241*, 1998.

[31] V. Sibillo, G. Pasquariello, M. Simeone, V. Cristini and S. Guido. Drop deformation in microconfined shear flow. *Physical Review Letters* 97(5), 054502, 2006.

[32] M. Minale. Models for the deformation of a single ellipsoidal drop: a review. *Rheologica Acta*, 49(8), 789–806, 2010.

[33] A. Vananroye, P. V. Puyvelde and P. Moldenaers. Effect of confinement on droplet breakup in sheared emulsions. *Langmuir*, 22(9), 3972–3974, 2006.

[34] H. Zhou and C. Pozrikidis. The flow of suspensions in channels: Single files of drops. *Physics of Fluids A*, 5(2), 311–324, 1993.

[35] M. R. Kennedy, C. Pozrikidis and R. Skalak. Motion and deformation of liquid drops, and the rheology of dilute emulsions in simple shear flow. *Computers & Fluids*, 23(2), 251–278, 1994.

[36] K. S. Sheth and C. Pozrikidis. Effects of inertia on the deformation of liquid drops in simple shear flow. *Computers & Fluids*, 24(2), 101–119, 1995.

[37] P. J. A. Janssen and P. D. Anderson. Boundary-integral method for drop deformation between parallel plates. *Physics of Fluids*, 19, 043602, 2007.

[38] A. Vananroye, P. J. A. Janssen, P. D. Anderson, P. Van Puyvelde and P. Moldenaers. Microconfined equiviscous droplet deformation: Comparison of experimental and numerical results. *Physics of Fluids*, 20(1), 013101, 2008.

[39] P. Janssen and P. Anderson. A boundary-integral model for drop deformation between two parallel plates with non-unit viscosity ratio drops. *Journal of Computational Physics*, 227(20), 8807–8819, 2008.

[40] R. E. Khayat. A boundary-only approach to the deformation of a shear-thinning drop in extensional Newtonian flow. *International Journal for Numerical Methods in Fluids*, 33(4), 559–581, 2000.

[41] M. Giraldo, H. Power and W. F. Flórez. Mobility of a viscous Newtonian drop in shear Newtonian flow. *International Journal of Dynamics of Fluids*, 3(2), 109–132, 2007.

[42] M. Giraldo, H. Power and W. F. Flórez. Mobility of shear thinning viscous drops in a shear Newtonian carrying flow using DR-BEM. *International Journal for Numerical Methods in Fluids*, 59(12), 1321–1349, 2009.

[43] I. Smagin, M. Pathak, O. M. Lavrenteva and A. Nir. Motion and shape of an axisymmetric viscoplastic drop slowly falling through a viscous fluid. *Rheologica Acta*, 50(4), 361–374, 2010.

[44] E. Toose, B. Geurts and J. Kuerten. A boundary integral method for two-dimensional (non)-Newtonian drops in slow viscous flow. *Journal of Non-Newtonian Fluid Mechanics*, 60(2–3), 129 – 154, 1995.

[45] P. Janssen and P. Anderson. Surfactant-covered drops between parallel plates. *Chemical Engineering Research and Design*, 86(12), 1388 – 1396, 2008. International Symposium on Mixing in Industrial Processes.

[46] C. Coulliette and C. Pozrikidis. Motion of an array of drops through a cylindrical tube. *Journal of Fluid Mechanics*, 358, 1–28, 1998.

[47] N. Boruah and P. Dimitrakopoulos. Motion and deformation of a droplet in a microfluidic cross-junction. *Journal of Colloid and Interface Science*, 453, 216–225, 2015.

[48] F. R. Cunha, M. H. P. Almeida and M. Loewenberg. Direct numerical simulations of emulsion flows. *Journal of the Brazilian Society of Mechanical Sciences and Engineering*, 25, 30–40, 2003.

[49] S. Kwak and C. Pozrikidis. Adaptive triangulation of evolving, closed, or open surfaces by the advancing-front method. *Journal of Computational Physics*, 145(1), 61–88, 1998.

[50] V. Cristini, J. Blawzdziewics and M. Loewenberg. An adaptive mesh algortihm for evolving surfaces: Simulations of drop breakup and coalescence. *Journal of Computational Physics*, 168, 445–463, 2001.

[51] I. B. Bazhlekov, P. D. Anderson and H. E. H. Meijer. Nonsingular boundary integral method for deformable drops in viscous flows. *Physics of Fluids*, 16(4), 1064–1081, 2004.

[52] J. Li, Y. Y. Renardy and M. Renardy. Numerical simulation of breakup of a

viscous drop in simple shear flow through a volume–of–fluid method. *Physics of Fluids*, 12(2), 269–282, 2000.

[53] Y. Y. Renardy and V. Cristini. Scalings for fragments produced from drop breakup in shear flow with inertia. *Physics of Fluids*, 13(8), 2161–2164, 2001.

[54] Y. Y. Renardy and V. Cristini. Effect of inertia on drop breakup under shear. *Physics of Fluids*, 13(1), 7–13, 2001.

[55] Y. Renardy. The effects of confinement and inertia on the production of droplets. *Rheologica Acta*, 46(4), 521–529, 2007.

[56] Y. Renardy and M. Renardy. Prost: a parabolic reconstruction of surface tension for the volume-of-fluid method. *Journal of Computational Physics*, 183(2), 400–421, 2002.

[57] D. Khismatullin, Y. Renardy and V. Cristini. Inertia–induced breakup of highly viscous drops subjected to simple shear. *Physics of Fluids*, 15(5), 1351–1354, 2003.

[58] D. Harvie, M. Davidson, J. Cooper-White and M. Rudman. A parametric study of droplet deformation through a microfluidic contraction: Shear thinning liquids. *International Journal of Multiphase Flow*, 33(5), 545–556, 2007.

[59] J. Li and Y. Y. Renardy. Shear-induced rupturing of a viscous drop in a Bingham liquid. *Journal of Non-Newtonian Fluid Mechanics*, 95(2–3), 235–251, 2000.

[60] A. Potapov, R. Spivak, O. M. Lavrenteva and A. Nir. Motion and deformation of drops in Bingham fluid. *Industrial & Engineering Chemistry Research*, 45(21), 6985–6995, 2006.

[61] T. Chinyoka, Y. Renardy, M. Renardy and D. Khismatullin. Two-dimensional study of drop deformation under simple shear for Oldroyd-B liquids. *Journal of Non-Newtonian Fluid Mechanics*, 130(1), 45–56, 2005.

[62] K. Verhulst, R. Cardinaels, P. Moldenaers, S. Afkhami and Y. Renardy. Influence of viscoelasticity on drop deformation and orientation in shear flow. Part 2: Dynamics. *Journal of Non-Newtonian Fluid Mechanics*, 156(1), 44–57, 2009.

[63] Y. Y. Renardy, M. Renardy and V. Cristini. A new volume-of-fluid formulation for surfactants and simulations of drop deformation under shear at a low viscosity ratio. *European Journal of Mechanics - B/Fluids*, 21(1), 49–59, 2002.

[64] V. Badalassi, H. Ceniceros and S. Banerjee. Computation of multiphase systems with phase field models. *Journal of Computational Physics*, 190(2), 371–397, 2003.

[65] L. Chang-Zhi and G. Lie-Jin. Numerical simulation of drop deformation and breakup in shear flow. *Heat TransferAsian Research*, 36(5), 286–294, 2007.

[66] P. Yue, J. J. Feng, C. Liu and J. Shen. A diffuse-interface method for simulating two-phase flows of complex fluids. *Journal of Fluid Mechanics*, 515, 293–317, 2004.

[67] M.-C. Lai, Y.-H. Tseng and H. Huang. An immersed boundary method for interfacial flows with insoluble surfactant. *Journal of Computational Physics*, 227(15), 7279–7293, 2008.

[68] H. Hua, Y. Li, J. Shin, H. kyu Song and J. Kim. Effect of confinement on droplet deformation in shear flow. *International Journal of Computational Fluid Dynamics*, 27(8–10), 317–331, 2013.

[69] H. Hua, J. Shin and J. Kim. Dynamics of a compound droplet in shear flow. *International Journal of Heat and Fluid Flow*, 50, 63–71, 2014.

[70] N. Aggarwal and K. Sarkar. Deformation and breakup of a viscoelastic drop in a Newtonian matrix under steady shear. *Journal of Fluid Mechanics*, 584, 1–21, 2007.

[71] S. Mukherjee and K. Sarkar. Effects of viscosity ratio on deformation of a viscoelastic drop in a Newtonian matrix under steady shear. *Journal of Non-Newtonian Fluid Mechanics*, 160(2), 104–112, 2009.

[72] R. Croce, M. Griebel and M. A. Schweitzer. Numerical simulation of bubble and droplet deformation by a level set approach with surface tension in three

dimensions. *International Journal for Numerical Methods in Fluids*, 62(9), 963–993, 2010.

[73] A. K. Gunstensen, D. H. Rothman, S. Zaleski and G. Zanetti. Lattice Boltzmann model of immiscible fluids. *Physical Review A*, 43, 4320–4327, 1991.

[74] X. Shan and H. Chen. Lattice Boltzmann model for simulating flows with multiple phases and components. *Physical Review E*, 47, 1815–1819, 1993.

[75] M. R. Swift, E. Orlandini, W. R. Osborn and J. M. Yeomans. Lattice Boltzmann simulations of liquid-gas and binary fluid systems. *Physical Review E*, 54, 5041–5052, 1996.

[76] X. He, S. Chen and R. Zhang. A lattice Boltzmann scheme for incompressible multiphase flow and its application in simulation of Rayleigh-Taylor instability. *Journal of Computational Physics*, 152(2), 642–663, 1999.

[77] H. Xi and C. Duncan. Lattice Boltzmann simulations of three-dimensional single droplet deformation and breakup under simple shear flow. *Physical Review E*, 59, 3022–3026, 1999.

[78] A. Gupta and M. Sbragaglia. Effects of viscoelasticity on droplet dynamics and break-up in microfluidic T-junctions: a lattice Boltzmann study. *European Physical Journal E*, 39(6), 2016.

[79] A. Wagner, L. Wilson and M. Cates. Role of inertia in two-dimensional deformation and breakdown of a droplet. *Physical Review E*, 68(4), 045301, 2003.

[80] R. van der Sman and S. van der Graaf. Emulsion droplet deformation and breakup with lattice Boltzmann model. *Computer Physics Communications*, 178(7), 492–504, 2008.

[81] S. Farokhirad, T. Lee and J. F. Morris. Effects of inertia and viscosity on single droplet deformation in confined shear flow. *Communications in Computational Physics*, 13(3), 706–724,2013.

[82] A. Komrakova, O. Shardt, D. Eskin and J. Derksen. Lattice Boltzmann simulations of drop deformation and breakup in shear flow. *International Journal of Multiphase Flow*, 59, 24–43, 2014.

[83] A. Komrakova, O. Shardt, D. Eskin and J. Derksen. Effects of dispersed phase viscosity on drop deformation and breakup in inertial shear flow. *Chemical Engineering Science*, 126(0), 150–159, 2015.

[84] Y. Shi and G. Tang. Simulation of Newtonian and non-Newtonian rheology behavior of viscous fingering in channels by the lattice Boltzmann method. *Computers & Mathematics with Applications*, 68(10), 1279 – 1291, 2014.

[85] Y. Shi and G. Tang. Lattice Boltzmann simulation of droplet formation in non-Newtonian fluids. *Communications in Computational Physics*, 17(04), 1056–1072, 2015.

[86] H. Liu and Y. Zhang. Phase-field modeling droplet dynamics with soluble surfactants. *Journal of Computational Physics*, 229(24), 9166–9187, 2010.

[87] O. Shardt, J. Derksen and S. K. Mitra. Simulations of droplet coalescence in simple shear flow. *Langmuir, 2013*, 29 (21), 6201–6212, 2010.

[88] H. Liu and Y. Zhang. Droplet formation in a T-shaped microfluidic junction. *Journal of Applied Physics*, 106(3), 034906, 2009.

[89] H. Liu and A. J. Valocchi. Three-dimensional lattice Boltzmann model for immiscibe two-phase flow simulations. *Physical Review E*, 85, 046309, 2012.

[90] H. Liu and Y. Zhang. Droplet formation in microfluidic cross-junctions. *Physics of Fluids*, 23(8), 082101, 2011.

[91] S. Kondaraju, H. Farhat and J. S. Lee. Study of aggregational characteristics of emulsions on their rheological properties using the lattice Boltzmann approach. *Soft Matter*, 8, 1374–1384, 2012.

[92] A. P. Hollis, T. J. Spencer, I. Halliday and C. M. Care. Dynamic wetting boundary condition for continuum hydrodynamics with multi-component lattice Boltzmann

equation simulation method. *IMA Journal of Applied Mathematics*, 76(5), 726–742, 2011.

[93] Y. Ba, H. Liu, J. Sun and R. Zheng. Color-gradient lattice Boltzmann model for simulating droplet motion with contact-angle hysteresis. *Physical Review E*, 88, 043306, 2013.

[94] H. Liu, Y. Ju, N. Wang, G. Xi and Y. Zhang. Lattice Boltzmann modeling of contact angle and its hysteresis in two-phase flow with large viscosity difference. *Physical Review E*, 92, 033306, 2015.

[95] Y. Ba, H. Liu, J. Sun and R. Zheng. Three dimensional simulations of droplet formation in symmetric and asymmetric T-junctions using the color-gradient lattice Boltzmann model. *International Journal of Heat and Mass Transfer*, 90, 931 – 947, 2015.

[96] H. Liu, Y. Zhang and A. J. Valocchi. Lattice Boltzmann simulation of immiscible fluid displacement in porous media: Homogeneous versus heterogeneous pore network. *Physics of Fluids*, 27(5), 052103, 2015.

[97] H. Liu, Y. Zhang and A. J. Valocchi. Modeling and simulation of thermocappilary flows using lattice Boltzmann method. *Journal of Computational Physics 4433-4453*, 2012.

[98] J. Li, H. Liu, N. Ioannou, Y. Zhang and J. M. Reese. Lattice Boltzmann simulations of thermocapillary motion of droplets in microfluidic channels. *Communications in Computational Physics*, 17, 1113–1126, 2015.

[99] H. J. Butt, K. Graf and M. Kappl. *Physics and Chemistry of Interfaces*. Wiley-VCH Verlag GmbH & Co. KGaA, 2003.

[100] S. Haeri and J. S. Shrimpton. On the application of immersed boundary, fictitious domain and body-conformal mesh methods to many particle multiphase flow. *International Journal of Multiphase Flow*, 40, 38–55, 2012.

[101] T. Hou, J. Lowengrub and M. Shelley. Boundary integral methods for multi-component fluids and multiphase materials. *Journal of Computational Physics*, 169(2), 302–362, 2001.

[102] M. Wörner. Numerical modeling of multiphase flows in microfluidics and micro process engineering: a review of methods and applications. *Microfluidics and Nanofluidics*, 12(6), 841–886, 2012.

[103] M. Lappa. Coalescence and non-coalescence phenomena in multi-material problems and dispersed multiphase flows: Part 2, a critical review of CFD approaches. *Fluid Dynamics and Material Processing*, 1(3), 213–234, 2005.

[104] C. K. Aidun and J. R. Clausen. Lattice-Boltzmann method for complex flows. *Annual Review of Fluid Mechanics*, 42, 439–472, 2010.

[105] J. Brackbill, D. Kothe and C. Zemach. A continuum method for modeling surface tension. *Journal of Computational Physics 100, 335–354*, 1992.

[106] D. Lörstad and L. Fuchs. High-order surface tension VOF-model for 3D bubble flows with high density ratio. *Journal of Computational Physics*, 200(1), 153–176, 2004.

[107] A. J. James and J. Lowengrub. A surfactant-conserving volume-of-fluid method for interfacial flows with insoluble surfactant. *Journal of Computational Physics*, 201(2), 685–722, 2004.

[108] A. J. James and J. Lowengrub. *Free Boundary Problems: Theory and Applications*, Chapter: Numerical Modeling of Surfactant Effects in Interfacial Fluid Dynamics, 251–261. Birkhäuser Basel, Basel, 2007.

[109] S. Afkhami, S. Zaleski and M. Bussmann. A mesh-dependent model for applying dynamic contact angles to VOF simulations. *Journal of Computational Physics*, 228(15), 5370–5389, 2009.

[110] S. Chen and G. D. Doolen. Lattice Boltzmann method for fluid flows. *Annual Review of Fluid Mechanics*, 30(1), 329–364, 1998.

[111] T. Reis and T. N. Phillips. Lattice Boltzmann model for simulating immiscible two-phase flows. *Journal of Physics A: Mathematical and Theoretical*, 40(14), 4033, 2007.

[112] J. Zhang. Lattice Boltzmann method for microfluidics: models and applications. *Microfluidics and Nanofluidics*, 10(1), 1–28, 2011.

[113] S. Succi. Lattice Boltzmann 2038. *Europhysics Letters*, 109(5), 50001, 2015.

[114] F. Massaioli and G. Amati. Achieving high performance in a LBM code using OpenMp. *The Fourth European Workshop on OpenMP, Roma.* 2002.

[115] Q. Li, K. Luo, Q. Kang, Y. He, Q. Chen and Q. Liu. Lattice Boltzmann methods for multiphase flow and phase-change heat transfer. *Progress in Energy and Combustion Science*, 52, 62–105, 2016.

[116] R. Nourgaliev, T. Dinh, T. Theofanous and D. Joseph. The lattice Boltzmann equation method: theoretical interpretation, numerics and implications. *International Journal of Multiphase Flow*, 29(1), 117–169, 2003.

[117] J. Yang and E. S. Boek. A comparison study of multi-component lattice Boltzmann models for flow in porous media applications. *Computers & Mathematics with Applications*, 65(6), 882–890, 2013.

[118] H. Liu, Q. Kang, C. R. Leonardi, S. Schmieschek, A. Narváez, B. D. Jones, J. R. Williams, A. J. Valocchi and J. Harting. Multiphase lattice Boltzmann simulations for porous media applications. *Computational Geosciences*, 1–29, 2015.

[119] M. Sbragaglia, R. Benzi, L. Biferale, S. Succi, K. Sugiyama and F. Toschi. Generalized lattice Boltzmann method with multirange pseudopotential. *Physical Review E*, 75, 026702, 2007.

[120] D. Lycett-Brown and K. H. Luo. Improved forcing scheme in pseudopotential lattice Boltzmann methods for multiphase flow at arbitrarily high density ratios. *Physical Review E*, 91, 023305, 2015.

[121] Q. Li and K. H. Luo. Achieving tunable surface tension in the pseudopotential lattice Boltzmann modeling of multiphase flows. *Physical Review E*, 88, 053307, 2013.

[122] W. Wang, Z. Liu, Y. Jin and Y. Cheng. LBM simulation of droplet formation in micro-channels. *Chemical Engineering Journal*, 173(3), 828–836, 2011.

[123] J. Chin. Lattice Boltzmann simulation of the flow of binary immiscible fluids with different viscosities using the Shan-Chen microscopic interaction model. *Philosophical Transactions of the Royal Society of London A: Mathematical, Physical and Engineering Sciences*, 360(1792), 547–558, 2002.

[124] M. L. Porter, E. T. Coon, Q. Kang, J. D. Moulton and J. W. Carey. Multicomponent interparticle-potential lattice Boltzmann model for fluids with large viscosity ratios. *Physical Review E*, 86, 036701, 2012.

[125] M. Sbragaglia, H. Chen, X. Shan and S. Succi. Continuum free-energy formulation for a class of lattice Boltzmann multiphase models. *Europhysics Letters*, 86(2), 24005, 2009.

[126] A. Kuzmin, A. Mohamad and S. Succi. Multi-relaxation time lattice Boltzmann model for multiphase flows. *International Journal of Modern Physics C*, 19(06), 875–902, 2008.

[127] T. Inamuro, T. Ogata, S. Tajima and N. Konishi. A lattice Boltzmann method for incompressible two-phase flows with large density differences. *Journal of Computational Physics*, 198(2), 628–644, 2004.

[128] M. Yoshino, Y. Toriumi and M. Arai. Lattice Boltzmann simulation of two-phase viscoelastic fluid flows. *Journal of Computational Science and Technology*, 2, 330–340, 2008.

[129] H. Zheng, C. Shu and Y. Chew. A lattice Boltzmann model for multiphase flows with large density ratio. *Journal of Computational Physics*, 218(1), 353–371, 2006.

[130] H. Huang, L. Wang and X. yun Lu. Evaluation of three lattice Boltzmann models for multiphase flows in porous media. *Computers & Mathematics with Applications*, 61(12), 3606 – 3617, 2011.

[131] H. Liu. *Modelling and simulation of droplet dynamics in microfluidic devices.* Ph.D. Thesis, University of Strathclyde, 2010.

[132] S. V. Lishchuk, C. M. Care and I. Halliday. Lattice Boltzmann algorithm for surface tension with greatly reduced microcurrents. *Physical Review E*, 67, 036701, 2003.

[133] I. Halliday, A. P. Hollis and C. M. Care. Lattice Boltzmann algorithm for continuum multicomponent flow. *Physical Review E*, 76, 026708, 2007.

[134] M. Latva-Kokko and D. H. Rothman. Diffusion properties of gradient–based lattice Boltzmann models of immiscible fluids. *Physical Review E*, 71, 056702, 2005.

[135] H. Farhat and J. S. Lee. Suppressing the coalescence in the multi-component lattice Boltzmann method. *Microfluidics and Nanofluidics*, 11(2), 137–143, 2011.

[136] Z. Guo, C. Zheng and B. Shi. Discrete lattice effects on the forcing term in the lattice Boltzmann method. *Physical Review E*, 65, 046308, 2001.

[137] A. Artoli, A. Hoekstra and P. Sloot. Optimizing lattice Boltzmann simulations for unsteady flows. *Computers & Fluids*, 35(2), 227–240, 2006.

[138] T. Krüger, F. Varnik and D. Raabe. Shear stress in lattice Boltzmann simulations. *Physical Review E*, 79(4), 046704, 2009.

[139] J. Boyd, J. Buick and S. Green. A second-order accurate lattice Boltzmann non-Newtonian flow model. *Journal of Physics A: Mathematical and General*, 39(46), 14241, 2006.

[140] G. Tang, X. Li, Y. He and W. Tao. Electroosmotic flow of non-Newtonian fluid in microchannels. *Journal of Non-Newtonian Fluid Mechanics*, 157(1–2), 133–137, 2009.

[141] S. S. Mendu and P. Das. Flow of power-law fluids in a cavity driven by the motion of two facing lids - a simulation by lattice Boltzmann method. *Journal of Non-Newtonian Fluid Mechanics*, 175-176(0), 10 – 24, 2012.

[142] S. Chen, X. He, V. Bertola and M. Wang. Electro-osmosis of non-Newtonian fluids in porous media using lattice Poisson-Boltzmann method. *Journal of Colloid and Interface Science*, 436(0), 186–193, 2014.

[143] Z. Chai, B. Shi, Z. Guo and F. Rong. Multiple-relaxation-time lattice Boltzmann model for generalized Newtonian fluid flows. *Journal of Non-Newtonian Fluid Mechanics*, 166(5-6), 332–342, 2011.

[144] K. Fallah, M. Khayat, M. H. Borghei, A. Ghaderi and E. Fattahi. Multiple-relaxation-time lattice Boltzmann simulation of non-Newtonian flows past a rotating circular cylinder. *Journal of Non-Newtonian Fluid Mechanics*, 177-178(0), 1–14, 2012.

[145] Q. Li, N. Hong, B. Shi and Z. Chai. Simulation of power-law fluid flows in two-dimensional square cavity using multi-relaxation-time lattice Boltzmann method. *Communications in Computational Physics*, 15, 265–284, 2014.

[146] T. N. Phillips and G. W. Roberts. Lattice Boltzmann models for non-Newtonian flows. *IMA Journal of Applied Mathematics*, 76(5), 790–816, 2011.

[147] C. Liu and J. Shen. A phase field model for the mixture of two incompressible fluids and its approximation by a fourier-spectral method. *Physica D*, 179, 211–228, 2003.

[148] Y. Q. Zu and S. He. Phase-field-based lattice Boltzmann model for incompressible binary fluid systems with density and viscosity contrasts. *Physical Review E*, 87, 043301, 2013.

[149] M. E. Cates, J.-C. Desplat, P. Stansell, A. J. Wagner, K. Stratford, R. Adhikari and I. Pagonabarraga. Physical and computational scaling issues in lattice Boltzmann simulations of binary fluid mixtures. *Philosophical Transactions of the Royal Society of London Series A*, 363, 1917–1935, 2005.

[150] T. Zhang, B. Shi, Z. Guo, Z. Chai and J. Lu. General bounce-back scheme for concentration boundary condition in the lattice-Boltzmann method. *Physical Review E*, 85, 016701, 2012.

[151] V. Bertola and M. Marengo. *Single Drop Impacts of Complex Fluids: a Review.* Chapter 11, 267–298. Koninklijke Brill NV, Leiden, 2012.

[152] V. T. Tsakalos, P. Navard and E. Peuvrel-Disdier. Deformation and breakup mechanisms of single drops during shear. *Journal of Rheology*, 42(6), 1403–1417, 1998.

[153] A. Vananroye, R. Cardinaels, P. Van Puyvelde and P. Moldenaers. Effect of confinement and viscosity ratio on the dynamics of single droplets during transient shear flow. *Journal of Rheology*, 52(6), 1459–1475, 2008.

[154] D. Megias-Alguacil. Surface rotation of liquid droplets under a simple shear flow: Experimental observations in 3D. *Soft Materials*, 11(1), 1–5, 2013.

[155] M. R. Davidson and J. J. Cooper-White. Pendant drop formation of shear-thinning and yield stress fluids. *Applied Mathematical Modelling*, 30(11), 1392–1405, 2006.

[156] V.-L. Wong, K. Loizou, P.-L. Lau, R. S. Graham and B. N. Hewakandamby. Numerical simulation of the effect of rheological parameters on shear-thinning droplet formation, *4th Joint US-European Fluids Engineering Division Summer Meeting collocated with the ASME 2014 12th International Conference on Nanochannels, Microchannels, and Minichannels*, 2, 2014.

[157] S. J. Kim and W. R. Hwang. Transient stresses of two-dimensional model droplet emulsions subjected to simple shear flow by numerical simulations. *Korea-Australia Rheology Journal*, 23(3), 163–171, 2011.

[158] S. Wannaborworn, M. R. Mackley and Y. Renardy. Experimental observation and matching numerical simulation for the deformation and breakup of immiscible drops in oscillatory shear. *Journal of Rheology*, 46(5), 1279–1293, 2002.

Appendices

A Flowfield on the surface of a droplet

Figure (A.1) illustrates the velocity on the surface of the droplet for the case $Re = 0.1$, $Ca = 0.2$, $\lambda = 5$, $2R/H = 0.18$, from different viewpoints. The contours show the velocity magnitude: red for high and blue for low values. Qualitatively similar images are shown in experiments in which the corresponding capillary number is approximately 0.156 and the viscosity ratio 17 (calculated from the data given) [154]. The confinement is not reported.

Figures (A.1(a)) and (A.1(c)) relate to figures (2–top view) and (3–side view) in [154], respectively. Notice that figure (A.1(a)) resembles figure (4) therein.

B Complementary comments on *Chapter* 3

Figures (B.1) and (B.2) illustrate the deformation and orientation angle as a function of the capillary number for viscosity ratios $\lambda = 0.3$, 1, and 3 at each confinement separately. The plots are a recreation of the ones shown in figure (3.4) in *Chapter* 3. This representation provides with clearer image on the different wall effects in individual viscosity ratio values.

Figure (B.3) illustrates on the left-hand side the deformation, and on the right-hand side the orientation angle as a function of Ca in confinement ratios $2R/H = 0.18$, 0.4, and 0.7 for each power-law exponent. These plots recreate the ones in figures (3.11) in *Chapter* 3. The results for the Newtonian matrix fluid ($n_c = 1$) are illustrated for comparison reasons. The reaction of the droplet in increasing confinement is independent of the exponent, except for the case $n_c = 1.25$ at $2R/H = 0.7$.
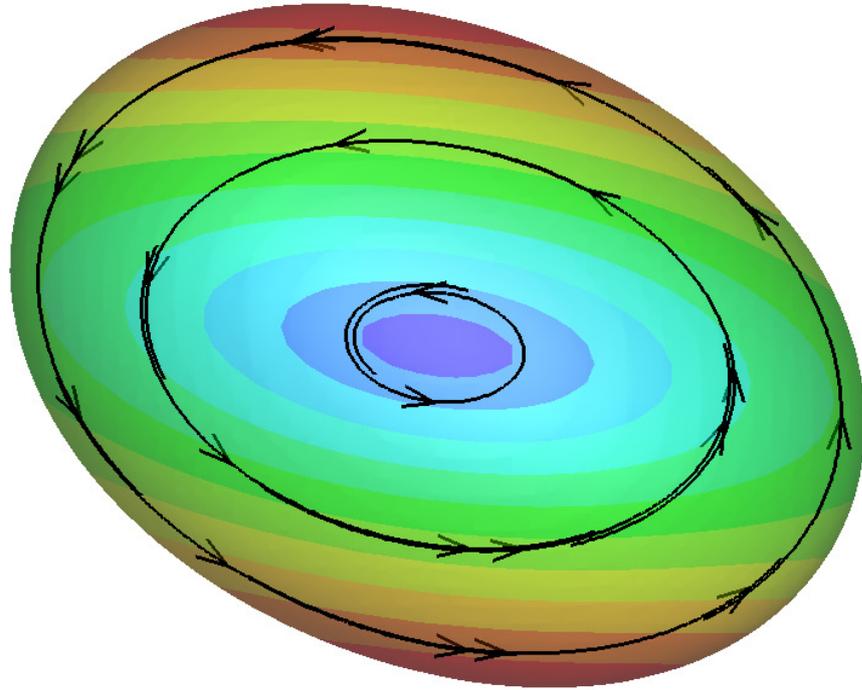
(a) xz plane
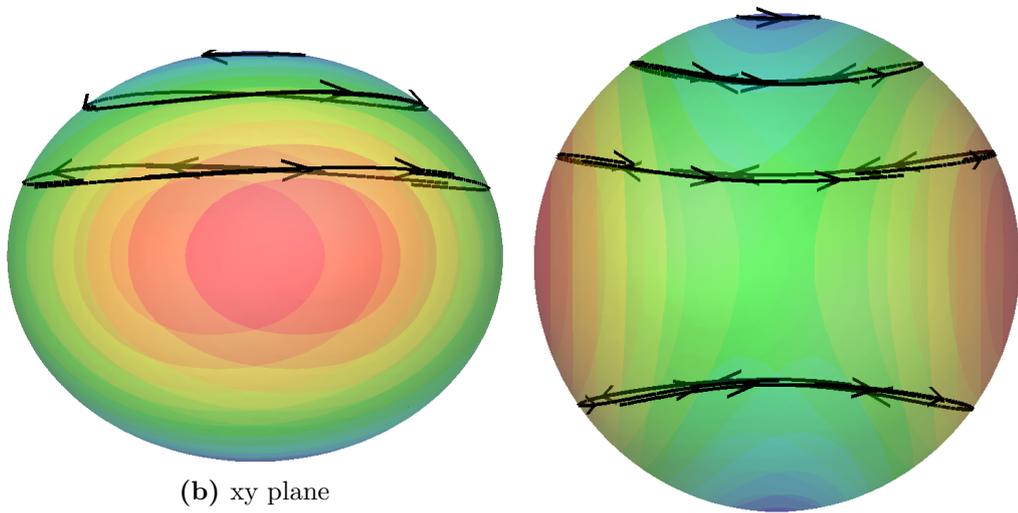
(b) xy plane

(c) yz plane

Figure A.1: Velocity on the surface of a Newtonian droplet from different viewpoints. 3D simulations for $Re = 0.1$, $Ca = 0.2$, $\lambda = 5$, $2R/H = 0.18$.

133

(a) $2R/H = 0.18$

(b) $2R/H = 0.4$

(c) $2R/H = 0.5$

(d) $2R/H = 0.7$
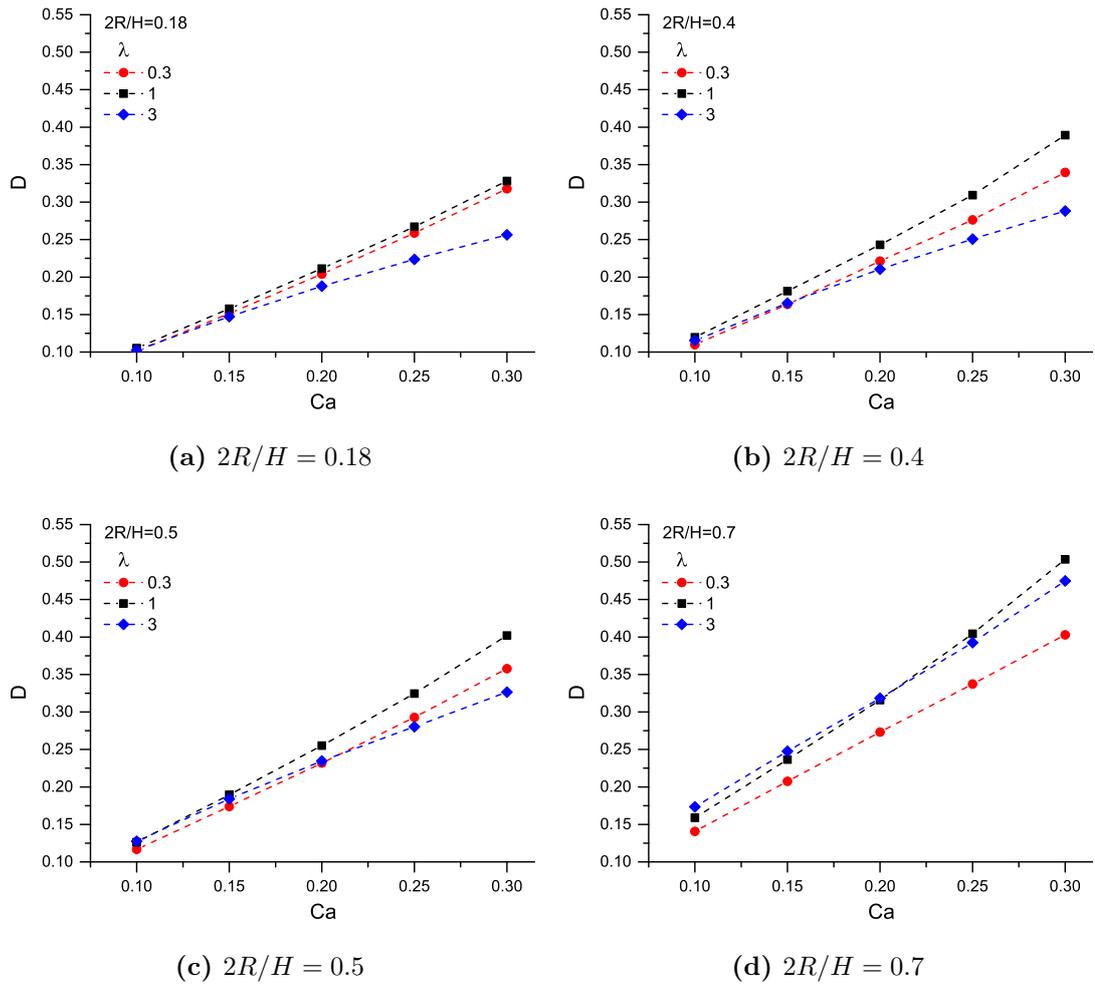
Figure B.1: Deformation parameter as a function of the capillary number Ca, for different viscosity ratios λ, in a specific confinement $2R/H$.

(a) $2R/H = 0.18$

(b) $2R/H = 0.4$

(c) $2R/H = 0.5$

(d) $2R/H = 0.7$
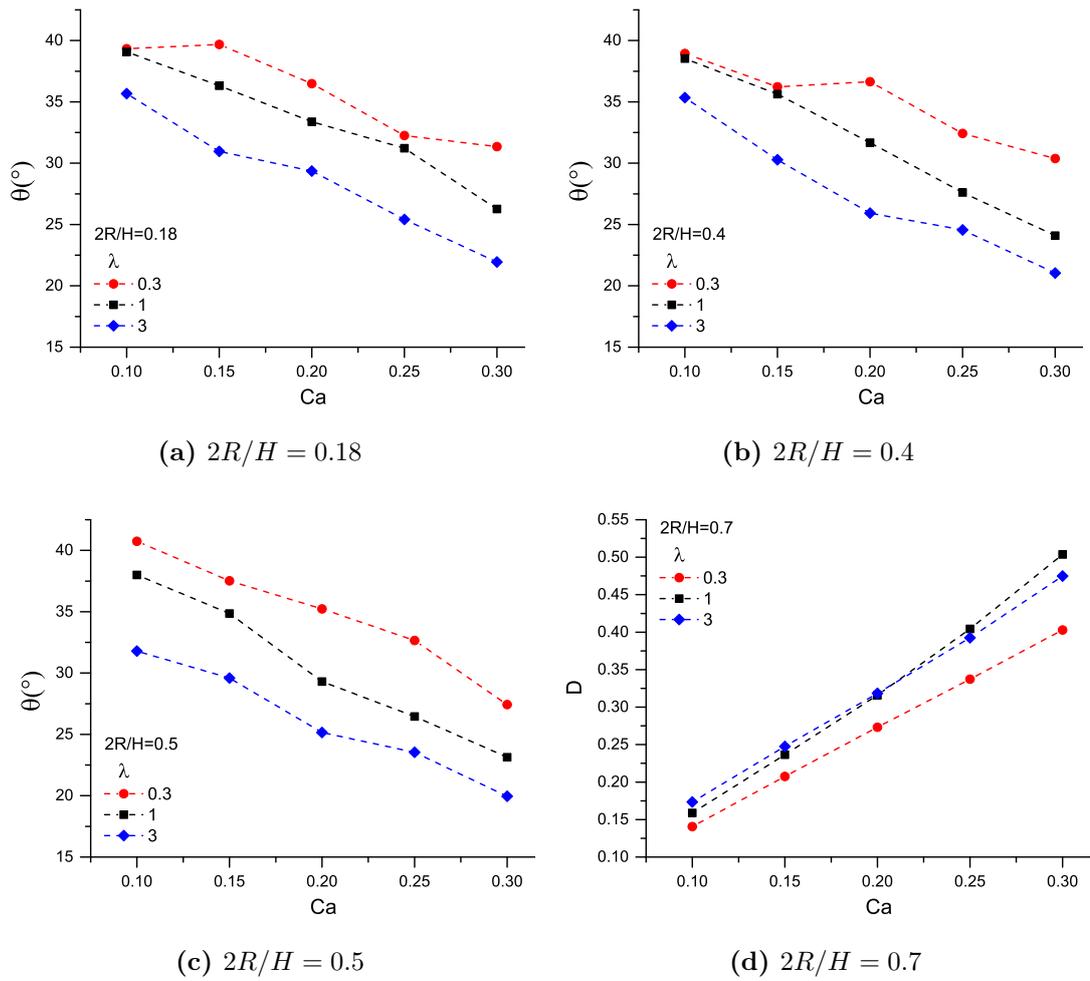
Figure B.2: Orientation angles as a function of the capillary number Ca, for different viscosity ratios λ, in a specific confinement $2R/H$.
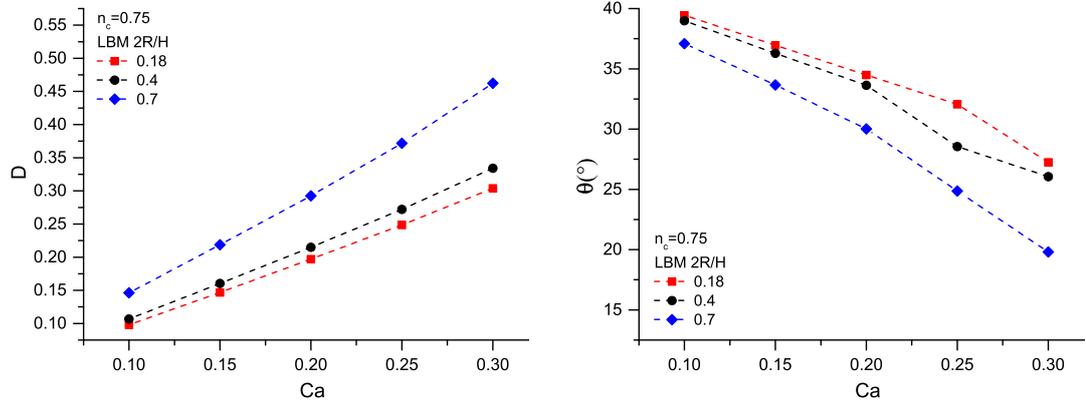
(a) $n_c = 0.75$
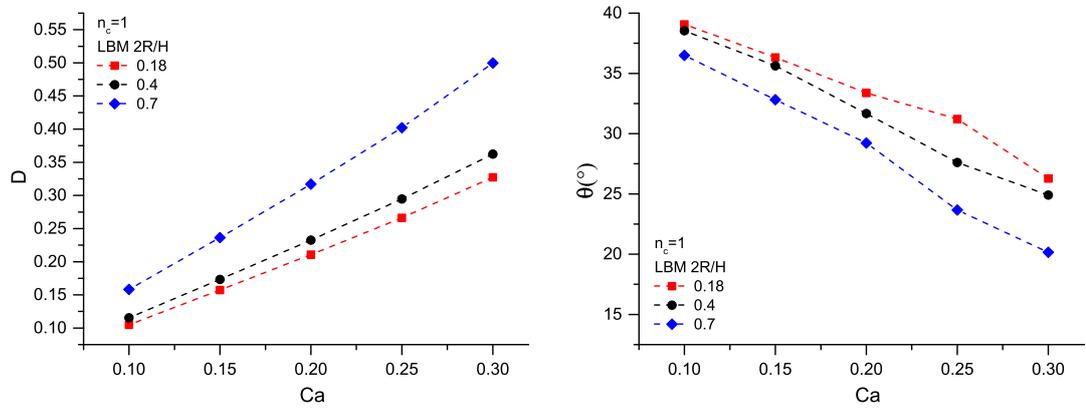
(b) $n_c = 1$
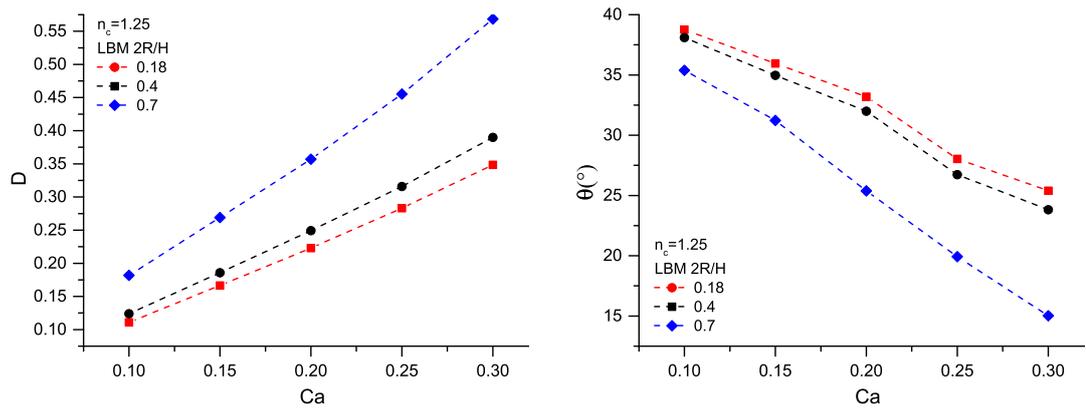
(c) $n_c = 1.25$

Figure B.3: (Left) Deformation parameter, and (right) orientation angle as a function of the capillary number, Ca, in various confinements for three power law exponents $n_c = 0.75$, 1, 1.25.

In figure (B.4) the shapes and stress vectors for droplets in two different confinement ratios are contrasted. Note that when comparing droplets in the same confinement ration in the same figure, the images were not clear. Table (B.1) presents the orientation angles (θ), and the maximum stress magnitudes, which interestingly are not exerted in the direction of the orientation angle.

Table B.1: Orientation angles (θ) and maximum stresses magnitude $\|\vec{T}\|$, in l.u. in the order of E-06.

	$2R/H = 0.4$		$2R/H = 0.7$	
	θ	$\|\vec{T}\|$	θ	$\|\vec{T}\|$
$\lambda = 0.3$	36.35°	15.1	31.3°	18.6
$\lambda = 1$	31.67°	19.8	28.88°	26.4
$\lambda = 3$	25.94°	18.5	24.68°	27.7
$n_c = 0.75$	33.64°	17.9	30°	22.6
$n_c = 1.25$	32°	21.8	25.38°	30.4

(a) $\lambda = 0.3$

(b) $\lambda = 1$

(c) $\lambda = 3$

(d) $n_c = 0.75$

(e) $n_c = 1.25$
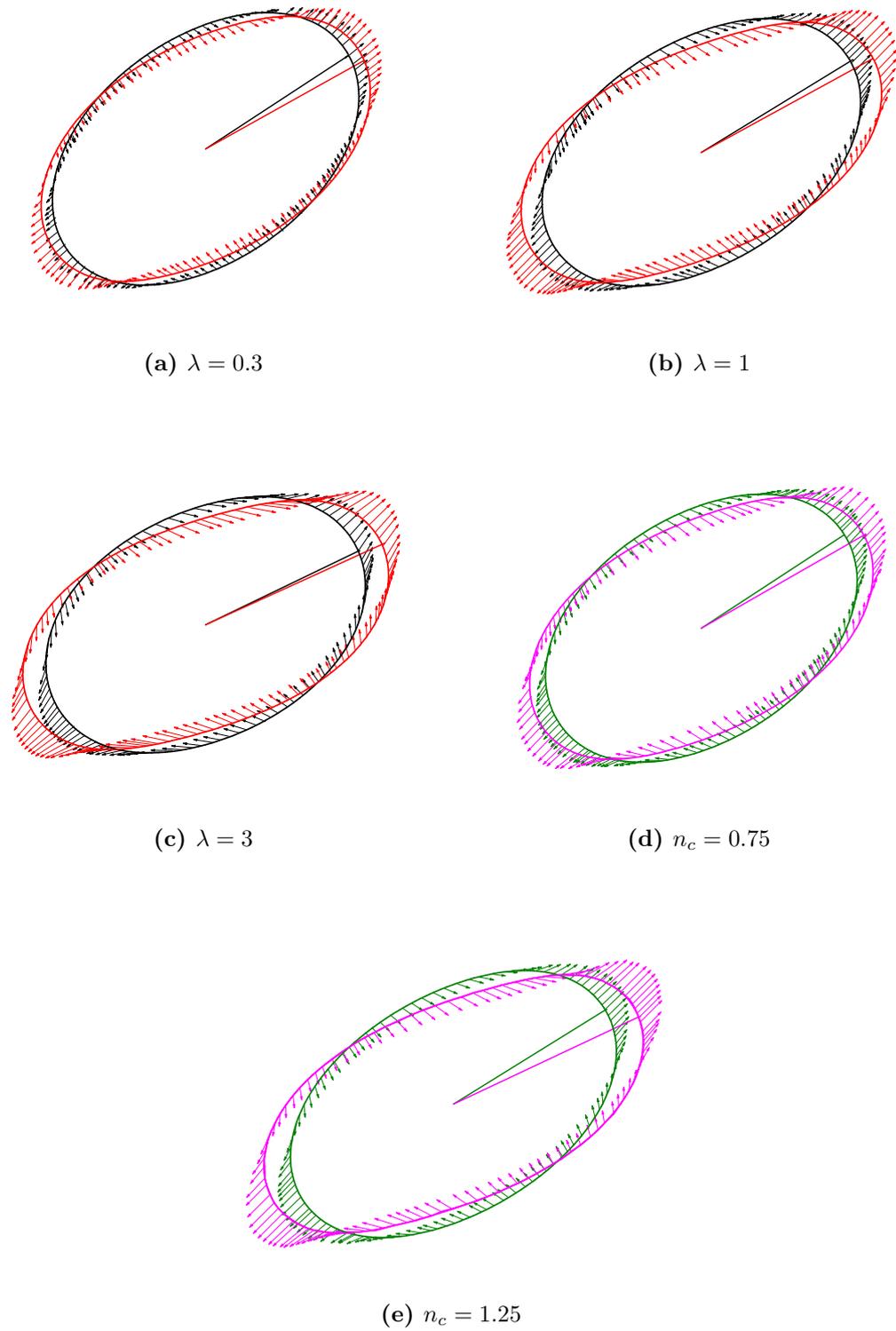
Figure B.4: Droplets shapes and stresses on the surface in confinement ratios (left) $2R/H = 0.4$, and (right) $2R/H = 0.7$, in the $x - z$ middle plane at $Ca = 0.2$, for various viscosity ratios λ and power-law exponents.

C   Complementary comments on *Chapter* 4

Deformation and orientation angle against confinement for Newtonian and power-law droplets

Figure (C.1) recreates the plots in figure (4.5), including the results for the Newtonian droplet in every viscosity ratio investigated shown in figure (3.5), *Chapter* 3.

Deformation and orientation differences of power-law droplets with increasing confinement

Table (C.1) presents the percentage change of the deformation (D) and the orientation angles (θ) values for different power-law droplets, from $2R/H = 0.3$ to 0.7, as shown in figure (4.5). In figure (4.5) the difference in tumbling cannot be clearly depicted for all the exponents studied together, due to the scaling of the vertical axis (θ). In parenthesis the differences in the orientation angle are shown in degrees.

Table C.1: Percentage increase of deformation and decrease of the orientation angle seen in figure (4.5) in Chapter 4.

n_d	0.75	0.875	1.0	1.125	1.25
$D \nearrow$	107.23 %	75.02 %	54.54 %	32.49 %	17.9 %
$\theta \searrow$	8.14 %	12.68 %	15.63 %	14.07 %	11.33 %
	(1.29°)	(3.35°)	(5.21°)	(5.16°)	(4.31°)

Newtonian and power-law droplet shapes and viscosities at $t^* = 5$ and 15

The shapes of the droplets and the viscosity contours for the systems: *i.* $N\text{-}N/\lambda = 0.3$, *ii.* $PL\text{-}N/n_d = 1.125$, and *iii.* $PL\text{-}N/n_d \approx 1.127$, are illustrated at the middle $x - z$ plane in figures (C.2) and (C.3) for time instants $t^* = 5$ and 15, respectively. Notice also the location of the tip at each droplet. Figure (C.4) plots the viscosity profiles along the neck of each droplet.

Neck-thinning for the PL-$N/n_d = 1.127$ system

Figure (C.5) illustrates the evolution of the interface for a droplet in the system PL-$N/n_d = 1.127$. The area in the centre is magnified and projected in the inset to reveal that the surface in the neck area continues to thin.

Comparison of stresses on droplets between high-viscous Newtonian and shear-thinning power-law drops

Table (C.2) presents the stresses for the *Newtonian-Newtonian*/$\lambda = 3$ and the *Power-law–Newtonian*/$n_d \approx 0.8837$ systems. Notice that in the region of the tip the normal stress T_{xx} which is related to the drop elongation is always larger in the *Newtonian-Newtonian*/$\lambda = 3$ system.

Table C.2: Stresses at the tip (x where $\partial u_z/z = 0$) and the neck ($x = 0$) of each droplet for (*i*) the Newtonian-Newtonian/$\lambda = 3$, and (*ii*) the Power-law–Newtonian/$n_d \approx 0.8837$ systems, at time instants $t^* = 5$, 15 and 20. Units in l.u. in the order of E-06.

t^*	Area case	Tip			Neck		
		T_{xx}	T_{xz}	T_{zz}	T_{xx}	T_{xz}	T_{zz}
5	*i*	17.18	46.24	0.06	-4.7	37.80	1.61
	ii	17.00	45.83	0.14	-5.9	38.4	1.98
15	*i*	16.5	46.45	-0.06	0.91	35.99	-0.28
	ii	16.31	45.56	-0.075	0.98	36.15	-0.35
20	*i*	15.59	45.55	-0.03	-0.82	36.23	0.38
	ii	15.51	45.49	-0.016	-0.374	36.28	0.19
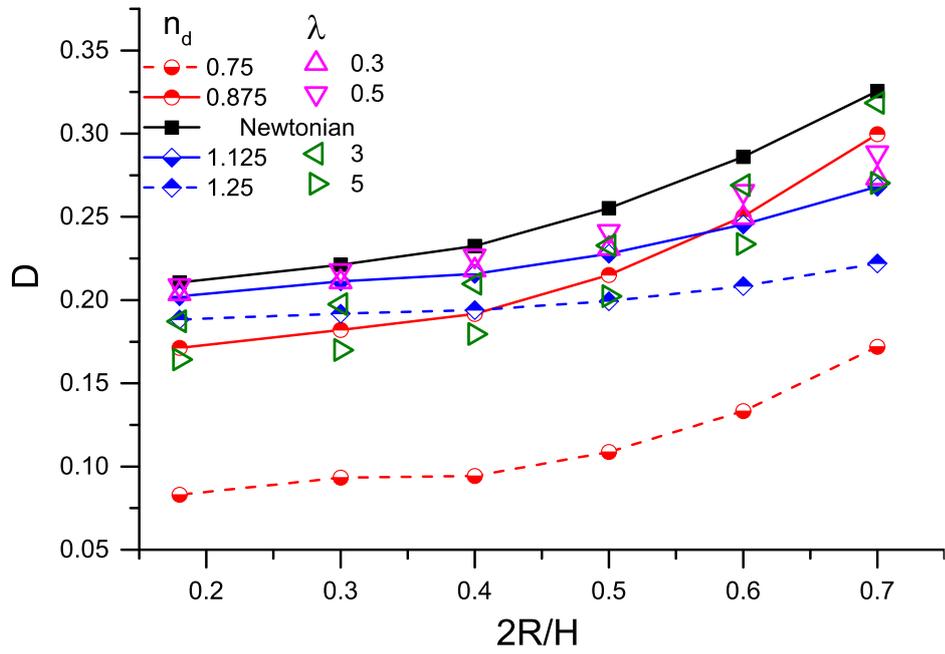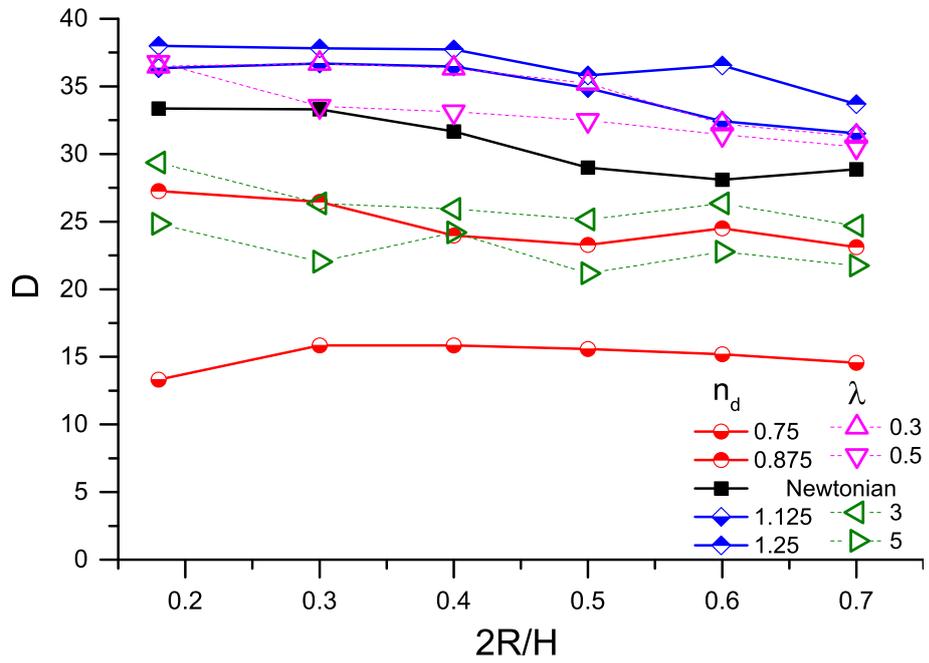
Figure C.1: (a) Droplet deformation, and (b) orientation angle as a function of the confinement ratios, 2R/H , for various exponents n_d, and viscosity ratios λ, for $Ca = 0.2$.
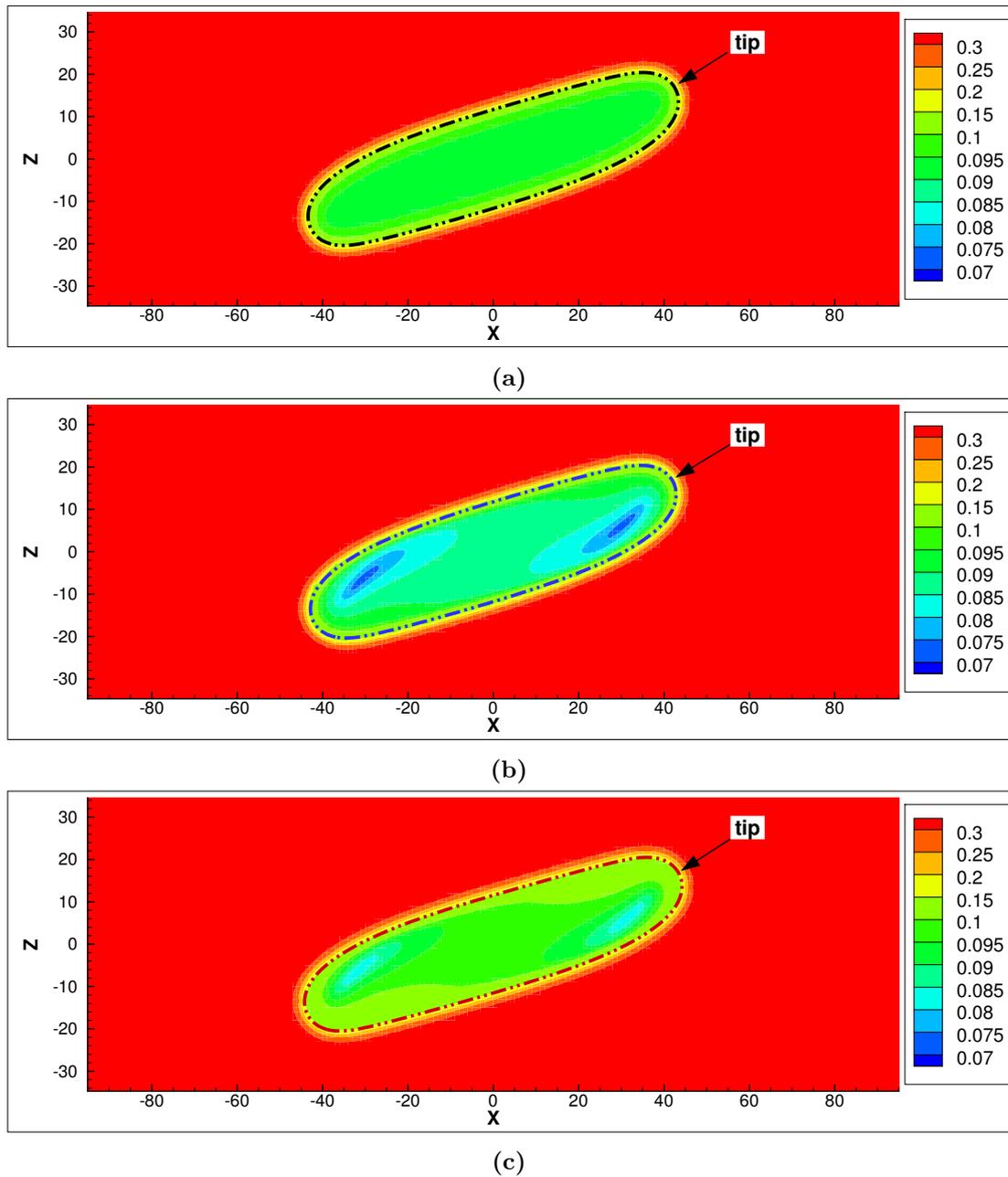
Figure C.2: Shapes of deformed droplets (dashed-dotted lines) and viscosity (see legend for contours in l.u.), in the $x - z$ middle plane, at time instant $t^* = 5$, for systems (a) $N\text{-}N/\lambda = 0.3$, (b) $PL\text{-}N/n_d = 1.125$, and (c) $PL\text{-}N/n_d \approx 1.127$, as described in *Chapter* 4.

(a)

(b)

(c)
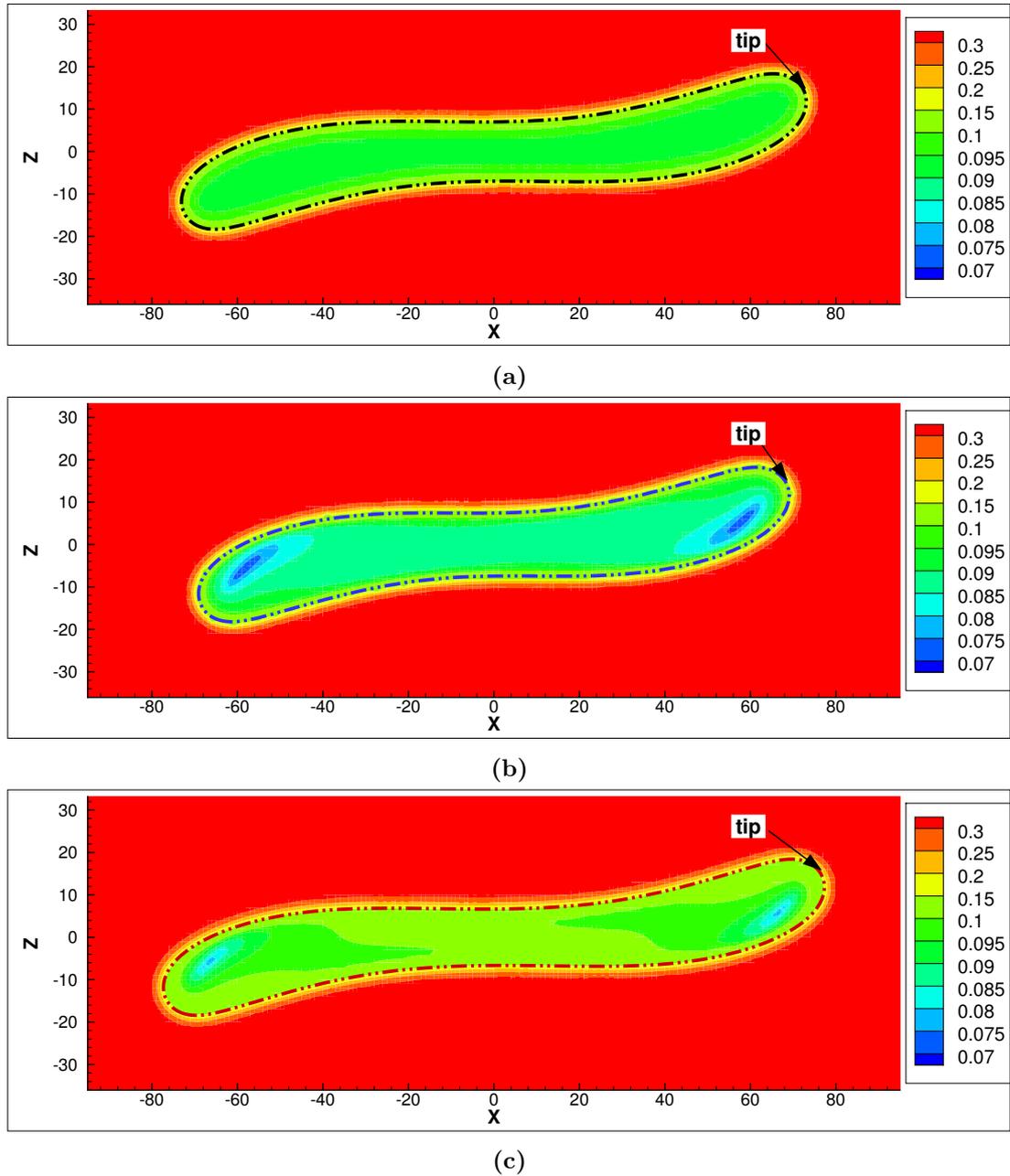
Figure C.3: Shapes of deformed droplets (dashed-dotted lines) and viscosity (see legend for contours in l.u.), in the $x - z$ middle plane, at time instant $t^* = 15$, for systems (a) N-$N/\lambda = 0.3$, (b) PL-$N/n_d = 1.125$, and (c) PL-$N/n_d \approx 1.127$, as described in *Chapter* 4..
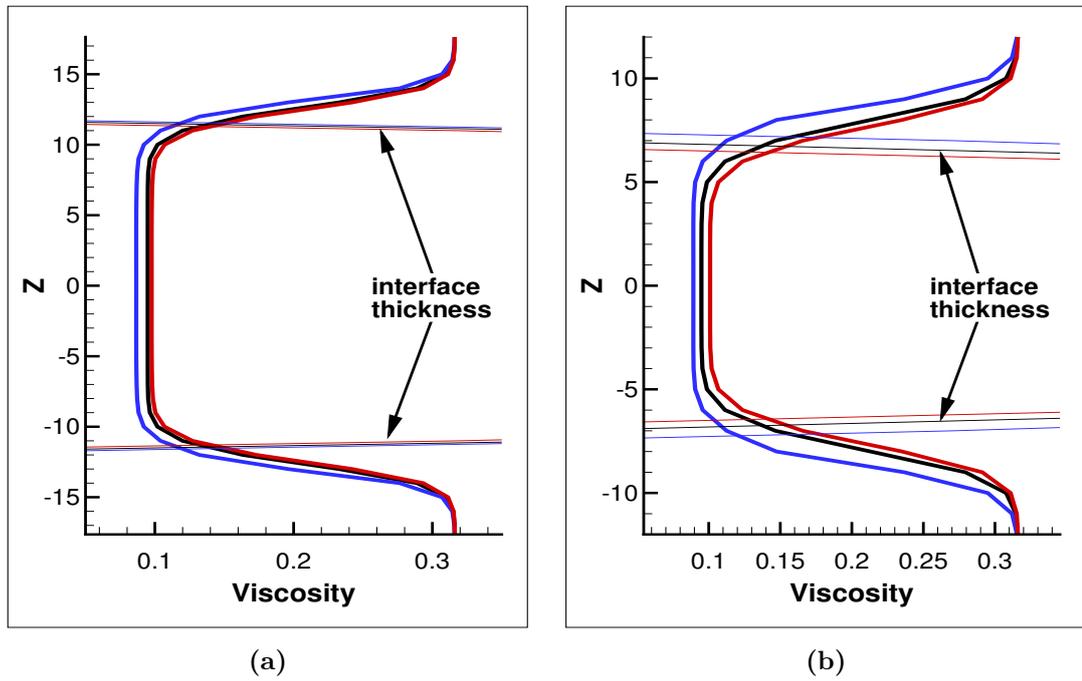
Figure C.4: Viscosity profile along height, z, at $x = 0$ at time instants (a) $t^* = 5$, and (b) $t^* = 15$, for systems systems (i) $N\text{-}N/\lambda = 0.3$ (black), (ii) $PL\text{-}N/n_d = 1.125$ (blue), and (iii) $PL\text{-}N/n_d \approx 1.127$ (red), as described in *Chapter* 4.
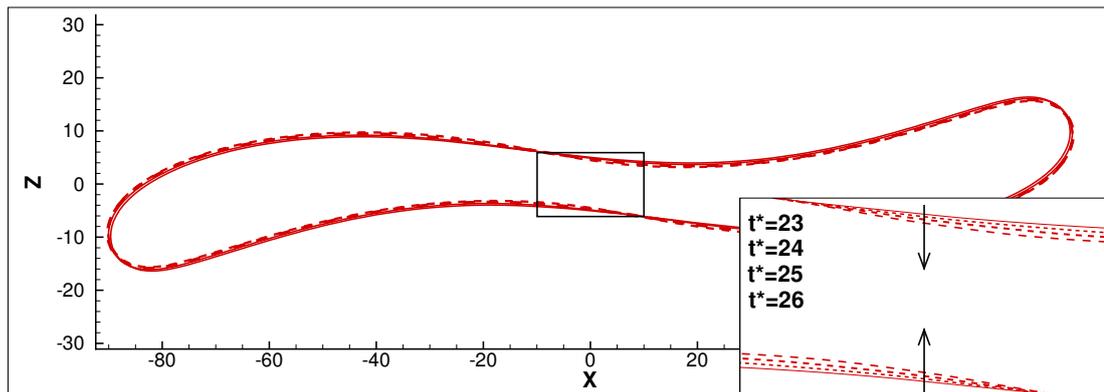
Figure C.5: Evolution of droplet shape for case *iii*. Notice the negligible droplet shape differences from $t^* = 23$ to 26. The inset indicates the slow neck narrowing trend (direction of the arrows) which eventually will lead to the breakup at time $t^* = 29$.

D   Fortran algotrithm for deformation and orienation angle calculations

In this Appendix, the program with which the deformation and orientation angles is presented with all the relative comments. Note, that a file produced by Tecplot with the coordinates of the points residing on the surface of the droplet in the middle plane is needed. This file should be formatted in two columns with the $x-$ and $z-$ values.

! This program reads a file where I have the coordinates of rho_N=0. The number of the lines of the input file varies
! Then it produces the deformation and the orientation angle
! The square root of: R^2 = (x-xc)^2 + (z-zc)^2 is the distance
! The highest R is the long axis of the ellipse and the lowest R the short axis. Deformation is calculated from (D-B)/(D+B)
! The angle is found for every distance. The location of the largest distance will set to give the orientation angle.
! Sometimes maybe you have to change the centre of the domain

module times
!- TIME VARIABLES
character(8) :: date
character(10) :: time1
character(5) :: zone
integer,dimension(8) :: values
real :: t1,t2
!————————————————————————
end module times

program Read_Coordinates_Write_D_Angle
use times
implicit none

integer i, lines, edge

double precision :: PI

double precision :: D, B, Def, xc, zc, Angle

double precision, allocatable, dimension(:) :: x, z, R, theta

! change the number at the right bound accordingly

character(len=70) :: cline

character(len=100):: filename, filename2

PI = 4.0d0*atan(1.0d0) ! Pi definition

xc = 50.0d0 ; zc=51.0d0 ! centre of the domain

filename = 'results.dat'! put the initial file (after you format it accordingly)

filename2= 'resultsb.dat'! output file

lines = 181 ! change the number accordingly to the number of points Tecplot has exported

allocate(x(1:lines))

allocate(z(1:lines))

allocate(R(1:lines))

allocate(theta(1:lines))

!——————————

call CPU_TIME(t1) ! call for timing starting point

!——————————

! Put the name of the file you want to change

open(1,file=filename), status="old",action="READ")!

! Reading the existing file

do i = 1, lines

read(1,*) x(i), z(i)

! Calculating R and theta

```
R(i) = (x(i)-xc)*(x(i)-xc) + (z(i)-zc)*(z(i)-zc)

R(i) = dsqrt(R(i))

theta(i) = (z(i)-zc)/(x(i)-xc)

theta(i) = atan(theta(i))

theta(i) = theta(i)*180.0d0/PI

enddo ! line

close(1)


! Calculate parameters

D = maxval(R)

B = minval(R)

Def = (D-B)/(D+B)

edge = maxloc(R,DIM=1) ! maxloc gives array as result – DIM=1 has to be here to
give a scalar and not a 1D array

Angle = theta(edge)


! Writing new file

open(2, file=filename2)

write(*,*) ''

write(2,*) 'For the case ', filename2

write(2,*) 'Deformation =', Def

write(2,*) 'Orientation angle =', Angle

write(2,*) maxloc(R), edge

write(2,*) ''

do i = 1, lines ! change the number at the right bound accordingly

write(2,*) x(i), z(i), R(i), theta(i)

enddo !

close(2)


! Print the deformation and orientation angle

write(*,*) ''
```

write(*,*) 'For the case ', filename2

write(*,*) 'Deformation =', Def

write(*,*) 'Orientation angle =', Angle

write(*,*) maxloc(R), edge

write(*,*) ''

!———————————

!- RUNNING TIME VARIABLE

call CPU_TIME(t2)

write (*,*) ''time'', t2 - t1,''sec'', (t2-t1)/60.0, ''mins''

call date_and_time(date,time1,zone,values)

call date_and_time(DATE=date,ZONE=zone)

call date_and_time(TIME=time1)

call date_and_time(VALUES=values)

write(*,*)''

write(*,*)''DATE AND TIME''

write(*,*) ''Date:'', Values(3), Values(2), Values(1)

write(*,*)''Time:'', Values(5), Values(6), Values(7)

!———————————

stop

end